TELLURIUM, ANTIMONY, AND SELENIUM ISOTOPES AS INDICATORS OF ELEMENTAL MOBILITY

BY

NAOMI LEAH WASSERMAN

DISSERTATION

Submitted in partial fulfillment of the requirements
for the degree of Doctor of Philosophy in Geology
in the Graduate College of the
University of Illinois at Urbana-Champaign, 2020

Urbana, Illinois

Doctoral Committee

Professor Thomas M. Johnson, Chair and Director of Research
Professor Craig C. Lundstrom
Assistant Professor Jennifer L. Druhan
Research Assistant Professor Robert Sanford

ABSTRACT

Redox reactions greatly influence metal and metalloid mobility, as different oxidation states can exhibit diverse geochemical behavior controlling solubility and adsorption affinity. Elucidating these processes is important in a wide range of geochemical applications, such as contaminant mobility, resource extraction, or the oxygenation of early Earth. Stable isotopic fractionation of redox-sensitive elements can be used as a means to identify redox reactions taking place. For example, selenium (Se) isotopes track reductive immobilization of the contaminant Se in groundwater or surface waters. Other isotope systems, like that of tellurium (Te) and antimony (Sb) have yet to be explored in depth and could provide information about biogeochemical processes that control their mobility in modern and ancient environments.

The work presented here seeks to improve our understanding of the isotope systematics of Te, Sb, and Se. I examined the potential of Te isotopes as a proxy of atmospheric oxygenation by creating a novel method to measure δ^{130}Te in a suite of paleosols and near-shore sediments ranging from 3.0 Ga to the Cenozoic. The results suggest that Te isotopes may track the initiation of global Te redox cycling triggered by O_2 levels at the Great Oxidation Event. For the oxyanions of the toxic metalloids, Sb and Te, one of the largest immobilizing processes is adsorption. Given the importance of this pathway, potential isotope effects induced by adsorption should be studied, as significant contribution from this fractionating process can complicate interpretations of redox-driven isotopic fractionation. I set up several experiments to examine the isotopic fractionation during adsorption of Sb and Te to goethite and illite at pH 6 and 8. The results indicate that isotope effects produced by adsorption are necessary to consider when using the Sb or Te isotope systems to track reduction reactions. Similarly, the isotope fractionation during Se(VI) or Se(IV) reduction may be complicated by other fractionating processes. For example, the oxidative dissolution of reduced Se-bearing phases has been assumed to produce minor isotopic fractionation but has not been studied in depth. I conducted oxidation experiments with selenide-bearing minerals, which revealed the presence of a persistent positive isotopic offset between the oxidized Se(VI) fraction and the mineral. This result has major implications in interpretation ofifer Se isotopic fractionation during reduction, especially in environments with fluctuating redox conditions. Taken together, the results of these studies advance the use of Te, Sb, and Se isotope systems as proxies of elemental mobility.

ACKNOWLEDGEMENTS

I am deeply indebted to my adviser, Tom, for guiding me to become a better scientist. Despite being the head of the department, Tom always made himself available to answer my questions and discuss my research with me. When I expressed self-doubt, he provided steadfast support. Tom challenged me to question my own interpretations of my research and inspired me to forge my own path as a scientist. I would also like to thank the members of my thesis committee, Craig Lundstrom, Robert Sanford, and Jennifer Druhan. Much of the knowledge I've gained during my PhD has come from their courses. They have been so generous in giving advice about my dissertation and professional development, in addition to lending resources to improve my research.

I am also thankful to Kathrin Schilling (LDEO) and Céline Pallud (UC Berkeley) for their work on the Se oxidation grant and their guidance on the work described in Chapter 4. In addition, I am grateful to Tom Kulp (SUNY-Binghamton) for his collaboration on explorations of Sb isotopic fractionation, and Joel Mackinney for establishing the Sb isotope measurement technique and anion exchange procedures. Many thanks to Sarah Hayes (USGS) for providing me with samples of mine tailings and David Smith (USGS), who gave me soils as part of the USGS Geochemical and Mineralogical Data for Soils of the Conterminous United States Project. Finally, I am deeply indebted to Noah Planavsky (Yale University), who provided me with the many valuable paleosol and ironstone formation samples measured in Chapter 5.

I also owe my success to the friends that I've made in the Department of Geology. Thank you, Mahta Ansari, Jia Wang, Gideon Bartov, Robert Hill, Hannah Toru, Noah Jemison, Joel Mackinney, and Matt Bizjack, for your friendship and conversations about life and geochemistry in Burrill and NHB. I would also like to thank Allie Wyman for being a great friend and BJJ partner. I am grateful to my 4042 officemates and the rest of the graduate students, who would drop whatever they were doing to commiserate with me about school and life. Jackie Wittmer-Malinowski sacrificed many hours to help me with our Dino Dig exhibit, and was a great mentor as I started graduate school. In addition, none of this work could have been completed without Lana Holben, Val Zigler, Rachel Davidson, Chandre Johnson, Scott Morris, and the rest of the SESE administrative staff. I am so grateful for their support and friendship.

I would like to thank my family for the innumerable ways they have supported me. Dave, Diane, Brian, Bobbi Jo, Ben, Isla, Cora and the extended Mand/Patt families have welcomed me with open arms ever since my first visit to Wisconsin. I am truly lucky to have such loving people in my life. In addition, I owe my success to my wonderful parents, my sister, grandparents, aunts, uncles, and cousins. My sister, Hana, has been my role model in terms of overcoming obstacles and finding self-confidence. My parents have instilled in me my appreciation for nature and science, a strong work ethic, and a desire to help others. I am incredibly privileged to have parents like them and my accomplishments are really a reflection of their values. Finally, I would like to thank my husband, Thom, for providing unwavering support and joy through the many peaks and valleys of my PhD. His drive and success during his own PhD and postdoc continues to be a source of inspiration to me. I am eternally grateful to Thom for being a wonderful partner.

TABLE OF CONTENTS

CHAPTER 1: INTRODUCTION

1.1 Significance

Redox reactions govern the mobility and concentration of contaminants (e.g. Cr, U, As), economically valuable metal(loids) (e.g. Cu, Te, Sb), and elements considered essential for animal and human life (e.g. N, P, S, Se), as oxidation states of these redox-sensitive elements generally display distinct geochemical behavior. For example, reduced Cr(III) is highly insoluble and less bioavailable than the carcinogenic Cr(VI) species (Losi et al., 1994). Therefore, the identification and quantification of the reactions that reduce or oxidize Cr, in this instance, are essential to minimizing the fate and transport of this contaminant. This is often not possible in a groundwater aquifer, as multiple reactions or physical processes in addition to reduction may be responsible for decreasing Cr(VI) concentrations. Stable isotopic fractionation of multivalent elements can track the presence and magnitude of specific redox reactions (e.g. Jemison et al. (2018); Schilling et al. (2015); Berna et al. (2010))

The applications of stable isotopic fractionation to biogeochemistry focused mainly on "traditional" H, C, N, O, and S isotopic fractionation until the 1990s. Decades of work measuring traditional isotope systems by gas source mass spectrometry produced a strong foundational knowledge of stable isotope geochemistry (see Valley (2001) and references therein). Isotopic fractionation of isotope systems other than H, C, N, O, and S, meanwhile, was largely theoretical until multi-collector inductively coupled plasma mass spectrometry (MC-ICP-MS) (Anbar and Rouxel, 2007). Measurements of these isotope systems were largely limited by the ability to ionize elements of interest and to correct for instrumental mass fractionation. The advent of MC-ICP-MS addressed both of these issues. The introduction of sample into Ar plasma allowed elements with high ionization potentials to be ionized more efficiently (Colodner et al., 1994). In addition, instrumental mass fractionation, while large, is mostly constant over time and can be corrected for (Teng, 2017). In addition, a magnetic sector mass analyzer allows for multiple beams to be detected by different collectors simultaneously.

Since this advancement, geochemists have used a wide range of new isotope systems to study diverse topics in earth science, such as early earth formation and solar system formation (Teng et al., 2019), the evolution of life (Lyons et al., 2014; Robbins et al., 2016), climate change and paleoceanography (Anbar and Rouxel, 2007), mantle-crust evolution (e.g. Huang et al. (2010)), the formation of new mineral phases (e.g. Fernandez et al. (2019)), and contaminant studies (Bopp et al., 2010; Wiederhold, 2015). As a result, the majority of elements with multiple stable isotopes in the Periodic Table have been measured. However, many have not been explored in depth. The following work examines the isotopic fractionation of three such isotope systems: tellurium (Te), antimony (Sb), and selenium (Se) for applications of understanding elemental mobility in modern and ancient environments.

1.2 Notation

For any element, isotopic fractionation is measured as variation in the ratio (R) of the heavy to light isotope. This is expressed using delta (δ) notation where R_{sample} is normalized to R of a universal standard.

$$\delta = [R_{sample}/R_{standard} - 1] * 1000‰ \qquad (1.1)$$

The magnitude and direction of fractionation for any reaction is expressed as a fractionation factor α, which is defined as the ratio of $R_{(Instantaneous\ Product)}$ relative to the $R_{(Reactant)}$. This can also be written as ε, or $\varepsilon = (\alpha-1) * 1000‰$.

1.3 Background

1.3.1 Tellurium

Tellurium is a rare metalloid (crustal abundance: ~1 μg kg-^{1}) of increasing economic value (Hu and Gao, 2008; Zweibel, 2010). Tellurium is both acutely toxic and teratogenic, but little is known about chronic exposure to low levels of Te (Perez-D'Gregorio et al., 1988b; Yarema and Curry, 2005). Higher demand for Te is coupled to its use in CdTe solar panels, and to a lesser extent, batteries, thermoelectric devices, and nanotechnology (Zweibel, 2010). Due to the growth in the solar industry, the U.S. Department of Energy deemed it an economically critical metal in 2016 (Goldfarb, 2015b). However, increased Te extraction has resulted in more instances of mining and refining-related contamination (Hayes and Ramos, 2019; Perkins, 2011; Wiklund et al., 2018). Understanding the biogeochemical reactions governing Te mobility is important for both improving resource extraction and mitigating the contamination of this metalloid.

Relatively little is known about Te geochemistry. Tellurium exists in four oxidation states, -II, 0, IV, and VI. The two lower valences, Te(0) and Te(-II), tend to be the most insoluble. Reduced tellurides form mineral phases with Ag, Cu, and Pb in sulfide-rich magmatic and hydrothermal ore deposits (Missen et al., 2020; Watterson et al., 1977). In the oxidized states, Te(IV) and Te(VI) are soluble oxyanions. Both oxyanions, though, show high adsorption affinity to Mn- and Fe-(oxy)hydroxides (Hein et al., 2003b; Kashiwabara et al., 2014b) and, to a lesser extent, clay minerals (Qin et al., 2017). Due to heavy scavenging of Te by solid surfaces in groundwater, surface waters, and the ocean, dissolved Te concentrations are low (< 1 ng L^{-1}) (Filella et al., 2019; Lee and Edmond, 1985). As a result, Fe-rich soils and marine sediments, especially ferromanganese crusts, are enriched relative to the crustal abundance of Te

(Kashiwabara et al., 2014b; Schirmer et al., 2014). Unlike its fellow chalcogen, Se, Te has no known biological role and causes oxidative stress. Tellurium redox reactions, however, can be microbially-mediated. Dissimilatory reduction of Te by a variety of microorganisms of Te(VI) to Te(IV) and Te(IV) to Te(0) nanoparticles or volatile methylated species occurs through a detoxification mechanism (Baesman et al., 2007; Ollivier et al., 2011; Ramos-Ruiz et al., 2016). In addition, a few examples of anaerobic microbial respiration with Te(VI) and Te(IV) as terminal electron acceptors have been reported (Baesman et al., 2007; Csotonyi et al., 2006).

Tellurium has eight stable isotopes (^{120}Te, ^{122}Te, ^{123}Te, ^{124}Te, ^{125}Te, ^{126}Te, ^{128}Te, and ^{130}Te). Study of Te isotopic fractionation is still in its infancy. The first examination of Te isotopic fractionation by Smithers and Krouse (1968) theoretically calculated equilibrium isotope partitioning equivalent to a 5‰ difference between the δ^{130}Te/^{126}Te of Te(VI) and Te(-II). In the same study, experimentally observed mass-dependent isotopic fractionation during reduction of Te(VI) by sulfite produced a $\varepsilon^{130/126}$Te of -3.2‰. Baesman et al. (2007) found a similar fractionation of -1.6 to 3.2‰ during the reduction of Te(VI) and Te(IV) to Te(0) by acetate-fed cultures, *Bacillus selenitireducens* and *Sulfurospirillum barnesii*. Until recently, no studies examining Te isotopic fractionation in natural samples existed. Recent work by Fornadel et al. (2017), Fukami et al. (2018) and Fehr et al. (2018), though, show significant mass-dependent isotope variations in ore deposits, meteorites, igneous rocks, and marine sediments. However, no examinations of Te isotopic fractionation in soils of modern or ancient environments have been conducted.

1.3.2 Antimony

Antimony is a much more common metalloid (upper crustal abundance ~300 μg kg^{-1}) than Te and is of greater environmental concern (Hu and Gao, 2008; Tanner and Ehmann, 1967).

Higher levels of Sb ingestion can result in acute toxicity (>9 mg L^{-1} Sb in water), and long-term exposure to Sb is correlated to higher prevalence of cancer and heart disease (Cooper and Harrison, 2009; Guo et al., 2016). Numerous consumer products contain non-trivial amounts of Sb, including polyethylene terephthalate (PET) plastic bottles (Westerhoff et al., 2008), brake pads (von Uexküll et al., 2005), and lead alloys (Okkenhaug et al., 2013). Leaching experiments of water bottles, and measurements of Sb concentrations next to highly trafficked roadways show significant elevation of this metalloid, indicating that Sb is released from these commonplace items.

Antimony exists in two oxidation states, Sb(III) and Sb(V), in low-temperature environments. Similar to Te, the reduced species is less soluble, forming a variety of Sb(III)-oxide minerals when sulfide is absent, and stibnite (Sb_2S_3) when sulfide is present (Filella and May, 2005; Filella et al., 2009; Olsen et al., 2018). However, at low concentrations, Sb(III) can form soluble $Sb(OH)_3$ and aqueous sulfide complexes, as observed in geothermal waters (Wilson et al., 2012). In addition to abiotic reduction by sulfide, microbial reduction and oxidation of Sb are ubiquitous geochemical reactions (Abin and Hollibaugh, 2014; Kulp et al., 2014). Both of these reactions are thought to involve biological pathways similar to As reduction or oxidation and have occurred in strains isolated in low Sb environments (Li et al., 2016).

As production of Sb is now dominantly driven by China, Sb mines in the US, Canada, and Australasia are presently inactive (Seal et al., 2017). The legacy contamination at Sb and gold mining operations, where Sb is a co-contaminant, has become the focus of many studies (Ashley et al., 2007; Cidu et al., 2014; Wang et al., 2011; Wilson et al., 2004). Investigations examining weathering of Sb-bearing mine tailings show that the immobilization of $Sb(OH)_6^-$ is controlled by adsorption to Fe-(oxy)hydroxides and clays (Wilson et al., 2012). In addition, remineralization of Sb(V) in Fe-(oxy)hydroxides (Burton et al., 2020) and formation of tripuyhite ($FeSbO_4$) has been suggested to be an important attenuating process of Sb(V) (Leverett et al., 2012). Sb(III) also has a high adsorption affinity to Fe-(oxy)hydroxides (Leuz et al., 2006). In oxic environments, $Sb(OH)_{3(aq)}$ oxidation is catalyzed by adsorption to ferric oxides (Leuz et al., 2006).

Antimony has two stable isotopes ^{121}Sb and ^{123}Sb, which exist in roughly equal proportions. The ratio of these two isotopes has been shown to vary in stibnite minerals (~1.5‰), mine-impacted river water (~1.0‰), and deep-sea sediments (~0.6‰) (Resongles et al., 2015; Rouxel et al., 2003). However, the interpretation of this data lacks a foundation, as only two studies thus far have conducted laboratory studies to examine the "isotope systematics" of Sb. Rouxel et al. (2003) found that reduction of Sb(V) by potassium iodide produced a -0.9‰ difference between the instantaneous product and reactant. Reduction of Sb(V) by sulfide in an acidic medium also produced a similar magnitude fractionation of -1.4‰ (Mackinney, 2016). In order to be able to use Sb isotopes to interpret biogeochemical cycling, laboratory experiments examining other environmentally relevant processes like biological reduction, oxidation, and adsorption should be conducted.

1.3.3 Selenium

Selenium (Se) is a micronutrient, but it is toxic at moderate levels to humans and animals. Insufficient intake of Se can cause Keshan disease, a weakening of the cardiovascular system (Loscalzo, 2014), while high levels of Se leads to multiple-organ failure caused by selenosis (Sutter et al., 2008). Se intake is related to the geological distribution of Se in waters and soils. In the United States, the weathering of seleniferous marine shales contributes to Se-enriched sediments (e.g. Presser and Swain (1990)). Therefore, the US Environmental Protection Agency has established a maximum contaminant level of 50 ng g^{-1} Se in drinking water (EPA, 2018). In the late 1980s, the ecological impact of high levels of selenium concentrated by irrigation canals became apparent at the Kesterson River National Wildlife Refuge (CA). Bioaccumulation of Se resulted in deformed embryos of waterfowl enriched with mg kg^{-1} levels of Se (Ohlendorf et al., 1990). Other examples of Se anthropogenic contamination include leaching of Se-rich overburden in waste rock piles and impoundments with coal combustion residuals (Brandt et al., 2019; Mebane et al., 2014). In these instances, redox processes primarily control the release and fate of this element.

In the more oxidized forms, Se(VI) and Se(IV) occur as soluble oxyanions, SeO_4^{2-}, SeO_3^{2-} and $HSeO_3^-$. Se(IV) adsorbs readily to Fe and Mn-(oxy)hydroxides and clays, making it more particle-reactive than Se(VI) (Balistrieri and Chao, 1990; Peak, 2006; Peak and Sparks, 2002). Meanwhile, the reduced oxidation states, Se(0) and Se(-II), exist in largely insoluble phases in low-temperature settings. This paradigm is complicated by biological assimilation of Se(IV) and transformation of Se to organo-selenides, which can make up a large percentage of Se present in more reducing settings (Clark and Johnson, 2010; Schilling et al., 2015). Se oxyanions can also serve as terminal electron acceptors and undergo dissimilatory reduction to Se(0) or methylated compounds. This often occurs through pathways that also reduce nitrate, nitrite, and sulfate (Hockin and Gadd, 2006; Sabaty et al., 2001). Microbial oxidation of Se(0) is soils is also active, but occurs at much slower rates than reduction (Dowdle and Oremland, 1998).

Selenium isotopic fractionation has been employed to monitor Se biogeochemical transformations in groundwaters and surface waters (Basu et al., 2016; Clark and Johnson, 2010; Zhu et al., 2014). In addition, Se isotopes have been used to track predominantly immobilizing processes (i.e. adsorption and reduction) in marine settings as a proxy of atmospheric and marine oxygenation (Stüeken et al., 2015). The framework used to interpret Se isotopic shifts in field settings is based on laboratory studies of isotopic fractionation during naturally relevant reactions. Abiotic reduction of Se(VI) to Se(IV) and Se(IV) to Se(0) by green rust and iron sulfides produce a maximum $\varepsilon^{82}Se/^{76}Se$ up to -11‰ and -10‰, respectively (Johnson and Bullen, 2003; Mitchell et al., 2013). Biological reduction of Se oxyanions also induces a variable range of -1.7 to -11.8‰ for Se(VI) and -1.7 to -7.8‰ for Se(IV) depending on the conditions and reduction rate (Ellis et al., 2003; Herbel et al., 2000; Schilling et al., 2020; Schilling et al., 2011). Isotopic fractionation during assimilatory reduction, meanwhile, is very small (Mitchell et al., 2012). While considerably less than reduction, isotopic fractionation is induced by adsorption of Se(IV) as well (Xu et al., 2020). Two very brief studies, of Se(0) oxidation in soils and Se(IV) oxidation by H_2O_2, showed little isotopic fractionation (Johnson, 2004; Johnson et al., 1999). However, the former instance is complicated by competing isotope effects of adsorption and reduction. The second example is arguably not environmentally relevant, as the experiment was conducted in a solution of 1.0 M NaOH with 3% H_2O_2. Significant isotope effects during oxidation could have major implications for use of the Se proxy as an indicator of marine redox conditions and tracing Se biogeochemical transformations during oxidative dissolution of Se-bearing shales.

1.4 Research Goals

The work presented here seeks to expand our current knowledge of Te, Sb, and Se isotope geochemistry for applications of tracing redox processes in modern and ancient settings.

There is considerable interest in using the Te and Sb stable isotope systems to better understand processes that concentrate these elements for economic or contaminant studies.

However, the development of MC-ICP-MS methods sensitive enough to measure average crustal concentrations of these metalloids is necessary. Chapters 2 and 3 present methods to measure isotope ratios using naturally-relevant concentrations of Te and Sb. These include a novel procedure for measurements of Te isotopes by MC-ICP-MS and development of new purification techniques for Te and Sb isotope measurements in waters and sediments. In Chapter 5, I apply the Te isotope measurements to examining Te redox cycling under variable atmospheric O_2 concentrations in Precambrian sediments.

In addition, the utility of isotope measurements in any modern or ancient setting depends on the ability to disentangle possibly multiple isotope-fractionating reactions. Well-constrained laboratory studies examining the magnitude of isotopic fractionation induced by environmentally-relevant reactions are essential to successfully interpret these isotopic variations. Chapters 3 and 4 focus on two previously overlooked but important fractionating reactions: adsorption of Sb and Te to goethite and illite and the oxidative dissolution of Se-bearing minerals.

1.5 Overview of chapters

Chapter 2 focuses on methods developed for making isotope measurements of small masses of Te in sediments. The development of Te isotope geochemistry in low-temperature environments has been hindered analytically by low crustal abundances of Te. Here, I present a method for making sensitive and precise measurements by hydride generation MC-ICP-MS. This technique can be used to measure Te mass-dependent isotope variations in sediments and waters. This study is published in the *Journal of Analytical and Atomic Spectroscopy*.

In Chapter 3, I examine the isotopic fractionation during adsorption of Sb and Te. Because Sb and Te both adsorb readily to Fe-oxides, Mn-oxides, and clays, isotopic fractionation induced by this process could become compounded with redox-driven isotopic shifts. I determined the magnitude of Te and Sb isotopic fractionation at equilibrium, and during transient phases prior to equilibrium being attained, for Te(IV), Te(VI), Sb(III) and Sb(V) adsorption to goethite and illite. The findings of this study can be applied to the interpretation of Sb and Te in oxic environments and those with fluctuating redox conditions.

Chapter 4 examines Se isotope fractionation that occurs during the oxidative dissolution of selenide-bearing minerals. This study investigates isotopic fractionation of produced Se(IV) and Se(VI) during the oxidation of ferroselite and berzelianite with hydrogen peroxide and air. The reported results point to a complicated interplay of fractionating mechanisms which in almost all conditions resulted in isotopically heavy Se(VI) relative to the bulk mineral isotopic composition.

In Chapter 5, I present results of Te isotopic variations in paleosols and ironstone formations to track the rise in atmospheric O_2 during the Precambrian. The results of this study show significant isotopic variation after the Great Oxidation Event, implying that appreciable O_2 was available for reduced Te phases to be oxidized and undergo isotope fractionation via reduction or adsorption.

1.6 References

Abin, C.A. and Hollibaugh, J.T. (2014) Dissimilatory Antimonate Reduction and Production of Antimony Trioxide Microcrystals by a Novel Microorganism. Environ. Sci. Technol. 48, 681-688.

Anbar, A.D. and Rouxel, O. (2007) Metal Stable Isotopes in Paleoceanography. Annual Review of Earth and Planetary Sciences 35, 717-746.

Ashley, P.M., Graham, B.P., Tighe, M.K. and Wolfenden, B.J. (2007) Antimony and arsenic dispersion in the Macleay River catchment, New South Wales: a study of the environmental geochemical consequences. Australian Journal of Earth Sciences 54, 83-103.

Baesman, S.M., Bullen, T.D., Dewald, J., Zhang, D., Curran, S., Islam, F.S., Beveridge, T.J. and Oremland, R.S. (2007) Formation of Tellurium Nanocrystals during Anaerobic Growth of Bacteria That Use Te Oxyanions as Respiratory Electron Acceptors. Appl. Environ. Microbiol. 73, 2135-2143.

Balistrieri, L.S. and Chao, T.T. (1990) Adsorption of selenium by amorphous iron oxyhydroxide and manganese dioxide. Geochimica et Cosmochimica Acta 54, 739-751.

Basu, A., Schilling, K., Brown, S.T., Johnson, T.M., Christensen, J.N., Hartmann, M., Reimus, P.W., Heikoop, J.M., Woldegabriel, G. and DePaolo, D.J. (2016) Se Isotopes as Groundwater Redox Indicators: Detecting Natural Attenuation of Se at an in Situ Recovery U Mine. Environmental Science & Technology 50, 10833-10842.

Berna, E.C., Johnson, T.M., Makdisi, R.S. and Basu, A. (2010) Cr Stable Isotopes As Indicators of Cr(VI) Reduction in Groundwater: A Detailed Time-Series Study of a Point-Source Plume. Environmental Science & Technology 44, 1043-1048.

Bopp, C.J., Lundstrom, C.C., Johnson, T.M., Sanford, R.A., Long, P.E. and Williams, K.H. (2010) Uranium ^{238}U/^{235}U Isotope Ratios as Indicators of Reduction: Results from an in situ Biostimulation Experiment at Rifle, Colorado, U.S.A. Environmental Science & Technology 44, 5927-5933.

Brandt, J.E., Simonin, M., Di Giulio, R.T. and Bernhardt, E.S. (2019) Beyond Selenium: Coal Combustion Residuals Lead to Multielement Enrichment in Receiving Lake Food Webs. Environ. Sci. Technol. 53, 4119-4127.

Burton, E.D., Hockmann, K. and Karimian, N. (2020) Antimony Sorption to Goethite: Effects of Fe(II)-Catalyzed Recrystallization. ACS Earth and Space Chemistry 4, 476-487.

Cidu, R., Biddau, R., Dore, E., Vacca, A. and Marini, L. (2014) Antimony in the soil–water–plant system at the Su Suergiu abandoned mine (Sardinia, Italy): Strategies to mitigate contamination. Science of The Total Environment 497-498, 319-331.

Clark, S.K. and Johnson, T.M. (2010) Selenium Stable Isotope Investigation into Selenium Biogeochemical Cycling in a Lacustrine Environment: Sweitzer Lake, Colorado. Journal of Environmental Quality 39, 2200-2210.

Colodner, D., Salters, V. and Duckworth, D.C. (1994) Ion sources for analysis of inorganic solids and liquids by MS. Analytical Chemistry 66, 1079A-1089A.

Cooper, R.G. and Harrison, A.P. (2009) The exposure to and health effects of antimony. Indian journal of occupational and environmental medicine 13, 3-10.

Csotonyi, J.T., Stackebrandt, E. and Yurkov, V. (2006) Anaerobic Respiration on Tellurate and Other Metalloids in Bacteria from Hydrothermal Vent Fields in the Eastern Pacific Ocean. Appl. Environ. Microbiol. 72, 4950.

Dowdle, P.R. and Oremland, R.S. (1998) Microbial Oxidation of Elemental Selenium in Soil Slurries and Bacterial Cultures. Environmental Science & Technology 32, 3749-3755.

Ellis, A.S., Johnson, T.M., Herbel, M.J. and Bullen, T.D. (2003) Stable isotope fractionation of selenium by natural microbial consortia. Chemical Geology 195, 119-129.

EPA (2018) 2018 Edition of the Drinking Water Standards and Health Advisories Tables. U.S. Environmental Protection Agency, Washington, DC.

Fehr, M.A., Hammond, S.J. and Parkinson, I.J. (2018) Tellurium stable isotope fractionation in chondritic meteorites and some terrestrial samples. Geochimica et Cosmochimica Acta 222, 17-33.

Fernandez, N.M., Zhang, X. and Druhan, J.L. (2019) Silicon isotopic re-equilibration during amorphous silica precipitation and implications for isotopic signatures in geochemical proxies. Geochimica et Cosmochimica Acta 262, 104-127.

Filella, M. and May, P.M. (2005) Critical appraisal of available thermodynamic data for the complexation of antimony(III) and antimony(V) by low molecular mass organic ligands.

Filella, M., Reimann, C., Biver, M., Rodushkin, I. and Rodushkina, K. (2019) Tellurium in the environment: current knowledge and identification of gaps. Environmental Chemistry 16, 215-228.

Filella, M., Williams, P.A. and Belzile, N. (2009) Antimony in the environment: knowns and unknowns. Environmental Chemistry 6, 95-105.

Fornadel, A.P., Spry, P.G., Haghnegahdar, M.A., Schauble, E.A., Jackson, S.E. and Mills, S.J. (2017) Stable Te isotope fractionation in tellurium-bearing minerals from precious metal hydrothermal ore deposits. Geochimica et Cosmochimica Acta 202, 215-230.

Fukami, Y., Kimura, J.-I. and Suzuki, K. (2018) Precise isotope analysis of tellurium by inductively coupled plasma mass spectrometry using a double spike method. Journal of Analytical Atomic Spectrometry 33, 1233-1242.

Goldfarb, R. (2015) Tellurium: The bright future of solar energy, USGS Mineral Resources Program Fact Sheet.

Guo, J., Su, L., Zhao, X., Xu, Z. and Chen, G. (2016) Relationships between urinary antimony levels and both mortalities and prevalence of cancers and heart diseases in general US population, NHANES 1999–2010. Science of The Total Environment 571, 452-460.

Hayes, S.M. and Ramos, N.A. (2019) Surficial geochemistry and bioaccessibility of tellurium in semiarid mine tailings. Environmental Chemistry 16, 251-265.

Hein, J.R., Koschinsky, A. and Halliday, A.N. (2003) Global occurrence of tellurium-rich ferromanganese crusts and a model for the enrichment of tellurium. Geochimica et Cosmochimica Acta 67, 11.

Herbel, M.J., Johnson, T.M., Oremland, R.S. and Bullen, T.D. (2000) Fractionation of selenium isotopes during bacterial respiratory reduction of selenium oxyanions. Geochimica et Cosmochimica Acta 64, 3701-3709.

Hockin, S. and Gadd, G.M. (2006) Removal of selenate from sulfate-containing media by sulfate-reducing bacterial biofilms. Environmental Microbiology 8, 816-826.

Hu, Z. and Gao, S. (2008) Upper crustal abundances of trace elements: A revision and update. Chemical Geology 253, 205-221.

Huang, F., Chakraborty, P., Lundstrom, C.C., Holmden, C., Glessner, J.J.G., Kieffer, S.W. and Lesher, C.E. (2010) Isotope fractionation in silicate melts by thermal diffusion. Nature 464, 396-400.

Jemison, N.E., Shiel, A.E., Johnson, T.M., Lundstrom, C.C., Long, P.E. and Williams, K.H. (2018) Field Application of 238U/235U Measurements To Detect Reoxidation and Mobilization of U(IV). Environmental Science & Technology 52, 3422-3430.

Johnson, T.M. (2004) A review of mass-dependent fractionation of selenium isotopes and implications for other heavy stable isotopes. Chemical Geology 204, 201-214.

Johnson, T.M. and Bullen, T.D. (2003) Selenium isotope fractionation during reduction by Fe(II)-Fe(III) hydroxide-sulfate (green rust). Geochimica et Cosmochimica Acta 67, 413-419.

Johnson, T.M., Herbel, M.J., Bullen, T.D. and Zawislanski, P.T. (1999) Selenium isotope ratios as indicators of selenium sources and oxyanion reduction. Geochimica et Cosmochimica Acta 63, 2775-2783.

Kashiwabara, T., Oishi, Y., Sakaguchi, A., Sugiyama, T., Usui, A. and Takahashi, Y. (2014) Chemical processes for the extreme enrichment of tellurium into marine ferromanganese oxides. Geochimica et Cosmochimica Acta 131, 150-163.

Kulp, T.R., Miller, L.G., Braiotta, F., Webb, S.M., Kocar, B.D., Blum, J.S. and Oremland, R.S. (2014) Microbiological Reduction of Sb(V) in Anoxic Freshwater Sediments. Environ. Sci. Technol. 48, 218-226.

Lee, D.S. and Edmond, J.M. (1985) Tellurium species in seawater. Nature 313, 782-785.
Leuz, A.-K., Mönch, H. and Johnson, C.A. (2006) Sorption of Sb(III) and Sb(V) to Goethite: Influence on Sb(III) Oxidation and Mobilization. Environmental Science & Technology 40, 7277-7282.

Leverett, P., Reynolds, J.K., Roper, A.J. and Williams, P.A. (2012) Tripuhyite and schafarzikite: two of the ultimate sinks for antimony in the natural environment. Mineralogical Magazine 76, 891-902.

Li, J., Wang, Q., Oremland, R.S., Kulp, T.R., Rensing, C. and Wang, G. (2016) Microbial Antimony Biogeochemistry: Enzymes, Regulation, and Related Metabolic Pathways. Appl. Environ. Microbiol. 82, 5482.

Loscalzo, J. (2014) Keshan disease, selenium deficiency, and the selenoproteome. New England Journal of Medicine 370, 1756-1760.

Losi, M.E., Amrhein, C. and Frankenberger, W.T., Jr. (1994) Environmental biochemistry of chromium. Reviews of environmental contamination and toxicology 136, 91-121.

Lyons, T.W., Reinhard, C.T. and Planavsky, N.J. (2014) The rise of oxygen in Earth's early ocean and atmosphere. Nature 506, 307.

Mackinney, J. (2016) Antimony isotopes as indicators of redox reactions in aqueous systems: fractionation during Sb(V) reduction by sulfide and isotope exchange kinetics between dissolved Sb(III) and Sb(V), IDEALS.

Mebane, C.A., Mladenka, G., Van Every, L., Williams, M.L., Hardy, M.A. and Garbarino, J.R. (2014) Selenium in the upper Blackfoot River watershed, southeastern Idaho, 2001-12. Scientific Investigations Report, 44.

Missen, O.P., Ram, R., Mills, S.J., Etschmann, B., Reith, F., Shuster, J., Smith, D.J. and Brugger, J. (2020) Love is in the Earth: A review of tellurium (bio)geochemistry in surface environments. Earth-Science Reviews 204, 103150.

Mitchell, K., Couture, R.-M., Johnson, T.M., Mason, P.R.D. and Van Cappellen, P. (2013) Selenium sorption and isotope fractionation: Iron(III) oxides versus iron(II) sulfides. Chemical Geology 342, 21-28.

Mitchell, K., Mason, P.R.D., Van Cappellen, P., Johnson, T.M., Gill, B.C., Owens, J.D., Diaz, J., Ingall, E.D., Reichart, G.-J. and Lyons, T.W. (2012) Selenium as paleo-oceanographic proxy: A first assessment. Geochimica et Cosmochimica Acta 89, 302-317.

Ohlendorf, H.M., Hothem, R.L., Bunck, C.M. and Marois, K.C. (1990) Bioaccumulation of selenium in birds at Kesterson Reservoir, California. Archives of Environmental Contamination and Toxicology 19, 495-507.

Okkenhaug, G., Amstätter, K., Lassen Bue, H., Cornelissen, G., Breedveld, G.D., Henriksen, T. and Mulder, J. (2013) Antimony (Sb) Contaminated Shooting Range Soil: Sb Mobility and Immobilization by Soil Amendments. Environ. Sci. Technol. 47, 6431-6439.

Ollivier, P.R.L., Bahrou, A.S., Church, T.M. and Hanson, T.E. (2011) Aeration controls the reduction and methylation of tellurium by the aerobic, tellurite-resistant marine yeast Rhodotorula mucilaginosa. Appl. Environ. Microbiol. 77, 4610-4617.

Olsen, N.J., Mountain, B.W. and Seward, T.M. (2018) Antimony(III) sulfide complexes in aqueous solutions at 30°C: A solubility and XAS study. Chemical Geology 476, 233-247.
Peak, D. (2006) Adsorption mechanisms of selenium oxyanions at the aluminum oxide/water interface. Journal of Colloid and Interface Science 303, 337-345.

Peak, D. and Sparks, D.L. (2002) Mechanisms of Selenate Adsorption on Iron Oxides and Hydroxides. Environ. Sci. Technol. 36, 1460-1466.

Perez-D'Gregorio, R.E., Miller Rk Fau - Baggs, R.B. and Baggs, R.B. (1988) Maternal toxicity and teratogenicity of tellurium dioxide in the Wistar rat: relationship to pair-feeding. Reproductive Toxicology 2, 55-61.

Perkins, W.T. (2011) Extreme selenium and tellurium contamination in soils--an eighty year-old industrial legacy surrounding a Ni refinery in the Swansea Valley. The Science of the total environment 412-413, 162-169.

Presser, T.S. and Swain, W.C. (1990) Geochemical evidence for Se mobilization by the weathering of pyritic shale, San Joaquin Valley, California, U.S.A. Applied Geochemistry 5, 703-717.

Qin, H.-B., Takeichi, Y., Nitani, H., Terada, Y. and Takahashi, Y. (2017) Tellurium Distribution and Speciation in Contaminated Soils from Abandoned Mine Tailings: Comparison with Selenium. Environ. Sci. Technol. 51, 6027-6035.

Ramos-Ruiz, A., Field, J.A., Wilkening, J.V. and Sierra-Alvarez, R. (2016) Recovery of Elemental Tellurium Nanoparticles by the Reduction of Tellurium Oxyanions in a Methanogenic Microbial Consortium. Environ. Sci. Technol. 50, 1492-1500.

Resongles, E., Freydier, R., Casiot, C., Viers, J., Chmeleff, J. and Elbaz-Poulichet, F. (2015) Antimony isotopic composition in river waters affected by ancient mining activity. Talanta 144, 851-861.

Robbins, L.J., Lalonde, S.V., Planavsky, N.J., Partin, C.A., Reinhard, C.T., Kendall, B., Scott, C., Hardisty, D.S., Gill, B.C., Alessi, D.S., Dupont, C.L., Saito, M.A., Crowe, S.A., Poulton, S.W., Bekker, A., Lyons, T.W. and Konhauser, K.O. (2016) Trace elements at the intersection of marine biological and geochemical evolution. Earth-Science Reviews 163, 323-348.

Rouxel, O., Ludden, J. and Fouquet, Y. (2003) Antimony isotope variations in natural systems and implications for their use as geochemical tracers. Chemical Geology 200, 25-40.

Sabaty, M., Avazeri, C., Pignol, D. and Vermeglio, A. (2001) Characterization of the Reduction of Selenate and Tellurite by Nitrate Reductases. Applied and Environmental Microbiology 67, 5122.

Schilling, K., Basu, A., Wanner, C., Sanford, R.A., Pallud, C., Johnson, T.M. and Mason, P.R.D. (2020) Mass-dependent selenium isotopic fractionation during microbial reduction of seleno-oxyanions by phylogenetically diverse bacteria. Geochimica et Cosmochimica Acta 276, 274-288.

Schilling, K., Johnson, T.M., Dhillon, K.S. and Mason, P.R.D. (2015) Fate of Selenium in Soils at a Seleniferous Site Recorded by High Precision Se Isotope Measurements. Environ. Sci. Technol. 49, 9690-9698.

Schilling, K., Johnson, T.M. and Wilcke, W. (2011) Isotope Fractionation of Selenium During Fungal Biomethylation by Alternaria alternata. Environmental Science & Technology 45, 2670-2676.

Schirmer, T., Koschinsky, A. and Bau, M. (2014) The ratio of tellurium and selenium in geological material as a possible paleo-redox proxy. Chemical Geology 376, 44-51.

Seal, R.R.I., Schulz, K.J., DeYoung, J.J.H., Sutphin, D.M., Drew, L.J., Carlin Jr, J.F. and Berger, B.R. (2017) Antimony. Professional Paper, 30.

Smithers, R.M. and Krouse, H.R. (1968) Tellurium isotope fractionation study. Can. J. Chem. 46, 583-591.

Stüeken, E.E., Buick, R., Bekker, A., Catling, D., Foriel, J., Guy, B.M., Kah, L.C., Machel, H.G., Montañez, I.P. and Poulton, S.W. (2015) The evolution of the global selenium cycle: Secular trends in Se isotopes and abundances. Geochimica et Cosmochimica Acta 162, 109-125.

Sutter, M.E., Thomas, J.D., Brown, J. and Morgan, B. (2008) Selenium Toxicity: A Case of Selenosis Caused by a Nutritional Supplement. Annals of Internal Medicine 148, 970-971.

Tanner, J.T. and Ehmann, W.D. (1967) The abundance of antimony in meteorites, tektites and rocks by neutron activation analysis. Geochimica et Cosmochimica Acta 31, 2007-2026.

Teng, F., Wang, S. and Moynier, F. (2019) Tracing the formation and differentiation of the Earth by non-traditional stable isotopes. Science China Earth Sciences 62, 1702-1715.

Teng, F.W., JM; Dauphas, N (2017) Non-traditional Stable Isotopes. Mineralogical Society of America and the Geochemical Society, Chantilly, VA.

Valley, J.C., DRE (2001) Stable Isotope Geochemistry. Mineralogical Society of America, Washington, DC.

von Uexküll, O., Skerfving, S., Doyle, R. and Braungart, M. (2005) Antimony in brake pads-a carcinogenic component? Journal of Cleaner Production 13, 19-31.

Wang, X., He, M., Xi, J. and Lu, X. (2011) Antimony distribution and mobility in rivers around the world's largest antimony mine of Xikuangshan, Hunan Province, China. Microchemical Journal 97, 4-11.

Watterson, J.R., Gott, G.B., Neuerburg, G.J., Lakin, H.W., Cathrall, J.B., Butt, C.R.M. and Wilding, I.G.P. (1977) Tellurium, a Guide to Mineral Deposits, Developments in Economic Geology. Elsevier, pp. 31-48.

Westerhoff, P., Prapaipong, P., Shock, E. and Hillaireau, A. (2008) Antimony leaching from polyethylene terephthalate (PET) plastic used for bottled drinking water. Water Research 42, 551-556.

Wiederhold, J.G. (2015) Metal Stable Isotope Signatures as Tracers in Environmental Geochemistry. Environmental Science & Technology 49, 2606-2624.

Wiklund, J.A., Kirk, J.L., Muir, D.C.G., Carrier, J., Gleason, A., Yang, F., Evans, M. and Keating, J. (2018) Widespread Atmospheric Tellurium Contamination in Industrial and Remote Regions of Canada. Environ. Sci. Technol. 52, 6137-6145.

Wilson, N., Webster-Brown, J. and Brown, K. (2012) The behaviour of antimony released from surface geothermal features in New Zealand. Journal of Volcanology and Geothermal Research 247-248, 158-167.

Wilson, N.J., Craw, D. and Hunter, K. (2004) Contributions of discharges from a historic antimony mine to metalloid content of river waters, Marlborough, New Zealand. Journal of Geochemical Exploration 84, 127-139.

Xu, W., Zhu, J.-M., Johnson, T.M., Wang, X., Lin, Z.-Q., Tan, D. and Qin, H. (2020) Selenium isotope fractionation during adsorption by Fe, Mn and Al oxides. Geochimica et Cosmochimica Acta 272, 121-136.

Yarema, M.C. and Curry, S.C. (2005) Acute Tellurium Toxicity From Ingestion of Metal-Oxidizing Solutions. Pediatrics 116, e319-e321.

Zhu, J.-M., Johnson, T.M., Clark, S.K., Zhu, X.-K. and Wang, X.-L. (2014) Selenium redox cycling during weathering of Se-rich shales: A selenium isotope study. Geochimica et Cosmochimica Acta 126, 228-249.

Zweibel, K. (2010) The Impact of Tellurium Supply on Cadmium Telluride Photovoltaics. Science 328, 699-701.

CHAPTER 2: MEASUREMENTS OF MASS-DEPENDENT TE ISOTOPIC VARIATION BY HYDRIDE GENERATION MC-ICP-MS[1]

Abstract

Tellurium (Te) stable isotope measurements have the potential to serve as tracers of Te mobility and redox conditions in modern and ancient environments. Here, we present a method to measure Te isotope ratios by MC-ICP-MS utilizing a hydride generation system to efficiently deliver Te to the plasma, in combination with a ^{120}Te-^{124}Te double spike. This approach allows for precise δ^{130}Te/^{126}Te (2σ: 0.09‰) measurements while using less than 8.75 ng of natural Te. Although hydride generation methods usually produce higher sensitivity than more conventional methods, for Te, the sensitivity is similar, on our instrument, to that achieved using a desolvating nebulizer. Nonetheless, hydride generation has an advantageous ability to exclude interfering elements such as Ba and allow analysis of samples without chemical separation of Te in some cases. We also demonstrate successfully a modified ion exchange procedure to separate various matrix components and isobaric interferences from Te in natural sediments. Analyses of multiple digestions of USGS standard reference materials, mine tailings, ancient sediments, and soils utilizing this approach show the largest spread in terrestrial Te isotopic composition to date (δ^{130}Te/^{126}Te ~1.21‰) and a lack of detectable mass-independent fractionation.

---

[1] This chapter is published as Wasserman, N.L. and Johnson, T.M. (2020) Measurements of mass-dependent Te isotopic variation by hydride generation MC-ICP-MS. *Journal of Atomic and Analytical Spectroscopy*. 35, 307-319. DOI: 10.1039/C9JA00244H

2.1 Introduction

Tellurium (Te) is an economically valuable metalloid often incorporated into photovoltaic cell technology and nanotechnology (Zweibel, 2010). Estimates show that demand for Te may increase as much as 100-fold by 2030, and this may lead to increasing instances of mining-related contamination as observed around Cu smelters (Canada) and a nickel refinery (UK) (Goldfarb, 2015; Perkins, 2011). Exposure to high concentrations of Te can result in liver and kidney necrosis and collapse of the respiratory and circulatory systems (Gerhardsson, 2015; Yarema and Curry, 2005). Tellurium is currently extracted primarily as a byproduct of copper solvent extraction-electrolytic refining (Zweibel, 2010). This method will most likely be phased out due to more efficient solvent extraction methods for copper refining that do not involve Te separation (Goldfarb, 2015). Accordingly, both exploration for Te ores and increased occurrence of industrial Te contamination may occur, and there is a greater need to examine low-temperature abiotic and microbial processes that control Te enrichment in ores, and Te transport in contaminated water.

While Te has a low crustal abundance (~1-3 ng g^{-1}) (Hein et al., 2003), certain geochemical processes can concentrate Te. A compilation of soil and sediment samples indicates that Te concentrations range from less than 5 to 100 ng g^{-1} and past studies have see enrichments up to 50,000 times in ferromanganese crusts (Belzile and Chen, 2015; Hein et al., 2003). Similar to other group 16 elements, selenium and sulfur, Te is found in four nominal oxidation states (-2, 0, +4, +6). Tellurium can be mobile in the +4 and +6 states as a soluble oxyanion, whereas in the reduced states it tends to have low solubility, forming solid tellurides or elemental Te nanorods (Goldfarb, 2015). In oxic marine surface waters, Te(IV) and Te(VI) exist as oxyanions in roughly equal proportions (Lee and Edmond, 1985). Both the irregularly-coordinated tellurite

(TeO_3^{2-}) and octahedrally-coordinated tellurate (TeO_4^{2-}) species are scavenged by Fe- and Mn-oxy(hydrox)ides, although tellurite adsorbs more strongly (Qin et al., 2017). Unlike Se, Te is not a micronutrient. Several studies, though, have observed microbial dissimilatory reduction of Te(IV) and Te(VI) to Te(0) nanorods or methylated tellurides (Baesman et al., 2007; Taylor, 1999).

Because a variety of abiotic and microbially-mediated redox processes influence Te mobility, there is increasing interest to develop the element as an indicator of paleoredox conditions. Decades of studies have utilized various isotopic and chemical proxies to provide constraints on the relative oxidizing power of the atmospheric and oceanic systems. Geochemical redox proxies indicate that, from the Great Oxygenation Event (~2.4 Ga) until the next major oxygenation event at 0.8 Ga, atmospheric oxygen remained low, while certain portions of the ocean (shallow oases and deep marine environments) may have been partially oxygenated (Hardisty et al., 2017; Planavsky et al., 2014; Planavsky et al., 2018). Such decoupling highlights the need for the development of additional geochemical tools, like Te isotopes, to trace distinct redox conditions of marine and terrestrial environments.

With eight stable isotopes, Te stable isotope measurements may be useful as tracers of redox processes that affect Te mobility. Similar to the Se, Cr, and U isotope systems, Te mass-dependent isotopic fractionation may occur during reduction or oxidation by abiotic or biological reactants (Bopp et al., 2010; Ellis et al., 2003). Theoretical calculations by Smithers and Krouse (1968) estimated a 6‰ difference between $^{130}Te/^{125}Te$ of TeO_4^{2-} and H_2Te at isotopic equilibrium. (Baesman et al., 2007) observed a kinetic Te isotopic fractionation factor of $\varepsilon \sim -2.0$ to -5.0‰ in laboratory reduction of TeO_4^{2-} and TeO_3^{2-} by sulfite, cysteine, and two bacterial cultures amended with acetate (Baesman et al., 2007). The fractionation factor, ε, is equivalent to

1000‰ x (α-1), where α equals the ratio of the $^{130}Te/^{125}Te$ of the instantaneous product relative to the reactant. Recent surveys of Te ores (range of ~2‰) and ordinary chondrites (range of ~6.3‰) and sediments (range of ~0.85‰) also show significant isotopic fractionation (Fehr et al., 2018; Fornadel et al., 2017; Fukami et al., 2018). However, attempts to examine isotopic variation in soil samples (typically <20 ng mL^{-1}) have been limited by the inability of analytical techniques to measure the very small masses found in many materials.

Here, we present a method for Te stable isotope measurements that allows for small masses of natural Te (<8.75 ng) without a need for a Ba correction, using a hydride generation sample introduction system in combination with a ^{120}Te-^{124}Te double spike. We also present an ion exchange purification technique modified from previous studies to achieve high recovery while separating Te from typical sample matrix components (e.g., Fe) (Wang and Becker, 2014) and isobaric interferences (e.g., Sn) (Forrest et al., 2009). With this method, the Te isotope approach can be more broadly applied to improve understanding of modern contaminated systems, paleoredox states of ancient earth systems, igneous systems, and modern critical zone processes.

2.2 Materials and Methods

2.2.1 Reagents

Acids for digestion and chemical separation of samples were prepared from American Chemical Society (ACS)-Certified HCl (Macron Fine Chemicals), ACS-Certified HNO_3 (Fisher Chemical), and HF (99.99% purity, Alfa Aesar). Additional distillation was not required as the acid blanks contained less than 0.1 ng mL^{-1} Te. The oxidizing solution for Te was prepared with potassium persulfate (Certified ACS, Fisher) powder. A Millipore Milli-Q Integral water purification system (Merck Millipore, USA) provided ultrapure water (18.2 MΩ) with which all reagent solutions were made. $NaBH_4$ (>98%, Acros Organics) and NaOH (Certified ACS, Fisher) powdered reagents were utilized to prepare the reductant solution used for hydride generation.

2.2.2 Samples and standards

Three Te standards, National Institute of Standards and Technology (NIST) SRM 3156 Te concentration standard (Lot no. 140830), Alfa Aesar Na_2TeO_3 powder reagent (99.5% metals basis, lot no. M27C052), and Alfa Aesar $H_2TeO_4 \bullet 2H_2O$ powder reagent (99% metals basis, lot no. Y05A029), were used to evaluate long-term precision. Single batches of these stock solutions of these reagents were used as in-house standards to assess precision. All solutions were prepared by dissolving the powder in 1 M HCl. A Te standard solution in 5% HNO_3 (Spex CertiPrep) was used as a concentration standard for measurements by single collector inductively coupled plasma-mass spectrometry (ICP-MS) (Thermo Scientific, iCAP Q).

Seven United States Geological Survey geochemical reference materials were digested and measured. Three of these standards, Nod-P-1, SGR-1 and MAG-1 have been measured previously (Fehr et al., 2018; Fukami et al., 2018). Briefly, Nod-P-1 is a diagenetic manganese nodule from the Pacific Ocean, SGR-1 is a shale powder from the Green River Formation, and MAG-1 is a marine mud from the Wilkinson Basin, Gulf of Maine (Flanagan and Gottfried, 1980). The USGS standard SCO-1, an Upper Cretaceous silty marine shale, has no published Te isotope values. One USGS soil sample, C-320293, is a topsoil taken from shrubland in the Humboldt-Toiyabe Forest in Nevada, USA (Smith et al., 2014).

Several mine tailings were collected from millsites from across the western United States with all coordinates recorded using NAD83 spheroid and WGS84 datum. The Delamar mining district (Lincoln County, NV; coordinates: 37.45892, -114.77739) was mined for gold from 1892 through 1909 leaving at least 408,000 metric tons of mine tailings at the site. Sample “Delamar big tailings surface” (0-2 cm) was collected from the site, “big tailings pile”. This site was characterized by smaller particle sizes, higher extent of oxidation, and higher concentrations of potentially toxic elements (Hayes and Ramos, 2019). The Ute Ulay mill (Hinsdale County, CO; coordinates: 38.0192289, -107.3768862) intermittently processed lead and zinc ore since 1874. More recently, tailings from the Golden Wonder, a nearby gold telluride deposit, have been deposited at the site since the 1990’s (Smith, 2012). Samples, “Ute Ulay surface” (0-2 cm) and “Ute Ulay deep” (83-90 cm), were collected from a fresh tailings pit there. Sample “Vulcan precipitate” is a precipitate found in weathered mine tailings, dominantly copiapite ($Fe^{2+}Fe^{3+}_4(SO_4)_6(OH)_2{\bullet}20H_2O$), collected from the soil surface under the historic Vulcan mill structure (Gunnison County, CO; coordinates: 38.3447176, -107.0062077). Sample “Masonic surface” (0-2 cm) was collected from the streambed just downstream of the historic Masonic Mill (Mono County, CA; coordinates 38.3673, -119.12059).

Two ancient sediments were also digested. The first sample “CLRD-3.0” is from the 2.45 Ga Cooper Lake paleosol (Ontario, Canada). The paleosol, made up of dominantly quartz and clay minerals with lesser amounts of pyrite, is developed on the Algomon granite at the base of the Huronian Supergroup (Sutton and Maynard, 1993). It is interpreted to have formed under anoxic atmospheric conditions (Babechuk et al., 2019). The second sample (CLG-1) originates from the 1.650 Ga Mesoproterozoic Chuanlinggou Formation (Northern China) (Gao L.Z., 2008). It is composed of primarily oolitic iron deposits, which were deposited in a ferruginous and mildly oxic water column (Li et al., 2015).

2.2.3 Digestion and purification

For samples with lower concentrations of Te (CLRD-3.0 and CLG-1) up to 0.4 g of sample was digested, while 0.02 g of “Masonic Surface”, “Vulcan Yellow Precipitate”, and “Delamar big tailings surface” samples was used. For all other samples approximately 0.2 g was used for digestion. Depending on the mass required, samples were digested in 4 or 8 mL reverse aqua regia (1:3 HCl: HNO_3 ratio) on a hot plate at 110°C for 24 hours. This digestion procedure was sufficient to release Te associated with non-silicate phases (e.g. clays, sulfides, Fe-oxyhydroxides), which are present in all of the samples. For silicate-rich matrices reverse aqua regia has been adequate to release 85% to 100% of the Te present due to its association with sulfide and oxide phases (Yierpan et al., 2018). Therefore, the small contribution of silicate phases in our samples should not influence our recovery. Residual solids were separated from the supernatant, which was evaporated to dryness at 90°C. Unlike Se, where >80% of Se can be volatilized during evaporation in HCl matrices, little volatilization of Te occurs in HCl or HNO_3 at this temperature (Chen et al., 2016). Small losses of Te by volatilization and possible isotopic fractionation are corrected by the Te double spike addition prior to digestion. Subsequently, the samples were brought up in 4 mL 6 M HCl and heated on the hot plate at 110°C for 2 hours to ensure all Te was converted to Te(IV). The ^{120}Te-^{124}Te double spike (+4 valence; see section 2.4) was added to the samples before digestion.

All chemical purification was performed in laminar flow HEPA-filtered clean hoods contained in a Class 10,000 Clean Lab (University of Illinois at Urbana-Champaign). The mass of Te loaded on the column ranged from 8 to 300 ng Te. For samples requiring more than 0.5 g of digested material (<15 ng Te), parallel column separations can be utilized with the expectation of a higher blank contribution. Separation from the majority of the interfering elements (Fe, matrix) was achieved using AG1-X8 anion exchange resin columns (3 mL bed volume; 100-200 mesh, BioRad Laboratories) following a modified procedure from Fehr et al. (2004) and Wang and Becker (2014). Briefly, resin was conditioned in a Poly-Prep 10 mL column (BioRad Laboratories) with 8 mL 6 M HCl after which the sample was loaded, with Te retained. The column was rinsed with 6 mL of 6 M HCl to elute Se and other matrix elements (Co^{2+}, Ni^{2+}, Cu^{2+}, and Pb^{2+}) followed by 5 M HF, which removed most of the Fe, a suppressant of H_2Te formation during hydride generation (Brennecka et al., 2017). Subsequently, 4 mL 9 M HCl was added to further elute matrix elements. To remove residual Fe, 5 mL of 2 M HCl was added before eluting Te(IV) with 8 mL of 1 M HNO_3.

Samples were evaporated to dryness at 90°C and further digested with five drops of concentrated HNO_3 followed by five drops of concentrated HCl. Once dried down, the residue was dissolved in 0.1 M HCl containing freshly made 0.02 M $K_2S_2O_8$. Samples were heated on a hot plate at 110°C for 90 minutes, converting all Te(IV) to Te(VI). After oxidation, samples were further purified with a 1 mL cation exchange column (AG50W-X8, 200-400 mesh, BioRad Laboratories) to remove Sn and Fe in a 10 mL Poly-Prep column (BioRad Laboratories). The columns were conditioned with 0.1 M HCl, after which, the sample was loaded followed by 5 mL of 0.1 M HCl. The eluent was immediately collected, as H_2TeO_4 is a neutrally charged species and does not adsorb to the resin. Residual Fe(III) was retained on the column along with most of Sn(IV) at dilute HCl concentrations (Fehr et al., 2004). Once dried down, samples were again digested with 2 drops of concentrated HNO_3 followed by concentrated HCl.

In some cases, to further remove Sn from samples, samples were acidified to 0.4 M HCl and passed through a BioRad column following a modified procedure from Wang et al. (2017). A 1 mL AG1-X8 (100-200 mesh) resin bed was conditioned with 10 mL 0.4 M HCl. Once the sample was loaded, as Te(VI), the elutant was collected immediately along with the next 5 mL of 0.4 M HCl. The sample was then dried down, dissolved in 2 mL 5 M HCl and heated at 110°C for at least 2 hours to fully reduce Te(VI) to Te(IV).

2.2.4 Double spike

A ^{120}Te-^{124}Te double spike (2% HNO_3) was used to correct for instrumental mass bias and any isotopic fractionation that might occur during sample preparation. Double spike addition is a well-established method to precisely correct for instrumental mass bias (Eugster et al., 1969; Johnson and Beard, 1999; Russell, 1971). ^{120}Te and ^{124}Te were chosen as the spike isotopes based on the minimization of error (Rudge et al., 2009). The isotopic composition of the double spike was determined by hydride generation measurements, corrected for mass bias determined from NIST SRM 3156 measurements before and after the double spike. The double spike composition was corrected for Sn and Xe interferences. Memory of the natural Te standard was removed completely before double spike measurement. The Te spikes were of high purity, containing 98.8% ^{120}Te and 93.0% ^{124}Te. The spikes were mixed to create solution with 54.40% ^{120}Te and 43.60% ^{124}Te (on a molar basis), which is close to the optimal ratio determined using the methods of Rudge et al. (2009) (57% and 43%) using ^{126}Te and ^{130}Te as the inversion isotopes. The concentration of the double spike solution was calibrated based on measurements of a spiked Te concentration standard (Spex CertiPrep).

2.2.5 Mass spectrometry

All measurements were made on a Nu Plasma HR MC ICP-MS (Nu Instruments, UK) in low-resolution mode, with Te introduced to the plasma via a custom –built hydride generation system. The system generates $H_2Te_{(g)}$ by reacting Te(IV) in 4 M HCl (1.0 mL min^{-1}) with an inline solution of 0.2 wt. % $NaBH_4$ and 0.2 wt. % NaOH (0.5 mL min^{-1}). A frit-based gas-liquid separator with an Ar flow of about 0.03 L min^{-1} stripped the H_2Te from the liquid, which was then passed through a 0.2 μm polytetrafluoroethylene (PTFE) filter to remove aerosols, and merged into Ar carrier gas (1.4 L min^{-1}). This allows for an efficient transfer of the gaseous H_2Te into the mass spectrometer. Importantly, only elements that can form gaseous hydrides and other volatile species can be transferred into the mass spectrometer through this method, excluding many potential isobaric interferences such as Ba, and molecular interferences from Mo, Nb, Zr, Cd, Pd, and Sr.

Several analyses were made using a desolvating nebulizer (CETAC, Aridus II DSN) to assess the advantages and disadvantages associated with each technique. A nebulizer Ar gas flow 1.0 L min^{-1} and sweep gas flow of 9.63 L min^{-1} allowed for a 0.07 mL min^{-1} sample uptake rate using a PFA MicroFlow nebulizer (Elemental Scientific).

The measurement routine used Faraday collectors on the Nu Plasma as shown in Table 2.1. Collectors were connected to amplifiers with standard 10^{11} Ω resistors on all collectors except the one in the H5 position (^{130}Te) which has been fitted with a 10^{10} Ω resistor. This facilitates high-precision ^{238}U/^{235}U measurements by allowing measurement at high ^{238}U intensities (up to 10^{-9} A). Unfortunately, reverting to the 10^{11} Ω resistor was not feasible during the course of this study and this resulted in greater baseline noise in the ^{130}Te measurement (see discussion). The measurement routine was set up such that ^{124}Te is in the Axial position (Table 2.1). In L4, ^{118}Sn, a common impurity in samples and the $NaBH_4$ reagent, is monitored to enable corrections for Sn interferences on ^{120}Te and ^{124}Te. SnH^+ sourced from the $NaBH_4$ was subtracted by on-peak zeroes, while that from the samples was such that ^{120}Sn/^{120}Te <0.02. In addition, ^{132}Xe was measured on collector H6 to enable correction for small Xe interferences on ^{130}Te, ^{128}Te, ^{126}Te and ^{124}Te. Baseline analysis of mass 120 without hydride generation revealed a ^{40}Ar^{40}Ar^{40}Ar interference of 2-3 mV, which was corrected for by on-peak zeroes. While we found no evidence for a significant SbH^+ interference on mass 124, mass 123 (^{123}Sb and ^{123}Te) was monitored. A TeH^+ correction removed hydride interferences on ^{125}Te and ^{126}Te. After each measurement, $^{124}Te^1H^+$ or $^{125}Te^1H^+$ was subtracted based on the intensity of ^{124}Te and ^{125}Te and a constant TeH^+/Te. At the beginning of each session, overspiked and underspiked samples were measured to validate and/or adjust the TeH^+/Te used for the correction. ^{125}Te is particularly sensitive to the TeH^+ interference, as the contribution of $^{124}TeH^+$ derived from the relatively high-intensity spike isotope, ^{124}Te, strongly impacts the somewhat rare ^{125}Te isotope. Given the average TeH^+/Te of 0.0001, $^{123}TeH^+$ interference on ^{124}Te was not corrected for, as $^{123}TeH^+$ at normal intensities and spike to sample ratios would be less than 0.002‰ of the intensity of the ^{124}Te signal. ^{130}Ba and ^{132}Ba, while of low abundance, can be significant interferences on ^{130}Te and ^{132}Xe as observed by Fehr et al. (2018) and Fukami et al. (2018). Similar to Brennecka et al. (2017), we did not observe significant ^{137}Ba above baseline values during hydride generation for samples containing up to 1V on ^{137}Ba while using the DSN. Ba does not readily form hydrides in the conditions utilized and was not corrected for in our sample routine.

Interferences were partially corrected by subtraction after on-peak baseline and background measurements of a blank 4 M HCl solution with an integration time of 100 sec, immediately prior to peak centering on ^{128}Te and sample measurement. Residual Xe and Sn were further subtracted by measuring ^{132}Xe and ^{118}Sn during each integration of sample measurement and calculating the interferences using assumed natural isotopic compositions and the mass bias determined from the double spike. This was done in an iterative way as part of the double spike data reduction, so the interferences were accounted for in the mass bias determinations and vice-versa. Samples were measured over 5 blocks of 10 measurements, each integrated over 3 seconds. A total of 3.5 minutes of sample consumption time was required, followed by 6.6 minutes rinse time before the next analysis.

In order to compare our results to previous studies, we normalized our samples to NIST SRM 3156. While previous studies have reported the isotope ratio ^{130}Te/^{125}Te (Brennecka et al., 2017; Fehr et al., 2018; Fukami et al., 2018), we report the ratio ^{130}Te/^{126}Te due to its lesser uncertainty: ^{126}Te is 2.7 times more abundant than ^{125}Te and the smaller measurement uncertainty using ^{126}Te more than compensated for the lower sensitivity of the ^{130}Te/^{126}Te ratio (4 D mass difference) to a given fractionation relative to the ^{130}Te/^{125}Te ratio (5 D mass difference). An analysis of counting statistics-related noise and baseline noise revealed that ^{130}Te/^{125}Te should have an uncertainty 1.6x larger than ^{130}Te/^{126}Te at normal intensity. We observed that on average the uncertainty of δ^{130}Te/^{125}Te was 1.5 times that of δ^{130}Te/^{126}Te over 4 analytical sessions. In addition to δ^{130}Te/^{126}Te, δ^{128}Te/^{126}Te and δ^{125}Te/^{126}Te were also determined independently to monitor for certain analytical problems such as uncorrected Xe, Sn, and hydride (^{124}TeH^{+} and ^{125}TeH^{+}) interferences. Over an analytical session, rejection of an analysis due to large uncorrected Xe, Sn, or hydride residuals was uncommon once samples were effectively separated from Sn (see Section 3.5).

Standards and samples were spiked based on the optimal molar proportion of spike to sample ~0.98 as discussed in Section 3.3. All standards, once spiked, were heated in 5 M HCl at 100°C for 2 hours to reduce Te(VI) to Te(IV). High-precision measurements typically required a natural Te concentration of 2.5 ng mL^{-1}. All bracketing standards were diluted such that ^{130}Te measured to ~1.5V, while all samples were diluted such that ^{130}Te was 1.2 – 2 V. Given the 3.5 minutes required for measurement, one sample measurement typically consumed 8.75 ng natural Te. Afterward, Te was rinsed out by admitting 0.5 M HCl for 70 s, followed by three cycles of 2

M HCl for 70 s each. An iterative routine was used to solve the double spike equations using ^{120}Te, ^{124}Te, ^{126}Te and ^{130}Te to derive δ^{130}Te/^{126}Te results, ^{120}Te, ^{124}Te, ^{126}Te and ^{128}Te to derive δ^{128}Te/^{126}Te results, and ^{120}Te, ^{124}Te, ^{125}Te, and ^{126}Te to derive δ^{125}Te/^{126}Te results.[35] Each group of four samples was bracketed with NIST SRM 3156 standard analyses before and after; sample results were normalized to the average Te isotope measurement of this standard over the analytical session.

2.2.6 Concentration measurement

To estimate the concentration of each sample for accurate spike addition, 0.2 mL of the digested samples were diluted in 2 mL of Milli-Q water to a final matrix of 5% HNO_3 and 0.1% HCl. Samples were measured on an iCAP Q ICP-MS (Thermo Fisher Scientific). The mass ^{125}Te was measured over 5 cycles with a 0.03 second integration time. An internal standard, consisting of ^{115}In, was mixed with the sample via an inline addition to correct for instrumental drift and matrix effects. The limit of detection was 0.02 ng mL^{-1} Te and the limit of quantification was 0.31 ng mL^{-1}.

Isotope dilution was used to obtain more precise concentrations. The double spike data reduction calculations yield a highly precise determination of the spike:sample ratio, allowing calculating of the sample concentration if the double spike concentration is known.

2.3 Results and Discussion

2.3.1 Sensitivity and memory

Measurement of Te isotope ratios of natural sediments requires a high-sensitivity measurement method. Average soils contain typically <5 to 100 ng g^{-1} Te (Belzile and Chen, 2015). Accordingly, it is very helpful if precise measurements of soils samples can be obtained using less than 10 ng Te per analysis. Sensitivity during the course of this study was on average

600 mV for ^{130}Te for a 1 ng mL^{-1} Te solution, which for a 1.0 mL min^{-1} uptake rate, delivers 1.0 ng min^{-1}. This sensitivity arises from the high efficiency of the hydride generation system in delivering Te to the plasma. Although the sample uptake rate is high, the relatively short analysis time of 3.5 minutes permits precise measurement on relatively small sample masses. While Brennecka et al. (2017) reported high efficiency using hydride generation to measure Te isotope ratios of calcium-aluminum-rich inclusions (~10 ng used per analysis), that method was designed to measure ^{126}Te anomalies in meteorites using internal normalization. The present study is the first to combine the double-spike technique with hydride generation to measure mass-dependent fractionation.

Surprisingly, our measurements on our instrument using desolvating nebulization (Aridus II system) yielded similar Te beam intensity at the same rate of Te mass consumed per unit time. This is an important result as hydride generation has been considered to produce superior sensitivity relative to the desolvating nebulizer for certain hydride forming elements like Sb and Se due to the efficiency of hydride formation and transfer into the mass spectrometer. The hydride sample introduction system used in this study produced equivalent sensitivity to that of Fehr et al. (2018) and Fukami et al. (2018). However, the Nu Plasma HR instrument used in this study was manufactured in 2004; newer MC-ICP-MS instruments would probably afford at least 2 times greater sensitivity.

There are significant advantages and disadvantages to each sample introduction system. As reported by Brennecka et al. (2017) at times we observed significant precipitation of elemental Te inside the hydride generation system. This caused slow wash-out of Te memory in the hydride generation system between samples and a decrease in sensitivity. Keeping the sample concentration below 5 ng mL^{-1} Te and tuning the instrument using a 0.5 ng mL^{-1} Te solution helped limit memory effects. We also avoided continuous measurement longer than 4 minutes and rinsed immediately after each analysis with a 0.5 M HCl wash followed by three 2 M HCl washes. In addition, while the Sn contribution from the $NaBH_4$ is significant for hydride generation (^{118}Sn ~30 to 100 mV), it will be corrected by on-peak zeroes and by monitoring ^{118}Sn.

A positive aspect of hydride generation is the avoidance of certain interferences that do not form hydrides. For example, barium (Ba) is an isobaric interference on ^{130}Te (0.11%) and ^{132}Xe (0.10%), which was monitored to correct for Xe on ^{126}Te, ^{128}Te, and ^{130}Te. This is a complex interference to correct for, due to the simultaneous impacts on ^{130}Te and the Xe correction. Ba would need to be reduced to very low levels by ion exchange chromatography or corrected for by monitoring ^{135}Ba, which is not feasible in our current detector setup. Furthermore, if solutions contain a simple matrix and low Sn (e.g. experimental samples), Te isotope measurements can be made by hydride generation with minimal preparation. This is in contrast to the DSN, where all analytes are transported into the mass spectrometer and could cause matrix or isobaric interferences.

In addition, the H_2 passed to the plasma by the hydride generation system suppresses the intensity of Xe and the Ar trimer, an impurity in Ar gas, thus decreasing the impact of these interferences. Furthermore, hydride generation also decreases the impact of Sn in sample solutions, as most Sn is not delivered to the plasma: Optimal stannane (SnH_4) generation requires basic conditions very different from those used for H_2Te generation (Rahman et al., 2018).

The sensitivity of both sample introduction methods allows for determination of rocks with average crustal Te concentrations. Samples containing more than 15 ng g^{-1} Te can be analyzed using the purification methods in this study. This range is relevant to natural sediments with lower Te content, such as CLG-1 and CLRD-3.0, and mafic rocks (Schirmer et al., 2014; Yierpan et al., 2018). For Te concentrations less than 15 ng g^{-1}, where more than 0.5 g of sample is required, $\delta^{130}Te/^{126}Te$ can be measured using separations of a single spiked sample split among parallel columns to distribute the matrix load. There will be a higher blank in the recombined sample. However, it will be considerably less than twice our current procedural blank, as the contribution of the blank is only from a few additional sources (column, column frit, and resin). This procedure may be suitable for average crustal rocks with lower Te contents, such as granites (Schirmer et al., 2014).

2.3.2 Precision and secondary standards

Long-term $\delta^{130}Te/^{126}Te$ reproducibility was assessed as twice the standard deviation (2σ) of repeated analyses over 2 years. Precision for NIST SRM 3156 processed through the sample preparation steps was ±0.06‰ (2σ) and 0.10‰ (2σ) for 100 ng (n = 11) and 50 ng (n=5) aliquots, respectively. For repeat analyses of a single bottle of the dissolved Alfa Aesar Te(VI) powdered standard (n= 39) our uncertainty was ±0.09‰ (2σ) for $\delta^{130}Te/^{126}Te$ (Table 2.2). The average $\delta^{130}Te/^{126}Te$ of the bracketing standard, NIST SRM 3156, was on average 0.04 ± 0.09‰ (2σ) (n=71). Average internal precision for $\delta^{130}Te/^{126}Te$, $\delta^{128}Te/^{126}Te$, and $\delta^{125}Te/^{126}Te$ was 0.07‰, 0.05‰ and 0.05‰ (2σ), respectively.

The long-term average $\delta^{130}Te/^{126}Te$ of the Te(VI) reagent used as an in-house standard was 0.84 ± 0.09‰ (2σ) relative to NIST SRM 3156. The Te(IV) Alfa Aesar reagent used as a second in-house standard was isotopically identical to NIST SRM 3156 within uncertainty. The offsets between these standards and NIST SRM 3156 were useful as secondary checks on analysis quality.

Repeat analyses of the Alfa Aesar Te(VI) solution were made at varying intensities to examine the impact on precision. When ^{130}Te intensity was less than 0.8 V, δ^{130}Te/^{126}Te and δ^{128}Te/^{126}Te values were measured outside of the accepted range of uncertainty and doubled for every factor of two decrease in intensity (Figure 2.1). This is equivalent to ~1.25 ng mL^{-1} Te for average instrument conditions. The increase in measured δ^{130}Te/^{126}Te, δ^{128}Te/^{126}Te, and δ^{125}Te/^{126}Te variability at lower Te intensities is due to an increasing impact of background interferences, such as ^{120}Sn and ^{124}Sn, and counting statistics-related noise on the measurement.

Overall, replicate measurements of natural samples (Table 2.3) show similar precision to that of the standards, implying good reproducibility of the digestion and ion exchange purification procedures. Higher variability in repeated measurements of Nod-P-1 (2σ: 0.12‰) and MAG-1 (2σ: 0.15‰) may reflect some heterogeneity within the powdered samples, as has been suggested by Fukami et al. (2018) for their analyses of ferromanganese nodules. For samples yielding less than 8 ng of Te or ^{130}Te less than 1.2 V, δ^{130}Te/^{126}Te, δ^{128}Te/^{126}Te, and δ^{125}Te/^{126}Te could be obtained with the trade-off of less precise measurements (Figure 2.1).

Our δ^{130}Te/^{126}Te measurement uncertainty (Table 2.2) is somewhat greater than the reported uncertainties of the most precise previously published methods (Fehr et al., 2018; Fukami et al., 2018); this difference arises from the current amplifier configuration of our instrument. A careful baseline analysis revealed no contributions from interferences other than ^{130}Xe, and because our Xe correction is both small and effective (see below), the added uncertainty cannot be attributed to interferences. Rather, some of our reported uncertainty arises from our use of a 10^{10} Ω resistor in the pre-amplifier for the collector used to measure ^{130}Te. Baseline (Johnson-Nyquist) noise measurements were 4 times higher on this collector than the others, which have 10^{11} Ω resistors. The resulting increase in uncertainty can be determined by calculating baseline noise on this channel (taking into account the total time of integration), multiplying by ¾ (¾ of the noise is excess noise cause by the use of the 10^{10} Ω resistor), and propagating this error through the isotope ratio measurement and double spike calculations. When the effect of the excess noise is removed, reproducibility of the standards and natural materials is about equal to that reported in Fehr et al., (2018). Accordingly, this method is expected to afford ±0.06‰ precision (2σ) on δ^{130}Te/^{126}Te for instruments with standard 10^{11} Ω resistors.

2.3.3 ^{120}Te-^{124}Te Double Spike

A spike to sample molar ratio of 0.98 was determined to be optimal for the inversion isotopes ^{130}Te, ^{126}Te, ^{124}Te, and ^{120}Te. This was based on repeated measurements of standards spiked with different proportions of spike, to minimize uncertainties in the final δ^{130}Te/^{126}Te associated with the spike composition. At this spike to sample composition, the precision observed is similar to the model generated by the Double Spike Toolbox (Rudge et al., 2009) (Figure 2.2). The accuracy of the spike composition was assessed by repeated measurements of lower (DS/natural ~ 0.60) and higher (DS/natural ~ 2) spiked samples (Figure 2.2). No statistically significant offsets were observed for δ^{130}Te/^{126}Te, δ^{128}Te/^{126}Te, and δ^{125}Te/^{126}Te (Table 2.2). The reproducibility of the lower- and higher-spiked standards were ±0.08‰ and ±0.09‰, respectively, similar to the precision of the normally spiked sample (Table 2.2). The optimal molar spike to sample ratio is noticeably higher than that recommended by the Double Spike Toolbox (DS/natural~ 0.62) (Rudge et al., 2009). However, the Double Spike Toolbox does not take into account effects of interferences. We find that increasing the spike to sample ratio lessens the influence of ^{120}Sn- and ^{124}Sn-related on the two spike isotopes leading to smaller errors on δ^{130}Te/^{126}Te, δ^{128}Te/^{126}Te, and δ^{125}Te/^{126}Te and overall better precision.

2.3.4 Effectiveness of Te purification methods, and blank results

Given the low abundance of Te compared to Sn (an isobaric interference) and Fe (a suppressant of hydride formation) in many terrestrial samples, separation from these interferences is challenging, yet important. To demonstrate effective Te separation from Sn- and Fe-rich samples, we present elution curves of a Nod-P-1 digestion (Figure 2.3) focusing on potential hydride-forming interferences and Fe. Arsenic, Se, and Fe are known suppressants of Te hydride formation at moderate concentrations, while Sn and Sb are isobaric interferences (Dedina, 1995). Yields for Te in Nod-P-1 (0.05 g digested) were high, and we achieve effective separation of Te from interfering matrix elements (Table 2.1). Elution with 8 mL of 1 M HNO_3 resulted in full recovery of Te (101.6%) similar to the results of the "HCl method" in Fehr et al. (2004) and Wang and Becker (2014) using a 3 mL AG1-X8 anion exchange column. The 5 M HF step eluted 69% of the total Fe while ~30% of the Fe was retained on the column (Figure 2.3A). Approximately 563 ng (<0.1%) of Fe were eluted with the Te fraction (1 M HNO_3). Selenium and other sample matrix elements were removed during the sample-loading step and the rinse with 6 M HCl. Antimony was mostly (>91%) retained on the column, presumably as $SbCl_6^-$, which adsorbs strongly in acidic conditions on basic resin (Korkisch, 2017). In the 1 M HNO_3 elution, 124 ng of Sb was eluted (2.5% of the Sb in the digested sample) as $SbCl_6^-$. Approximately 25% of Sn was eluted during the 5 M HF and 2 M HCl steps. Arsenic was also strongly retained in the column, with the exception of the 6 M HCl rinse. In 6 M HCl, most Sn loaded onto the anion-exchange resin is dissolved as $SnCl_5^-$ or $SnCl_4$ (Korkisch, 2017) and was retained during this rinse. In 2 M HCl, Sn(IV) elutes more readily as a neutrally charged species. In 5 M HF, Sn(IV) is moderately adsorbed, which accounts for the partial elution of Sn during this step. The rest was eluted with Te and was separated later (see below).

In the second ion exchange step (cation resin) modified after Wang et al. (2017), the first three milliliters of collected fluid contained all recoverable Te (Figure 2.3B). Sn(IV) hydrolyzes in low molarity acids to form weakly positive ions (Clayton et al., 2002). Dissolved Sn(IV) in low HCl molarity adsorbed on the acidic resin and, as expected, was not eluted in the collected Te fraction (Korkisch, 2017). The residual Fe that was not removed by the anion exchange step was adsorbed on the resin and not eluted with the Te fraction. Sb(V) was eluted with the collected Te fraction. For samples with relatively high Sn/Te (> 38), Sn was not completely separated. The reason behind this is unclear, but may be due to small amounts of dissolved $SnCl_5^-$ or $SnCl_6$ remaining in the sample. Passing the 0.1 M HCl sample solution through a column with 1 mL AG1-X8 (100-200 mesh) resin removed the remaining Sn (Wang et al., 2017). Dissolved Sn(IV) was only eluted at higher molarities of HCl (Wang et al., 2017).

Digestion blanks (n=3) were less than 0.01 ng on average. Cumulative blanks for the first two columns were 0.05 ng Te on average (n = 17) and for the third were 0.03 ng Te (n=4). Total cumulative blanks from all three columns are 0.5% of the lowest samples measured using this method. NIST SRM 3156 standards containing 100, 50, 15 ng Te processed through the columns showed no offset relative to unprocessed solutions, indicating that isotopic fractionation either did not occur during the process or was corrected for by the double spike (Table 2.2).

2.3.5 Interferences

Correction for Sn-based interferences is essential, as ^{120}Sn (32.58%) and ^{124}Sn (5.79%) are isobaric interferences on both Te spike isotopes, as we observed 30 to 100 mV of ^{118}Sn in the blank during hydride generation measurements. This contribution of Sn is mostly subtracted during on-peak zeros even when the $NaHB_4$ contains relatively high Sn (^{118}Sn > 80 mV). However, on-peak zero subtraction cannot correct for errors arising from incomplete removal of

Sn from samples during sample preparation. Doping experiments show that measuring ^{118}Sn (24.22%) and subtracting calculated ^{120}Sn and ^{124}Sn results in an effective correction up to ^{120}Sn/^{120}Te~0.02, equivalent to a 19‰ correction on δ^{130}Te/^{126}Te (Figure 2.4). This is a high tolerance for Sn, equal to 5 ng mL^{-1} Sn in a 2.5 ng mL^{-1} Te sample with normal spike to sample ratio. An example of high Sn/Te in a natural sample is the standard reference material MAG-1 (Sn/Te~ 54.5). For a required mass of 10 ng Te, approximately 99% of Sn would need to be separated from the purified Te to meet the Sn correction threshold for our initial correction. Given the efficacy of the column procedure in removing Sn, this requirement is not difficult to achieve. Standards did not exceed a ^{118}Sn intensity of 10 mV and did not require column purification.

Above ^{120}Sn/^{120}Te~0.02, we noted that increased Sn doping caused δ^{130}Te/^{126}Te to decrease linearly (Figure 2.4). This error is most likely caused by fractionation of Sn isotopes in the hydride generation system, which we expect is strong as Sn(IV) undergoes reduction by $NaBH_4$ and is incompletely released. Accordingly, our correction scheme, which assumes Sn of "average natural" composition and the same mass bias as Te, becomes inaccurate. We do not include a correction for SnH^+ signals, and thus contribution of $^{117}SnH^+$ to ^{118}Sn or $^{119}SnH^+$ to ^{120}Te may be another source of small errors at higher Sn/Te where the primary correction fails. Based on our Sn doping experiments, we suggest a secondary linear correction may be helpful up to ^{120}Sn/^{120}Te~0.3, the range of ^{120}Sn/^{120}Te we examined (Figure 2.4). We also note that the impact of Sn interferences can be reduced if the molarity of HCl in all samples is within ± 0.1 M of the 4 M HCl acid used for the blank. Discrepancies in HCl molarity in the blank and sample can lead to post-correction excesses in the net Sn signal as the production of stannane during hydride generation is favorable at more basic conditions (Rahman et al., 2018). Therefore, the HCl molarity of a small aliquot of each sample was checked via titration.

Residual Xe after subtraction of on-peak zeros was corrected successfully using ^{132}Xe measurements. As an impurity in the Ar gas, ^{132}Xe typically varies between 5-15 mV before the correction from one session to another and is stable over the measurement run. While Xe isotopes impact ^{130}Te (^{130}Xe: 4.071%), ^{128}Te (^{128}Xe: 1.910%), ^{126}Te (^{126}Xe: 0.089%), and ^{124}Te (^{124}Xe: 0.095%), this correction is at most ± 0.1‰ on δ^{130}Te/^{126}Te and is even lower on the other impacted Te isotope ratios. On average, residual ^{130}Xe is 10^{-4} V, as most of the Xe was corrected in the on-peak zero subtraction. As such, it is not a challenging interference to correct for, but could be if Xe concentrations were larger or fluctuated significantly during analyses. For example, high impurities in Ar, as a result of the fractional distillation of air, could possibly cause problematic intensities of isotopically fractionated Xe.

The impact of Te hydrides (^{124}Te^{1}H, ^{125}Te^{1}H) was also minimized due to our corrections. Based on measurements of mass 131 while measuring a Te standard solution, we estimate the TeH^{+}/Te ~ 10^{-4}. This magnitude of hydride formation is similar to that of SeH^{+}/Se in the hydride generation system used here. This value is refined before every run and does not vary by more than ± 3 x10^{-5} between measurement sessions. It is imperative that the double spike is well characterized before this correction is applied, as the TeH^{+}/Te is tuned using the results of overspiked or underspiked standards at the beginning of each analytical session (see methods section).

While Sb does not directly cause an interference on any isotopes of interest, ^{123}Sb^{1}H could potentially affect ^{124}Te. Figure 2.5 indicates that this is not consequential at even relatively high Sb added into the standard. Assuming a similar hydride formation rate as TeH^{+}/Te of 10^{-4}, a

^{123}Sb/^{130}Te ratio of 1.24 would cause a 0.12‰ shift on δ^{130}Te/^{126}Te. This is not apparent in the measurement results given in Figure 2.5, indicating Sb must have lower rates of hydride formation than noted here for TeH$^+$/Te. In addition, H_3Sb generation is inefficient when Sb is present in the oxidized Sb(V) form (Dedina, 1995), as expected for samples stored in contact with air. As a result, Sb/Te for natural samples measured to date has always been less than that of the maximum Sb doped standard in Figure 2.5. A ^{123}XH$^+$/^{124}Te correction of 0.00001, nevertheless, is included in our routine in the event of higher Sb intensities.

2.3.6 Concentration measurements

Concentrations of Nod-P-1, SCO-1, MAG-1, and SGR-1 calculated by isotope dilution overall agree with previously published data (Table 2.3) (Axelsson et al., 2002; Fehr et al., 2018; Fukami et al., 2018; Schirmer et al., 2014; Wang and Becker, 2014). The average of multiple digestions of Nod-P-1 is identical to all three previous reported results, within the uncertainties. SCO-1 and MAG-1 agree within uncertainty with concentration values in Wang and Becker (2014). Variability over multiple measurements could be the result of heterogeneity in the powdered material or contribution of error from weighing errors inherent in measuring small sample masses (e.g., 0.02 g) using the balance available in our laboratory. Our isotope dilution results for USGS soils and mine tailings provide more precise concentration measurements than previous measurements by single-collector ICP-MS digestions. While there are no previously published concentrations of CLRD-3.0 and CLG-1, good reproducibility indicates nearly full recovery of samples.

2.3.7 Isotope measurements of natural samples

The NIST SRM 3156 standard solution used to define the zero point on the delta scale originates from the same batch (Lot: 140830) measured in Fukami et al. (2018), Therefore, we can compare directly our results to values of Nod-P-1 reported in this study. The NIST SRM 3156 measured by Fehr et al. (2018) is sourced from a different lot, which, in this case, originates from separate materials and manufacturers and cannot be directly compared. Nevertheless, a few of our values match well with those published in Fehr et al. (2018) and could be indicative of similar isotopic compositions between lots. Our average Nod-P-1 agrees with those of both Fehr et al. (2018) and Fukami et al. (2018) highlighting the relative uniformity in this specific powdered material despite possible chemical heterogeneity in the original nodules and in other samples (see below). The average of MAG-1 measured in our study overlaps within analytical uncertainty to values in Fehr et al. (2018). However, our average δ^{130}Te/^{125}Te for SGR-1 is significantly greater than the single measurement reported for the same reference material in Fehr et al. (2018). This may be due to either differences in the δ^{130}Te/^{125}Te NIST SRM 3156 or heterogeneity in the sample bottle. Variability in selenium isotope ratios has been noted before between different bottles of SGR-1, suggesting that this material may be isotopically heterogeneous (Mitchell et al., 2016).

All samples measured were isotopically heavier than NIST SRM 3156; the heaviest and lightest being the Vulcan Yellow Precipitate (1.29 ± 0.08 ‰) and C350500 (0.08 ± 0.06 ‰), respectively. This is the largest range in δ^{130}Te/^{126}Te, δ^{128}Te/^{126}Te, and δ^{125}Te/^{126}Te observed in low-temperature environments yet, suggesting that Te stable isotopes fractionate during low-temperature processes in marine and terrestrial weathering environments. Redox reactions may contribute to the observed isotopic fractionation. For example, Fukami et al. (2018) suggested that oxidation of Te(IV) to Te(VI) in ferromanganese crust may result in isotopically heavy values. Reduction of Te oxyanions to elemental Te(0) in reducing soils may also drive the residual Te isotopically heavier as well, as has been shown for various abiotic reductants

(Baesman et al., 2007). Alternatively, the major fractionating pathway could be adsorption, as both Te(VI) and Te(IV) adsorb strongly on iron oxides (Qin et al., 2017). As observed for W adsorption on ferrihydrite, adsorption of metal oxyanions results in an isotopically lighter sorbent relative to the original fluid due to differences in the coordination environment (Kashiwabara et al., 2017). As the magnitude of adsorption increases, the solid sample could evolve to a heavier Te isotopic composition. This is another interpretation for the correlation between the higher Te/Se ratio and δ^{130}Te/^{125}Te as noted in Fukami et al. (2018). It also may explain why certain samples, that have undergone a greater extent of oxidation or contain greater Fe_2O_3%, like the Vulcan Yellow precipitate, seem to be isotopically heavier than less Fe_2O_3% rich samples. For example Nod-P-1 is 0.35‰ heavier than the marine mud, MAG-1 and topsoil, C320293, is 0.25‰ greater than the Horizon A soil, C350500.

Te isotope studies have not yet found evidence of mass-independent fractionation of Te isotopes in terrestrial samples (Fehr et al., 2018; Fehr et al., 2005; Fornadel et al., 2017), despite significant nuclear field shift effects on Te isotopes observed in a laboratory study (Moynier et al., 2008). When comparing δ^{128}Te/^{126}Te and δ^{125}Te/^{126}Te to δ^{130}Te/^{126}Te, we observe no significant deviations from mass-dependent fractionation in the Alfa Aesar Te(VI) powder standards (Figure 2.6). We also see no deviation within analytical uncertainty from an exponential mass-dependent fractionation relationship in the natural samples either (Figure 2.6). With additional replicate analyses leading to higher precision, mass-independent fractionation may be resolved. Assuming an exponential mass-dependent kinetic isotope fractionation law, the slope (β) of the relationships in Figure 2.6 is expressed as:

$$\beta = \frac{ln\frac{m_{126}}{m_x}}{ln\frac{m_{126}}{m_{130}}},$$

where X is either the mass of ^{128}Te or ^{125}Te. This observation does not preclude the possibility of mass-independent fractionation in the future though. The fact that mass-dependent patterns were always observed provide further evidence of the fidelity of the measurements despite several interferences. In particular, the Sn correction is effective over a large range of Sn/Te in the samples. Improper removal of Sn to produce a large Sn excess would not only artificially depress the δ^{130}Te/^{126}Te and δ^{128}Te/^{126}Te, and increase δ^{125}Te/^{126}Te, but also affect mass-independent fractionation due to the ^{124}TeH^{+} correction on ^{125}Te.

2.4 Conclusions

The methods detailed in this study provide a new approach to measure Te isotopes.

- While we expected that the hydride generation method would allow for measurements on lower masses of Te with better ionization efficiency, under the current conditions on our instrument, we observe that the sensitivity of the hydride generation sample introduction is similar to that achieved with a desolvating nebulizer (Aridus II; <8.75 ng Te per measurement).
- Hydride generation avoids the introduction of certain interfering elements like Ba, which can be complicated to correct for. Furthermore, many solutions containing low dissolved Sn and Fe concentrations can be analyzed without any matrix separation. This enables a large savings in time for some sample types with simple matrices, such as those generated by laboratory experiments and possibly high-Te contaminated water.
- The attainable precision of this method using about 8 ng per measurement ($2\sigma \sim 0.09‰$ for δ^{130}Te/^{126}Te) is similar to that of previously published methods.

- The large range in $\delta^{130}Te/^{126}Te$ (1.21‰) of several natural samples presented here indicates that isotopic fractionation of Te is prevalent in low-temperature marine and terrestrial environments.
- Despite the potential for effects from interferences like Sb, Sn and Fe, the ion exchange procedure we modified from previous methods effectively purifies Te from the sample matrix. Future studies can apply this method to Te isotope measurements of natural waters.
- We observed that the $\delta^{130}Te/^{126}Te$, $\delta^{128}Te/^{126}Te$, and $\delta^{125}Te/^{126}Te$ results for reagent Te and the natural samples follow mass-dependent fractionation as has been observed in all studies to date.

Although laboratories using desolvating nebulization should be able to achieve high-quality measurements with similar masses of Te, we suggest that future laboratory and field studies can use this hydride generation approach advantageously due to its ability decrease or eliminate interferences and matrix-related problems.

2.5 Tables and Figures

Table 2.1. Detector setup showing associated Te isotopes and isobaric interferences.

L4	L3	L1	Ax	H1	H2	H3	H4	H5	H6
^{118}Sn	**^{120}Te** ^{120}Sn ^{119}SnH^{+} ^{40}Ar^{40}Ar^{40}Ar	**^{123}Te** ^{123}Sb ^{122}TeH^{+}	**^{124}Te** ^{124}Sn ^{123}SbH^{+} ^{123}TeH^{+} ^{124}Xe	**^{125}Te** ^{125}TeH^{+}	**^{126}Te** ^{126}Xe ^{126}TeH^{+}	^{127}I	**^{128}Te** ^{128}Xe	**^{130}Te** ^{130}Xe ^{130}Ba	^{132}Xe ^{132}Ba

Table 2.2. δ^{130}Te$^{/126}$Te data of standards.

Standard	Number of Analyses	δ^{130}Te/^{126}Te (‰)	2σ
In-house standard solution from Alfa Aesar Te(VI) powder (lot no. Y05A029)	39	0.84	0.09
In-house standard solution from Alfa Aesar Te(IV) powder (lot no. M27C052)	13	-0.06	0.14
Processed NIST SRM 3156 (100 ng)[a]	11	0.00	0.06
Processed NIST SRM 3156 (50 ng)[a]	5	0.04	0.10
Processed NIST SRM 3156 (15 ng)	1	-0.06	n.d.
Processed NIST SRM 3156 (15 ng)	1	0.00	n.d
NIST SRM 3156 (DS/sample ~0.6)	7	0.00	0.08
NIST SRM 3156 (DS/sample ~ 2)	5	-0.05	0.09
NIST SRM 3156 bracketing standards	71	0.04	0.09

[a.] Processed NIST SRM 3156 standards represent an aliquot of standard run through all three columns (Section 2.3).

Table 2.3. Results of Te concentrations and Te isotope ratios of natural samples.[a]

Sample	**Te [µg g^{-1}]**	**2σ**	**δ^{130}Te/^{126}Te (‰)**	**2σ**	**δ^{128}Te/^{126}Te (‰)**	**2σ**	**δ^{125}Te/^{126}Te (‰)**	**2σ**	**δ^{130}Te/^{125}Te (‰)**	**2σ**
Nod-P-1										
This study	4.7		0.5		0.2		-0.22		0.72	
This study	5.44		0.44		0.25		-0.12		0.66	
This study	4.59		0.59		0.33		-0.09		0.68	
This study	4.58		0.51		0.22		-0.07		0.59	
This study	5.08		0.45		0.27		-0.07		0.52	
Average	**4.88**	**0.75**	**0.5**	**0.12**	**0.25**	**0.1**	**-0.11**	**0.12**	**0.64**	**0.16**
Fehr et al. (2018)	n.d.								0.54	0.12
Fukami et al. (2018)	5.14	0.31							0.66	0.05
Axelsson et al.(2002)	4.8	0.4								
Schirmer et al. (2014)	4.95	0.4								
SCO-1										
This study	0.08		0.12		0.06		0.02		0.09	
This study	0.08		0.13		0.04		0.01		0.12	
Average	**0.08**	**0**	**0.13**	**0.02**	**0.05**	**0.03**	**0.01**	**0.01**	**0.1**	**0.03**
Wang et al. (2014)	0.07	0.02								
Schirmer et al. (2014)	0.09	0.01								

Table 2.3 (cont.)

Sample	**Te [μg g^{-1}]**	**2σ**	**δ^{130}Te/^{126}Te (‰)**	**2σ**	**δ^{128}Te/^{126}Te (‰)**	**2σ**	**δ^{125}Te/^{126}Te (‰)**	**2σ**	**δ^{130}Te/^{125}Te (‰)**	**2σ**
SGR-1										
This study	0.25		0.32		0.29		-0.13		0.46	
This study	0.25		0.29		0.17		-0.01		0.3	
Average	**0.25**	**0**	**0.31**	**0.04**	**0.23**	**0.18**	**-0.07**	**0.16**	**0.31**	**0.23**
Schirmer et al. (2014)	0.24	0.01								
Fehr et al. (2018)	0.2	n.d.							0.04	0.08
MAG-1										
This study	0.07		0.15		0.08		-0.04		0.2	
This study	0.06		0.17		0.24		-0.18		0.33	
This study	0.07		0.05		0.12		-0.09		0.29	
This study	0.06		0.23		0.28		-0.16		0.45	
Average	**0.07**	**0.01**	**0.15**	**0.15**	**0.18**	**0.19**	**-0.12**	**0.13**	**0.32**	**0.21**
Wang et al. (2014)	0.07	0.01								
Fehr et al. (2018)	0.05	n.d.							0.01	0.1
C320293										
This study	69.94		0.35		0.16		-0.09		0.47	
This study	49.74		0.42		0.14		-0.02		0.46	
This study	56.72		0.33		0.15		-0.07		0.5	
This study	54.69		0.32		0.14		-0.08		0.39	
Average	**57.77**	**17.25**	**0.36**	**0.09**	**0.15**	**0.02**	**-0.07**	**0.06**	**0.46**	**0.09**
USGS	50.5	n.d.								

Table 2.3 (cont.)

Sample	**Te [µg g^{-1}]**	**2σ**	**δ^{130}Te/^{126}Te (‰)**	**2σ**	**δ^{128}Te/^{126}Te (‰)**	**2σ**	**δ^{125}Te/^{126}Te (‰)**	**2σ**	**δ^{130}Te/^{125}Te (‰)**	**2σ**
C350500										
This study	18.34		0.06		0		-0.1		0.2	
This study	17.92		0.11		-0.04		-0.07		0.25	
Average	**18.13**	**0.59**	**0.08**	**0.06**	**-0.02**	**0.05**	**-0.08**	**0.05**	**0.23**	**0.07**
USGS	9.6	n.d.								
Masonic surface										
This study	1070.89		0.31		0.09		-0.16		0.49	
This study	1810.83		0.39		0.18		-0.1		0.52	
Average	**1440.86**	**1046.43**	**0.35**	**0.11**	**0.13**	**0.12**	**-0.13**	**0.09**	**0.51**	**0.04**
Vulcan yellow precipitate										
This study	571.75		1.33		0.75		-0.36		1.64	
This study	684.71		1.24		0.66		-0.39		1.5	
This study	604.63		1.28		0.75		-0.3		1.57	
This study	627.46		1.31		0.68		-0.23		1.55	
Average	**622.14**	**95.14**	**1.29**	**0.08**	**0.71**	**0.09**	**-0.32**	**0.14**	**1.57**	**0.12**
Ute Ulay surface										
This study	19.92		0.47		0.21		-0.13		0.6	
This study	17.03		0.46		0.22		-0.12		0.48	
This study	18.03		0.54		0.33		-0.19		0.67	
This study	16.93		0.42		0.34		-0.06		0.52	
Average	**17.98**	**2.77**	**0.47**	**0.09**	**0.27**	**0.14**	**-0.13**	**0.11**	**0.57**	**0.17**

Table 2.3 (cont.)

Sample	**Te [µg g^{-1}]**	**2σ**	**δ^{130}Te/^{126}Te (‰)**	**2σ**	**δ^{128}Te/^{126}Te (‰)**	**2σ**	**δ^{125}Te/^{126}Te (‰)**	**2σ**	**δ^{130}Te/^{125}Te (‰)**	**2σ**
Ute Ulay deep										
This study	1.66		0.36		0.22		-0.13		0.47	
This study	1.04		0.4		0.24		-0.15		0.55	
This study	1.32		0.4		0.25		-0.12		0.52	
Average	**1.34**	**0.63**	**0.38**	**0.05**	**0.23**	**0.03**	**-0.13**	**0.03**	**0.51**	**0.08**
Delamar big tails surface										
This study	233.67		0.31		0.2		-0.02		0.35	
This study	337.01		0.41		0.2		-0.08		0.48	
This study	335.4		0.31		0.27		-0.1		0.41	
Average	**302.03**	**118.41**	**0.34**	**0.11**	**0.22**	**0.08**	**-0.07**	**0.08**	**0.41**	**0.14**
CLRD-3.0										
This study	0.037		0.32		0.09		-0.02		0.34	
This study	0.041		0.4		0.21		-0.13		0.53	
Average	**0.039**	**0.007**	**0.36**	**0.11**	**0.15**	**0.16**	**-0.08**	**0.16**	**0.44**	**0.27**
CLG-1										
This study	0.02		0.14		0.08		0		0.14	
This study	0.018		0.08		0.04		-0.11		0.19	
Average	**0.019**	**0.003**	**0.11**	**0.08**	**0.06**	**0.05**	**-0.05**	**0.15**	**0.17**	**0.07**

[a] All values reported for this study represent samples digested, purified, and measured once. *Fehr et al. (2018) and Fukami et al. (2018) values are compared to the average NIST SRM 3156 values reported in their respective studies. δ^{130}Te/^{125}Te results are calculated using ^{120}Te, ^{124}Te, ^{125}Te, and ^{130}Te as the inversion isotopes.

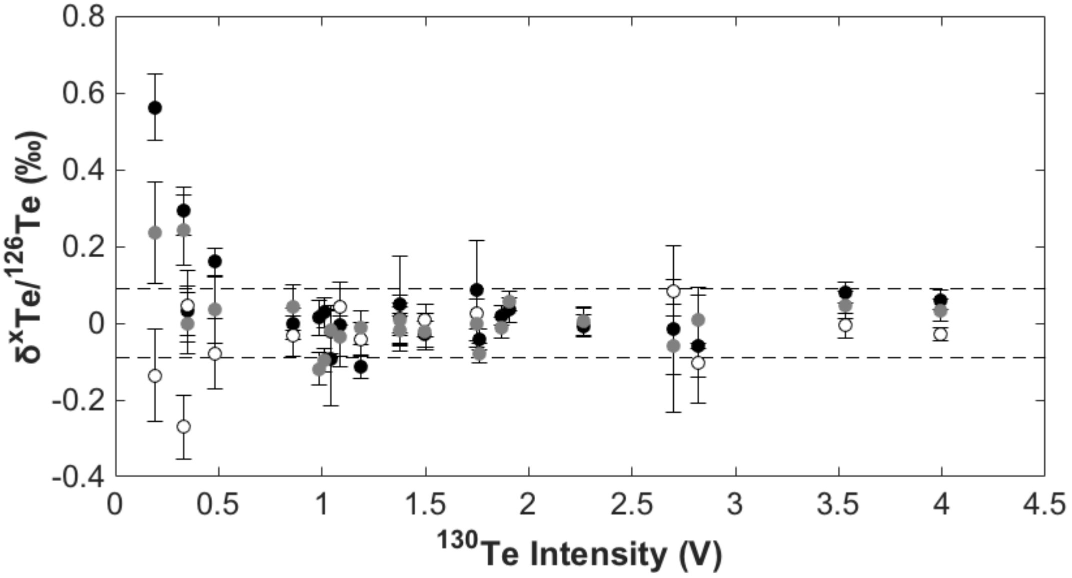

Figure 2.1. Repeated analyses of δ^{130}Te/^{126}Te (black circles), δ^{128}Te/^{126}Te (grey circles), or δ^{125}Te/^{126}Te (open circles) at varying intensities of the Alfa Aesar Te(VI) in-house standard with optimal spike:sample ratio normalized to the average value of a 2.5 ppb solution of Alfa Aesar Te(VI). The dashed band denotes the average envelope of uncertainty (2σ) for δ^{130}Te/^{126}Te. Error bars represent twice the standard error of an individual analysis.

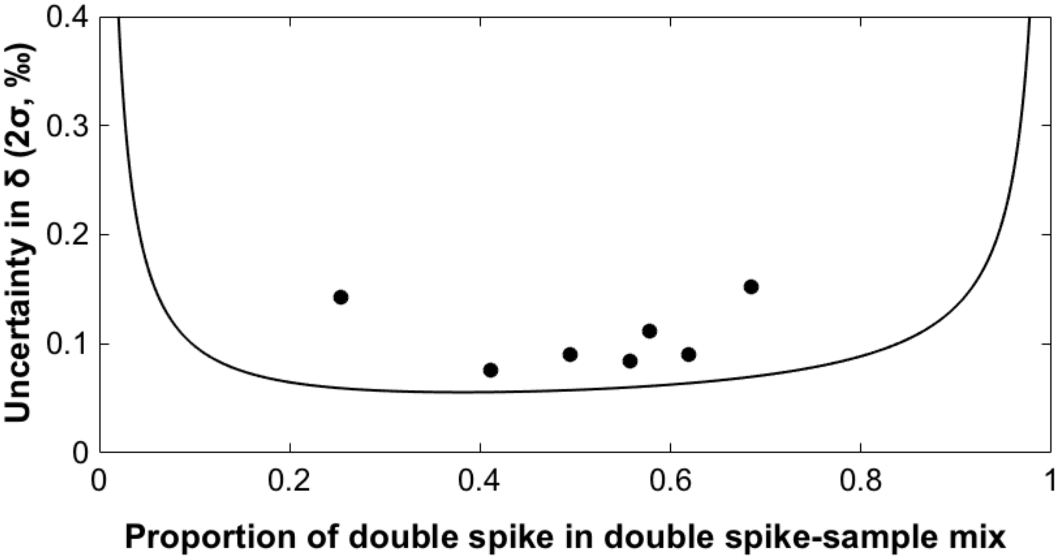

Figure 2.2. Uncertainties of $\delta^{130}Te/^{126}Te$ over various proportions of double spike in the double spike-sample mixture. Black circles represent triplicate measurements of NIST SRM 3156 at different proportion of double spike in the double spike-sample mixture (molar basis). The solid line denotes the error propagation model by Rudge et al. (2009) using the double spike composition from this study, where the optimal proportion of double spike in the double spike mixture is 0.28.

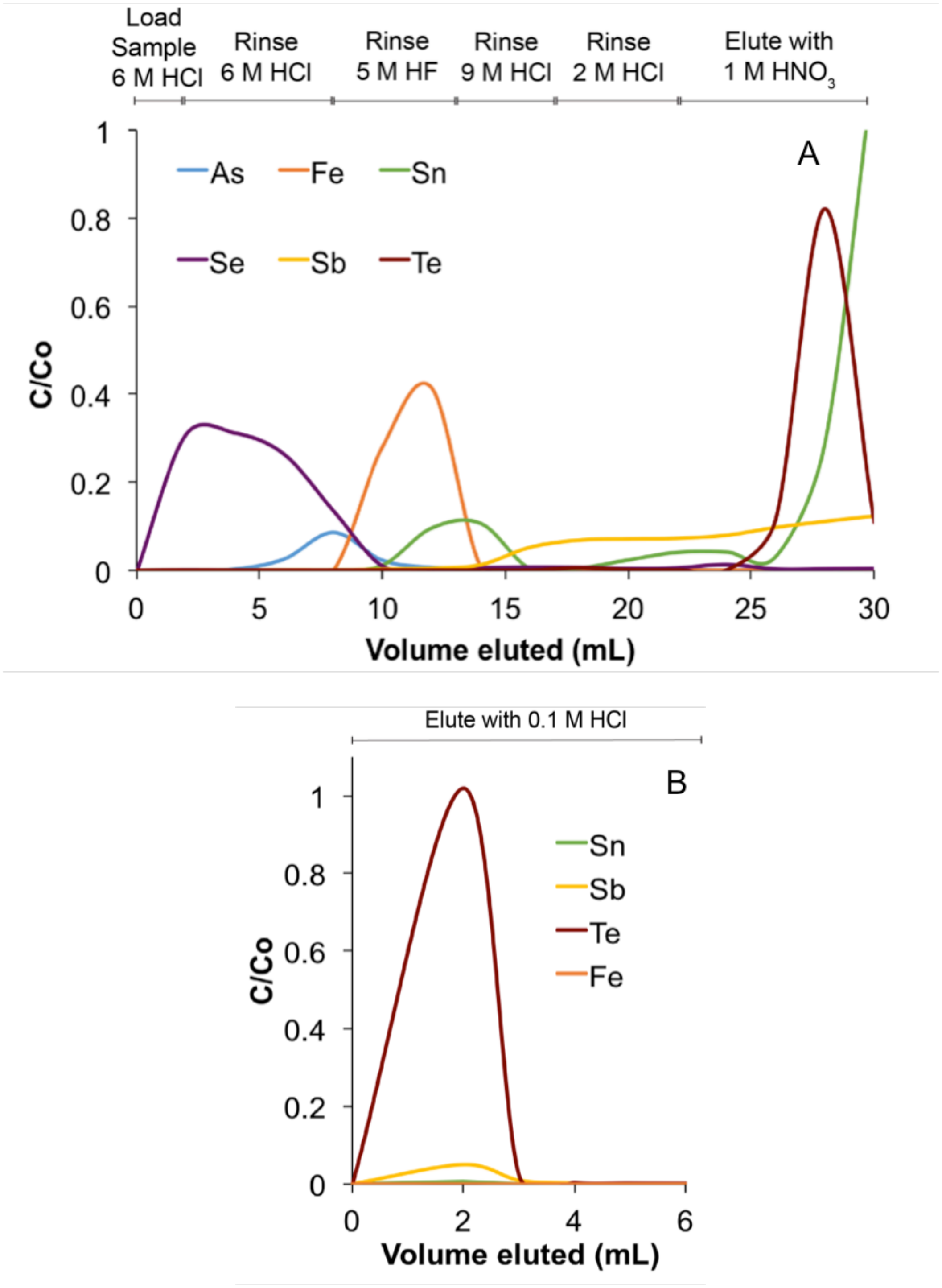

Figure 2.3. (A) Elution curves for a digestion of 50 mg of SRM Nod-P-1 following a modified anion exchange procedure from Fehr et al. (2004) and Wang and Becker (2014). (B) Elution curves for the secondary column to separate Sn and Fe from Te using AG 50W-X8 cation-exchange resin. C/Co is defined as the elemental mass eluted over the total elemental mass of sample loaded into the column.

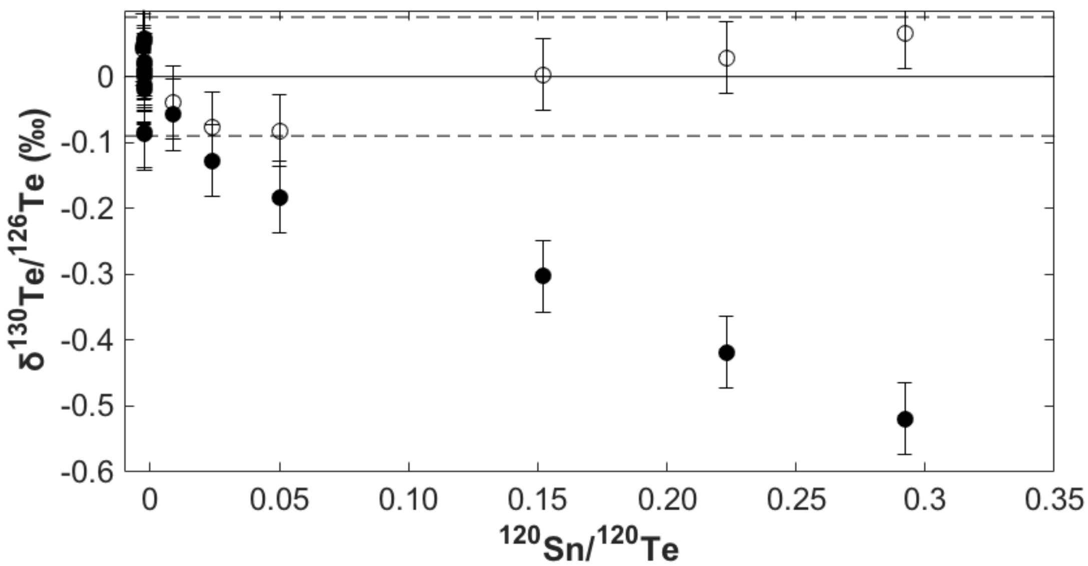

Figure 2.4. δ^{130}Te/^{126}Te with increasing amounts of Sn doped into the standard Alfa Aesar Te(VI) solution and normalized to the average Alfa Aesar Te(VI) value. Filled circles show measured values that are corrected with the primary correction. Open circles have a secondary correction based on a linear fit between δ^{130}Te/^{126}Te and Sn/Te. These corrected values fall within the average envelope of uncertainty (2σ) for repeated analyses of Alfa Aesar Te(VI) denoted by the dashed lines. Error bars are twice the average standard error of the measurements.

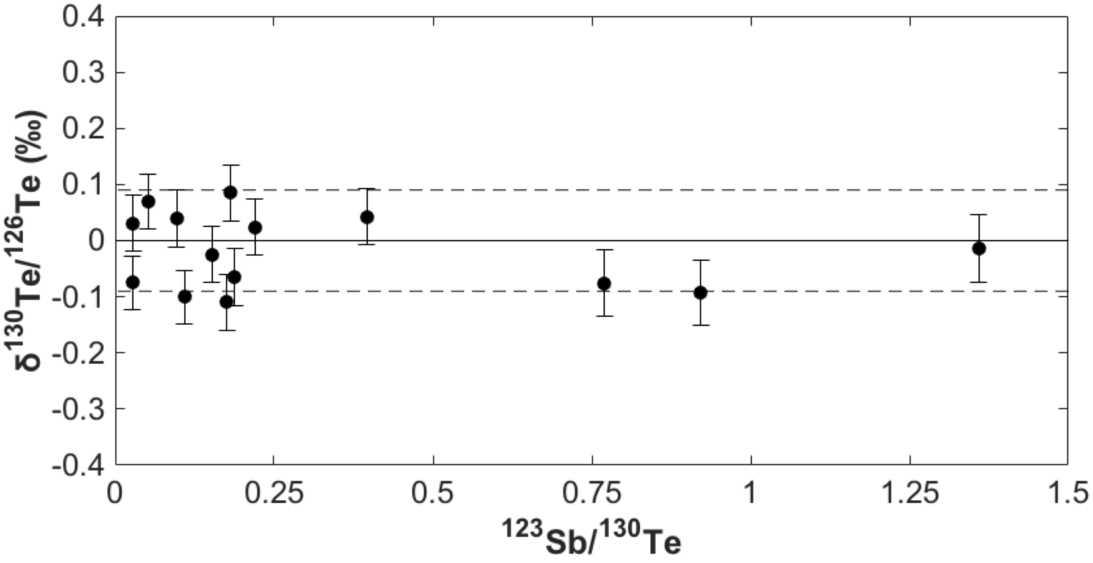

Figure 2.5. $\delta^{130}Te/^{126}Te$ with increasing amounts of Sb added to the standard NIST SRM 3156, as indicated by the ratio of ^{123}Sb to ^{130}Te on the x axis. No $^{123}SbH^{+}$ correction is applied to the data shown. The impact of $^{123}SbH^{+}$ on measurement of ^{124}Te is negligible for $^{123}Sb/^{130}Te < 1.4$. The dashed lines indicate the average envelope of uncertainty (2σ) for repeated analyses of NIST SRM 3156. Error bars are twice the standard error of each measurements.

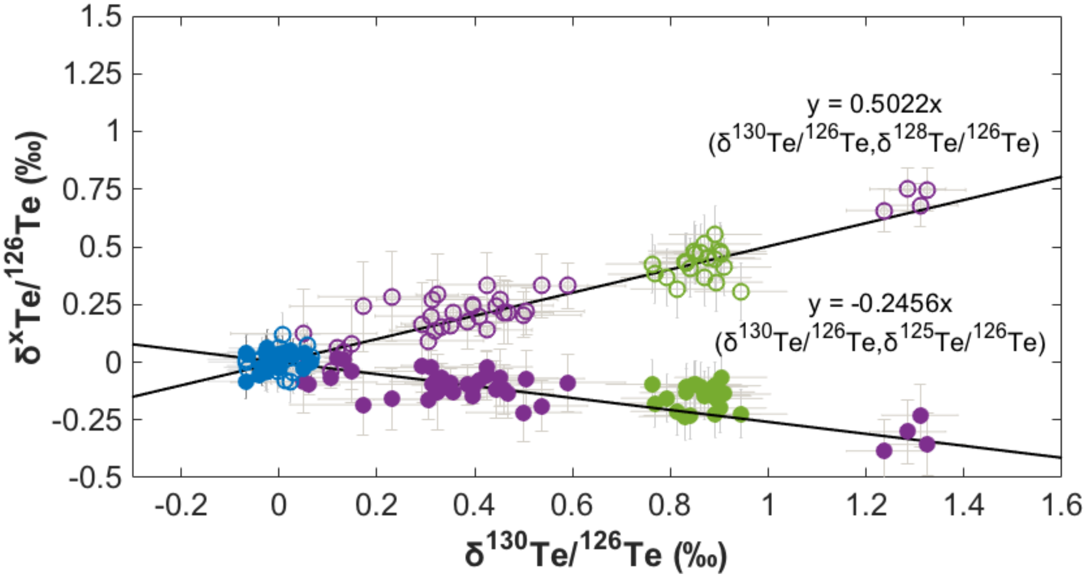

Figure 2.6. Comparison of δ^{128}Te/^{126}Te or δ^{125}Te/^{126}Te by δ^{130}Te/^{126}Te. Open symbols reflect the δ^{130}Te/^{126}Te, δ^{128}Te/^{126}Te correlation, while closed symbols show δ^{130}Te/^{126}Te, δ^{128}Te/^{126}Te. All symbols fall within analytical uncertainty (2σ, grey error bars) of the expected relationship (δ^{128}Te/^{126}Te = 0.5022 x δ^{130}Te/^{126}Te and δ^{125}Te/^{126}Te = -0.2456 x δ^{130}Te/^{126}Te), based on exponential-law, mass-dependent kinetic fractionation. Blue symbols are multiple analyses of NIST SRM 3156; purple symbols reflect natural samples; green symbols are multiple analyses of the Alfa Aesar Te(VI) reagent.

2.6 References

Axelsson, M.D., Rodushkin, I., Ingri, J. and Öhlander, B. (2002) Multielemental analysis of Mn–Fe nodules by ICP-MS: optimisation of analytical method. Analyst 127, 76-82.

Babechuk, M.G., Weimar, N.E., Kleinhanns, I.C., Eroglu, S., Swanner, E.D., Kenny, G.G., Kamber, B.S. and Schoenberg, R. (2019) Pervasively anoxic surface conditions at the onset of the Great Oxidation Event: New multi-proxy constraints from the Cooper Lake paleosol. Precambrian Research 323, 126-163.

Baesman, S.M., Bullen, T.D., Dewald, J., Zhang, D., Curran, S., Islam, F.S., Beveridge, T.J. and Oremland, R.S. (2007) Formation of Tellurium Nanocrystals during Anaerobic Growth of Bacteria That Use Te Oxyanions as Respiratory Electron Acceptors. Appl. Environ. Microbiol. 73, 2135-2143.

Belzile, N. and Chen, Y.-W. (2015) Tellurium in the environment: A critical review focused on natural waters, soils, sediments and airborne particles. Applied Geochemistry 63, 83-92.

Bopp, C.J., Lundstrom, C.C., Johnson, T.M., Sanford, R.A., Long, P.E. and Williams, K.H. (2010) Uranium 238U/235U Isotope Ratios as Indicators of Reduction: Results from an in situ Biostimulation Experiment at Rifle, Colorado, U.S.A. Environmental Science & Technology 44, 5927-5933.

Brennecka, G.A., Borg, L.E., Romaniello, S.J., Souders, A.K., Shollenberger, Q.R., Marks, N.E. and Wadhwa, M. (2017) A renewed search for short-lived 126Sn in the early Solar System: Hydride generation MC-ICPMS for high sensitivity Te isotopic analysis. Geochimica et Cosmochimica Acta 201, 331-344.

Chen, Y.-W., Alzahrani, A., Deng, T.-L. and Belzile, N. (2016) Valence properties of tellurium in different chemical systems and its determination in refractory environmental samples using hydride generation – Atomic fluorescence spectroscopy. Analytica Chimica Acta 905, 42-50.

Clayton, R., Andersson, P., Gale, N.H., Gillis, C. and Whitehouse, M.J. (2002) Precise determination of the isotopic composition of Sn using MC-ICP-MS. Journal of Analytical Atomic Spectrometry 17, 1248-1256.

Dedina, J.a.T.D.L. (1995) Hydride Generation Atomic Absorption Spectrometry. Wiley, Chichester, NY.

Ellis, A.S., Johnson, T.M., Herbel, M.J. and Bullen, T.D. (2003) Stable isotope fractionation of selenium by natural microbial consortia. Chemical Geology 195, 119-129.

Eugster, O., Tera, F. and Wasserburg, G.J. (1969) Isotopic analyses of barium in meteorites and in terrestrial samples. Journal of Geophysical Research (1896-1977) 74, 3897-3908.

Fehr, M.A., Hammond, S.J. and Parkinson, I.J. (2018) Tellurium stable isotope fractionation in chondritic meteorites and some terrestrial samples. Geochimica et Cosmochimica Acta 222, 17-33.

Fehr, M.A., Rehkämper, M. and Halliday, A.N. (2004) Application of MC-ICPMS to the precise determination of tellurium isotope compositions in chondrites, iron meteorites and sulfides. International Journal of Mass Spectrometry 232, 83-94.

Fehr, M.A., Rehkämper, M., Halliday, A.N., Wiechert, U., Hattendorf, B., Günther, D., Ono, S., Eigenbrode, J.L. and Rumble, D. (2005) Tellurium isotopic composition of the early solar system—A search for effects resulting from stellar nucleosynthesis, 126Sn decay, and mass-independent fractionation. Geochimica et Cosmochimica Acta 69, 5099-5112.

Flanagan, F.J. and Gottfried, D. (1980) USGS rock standards; III, Manganese-nodule reference samples USGS-Nod-A-1 and USGS-Nod-P-1, Professional Paper. U.S. Govt. Print Off.

Fornadel, A.P., Spry, P.G., Haghnegahdar, M.A., Schauble, E.A., Jackson, S.E. and Mills, S.J. (2017) Stable Te isotope fractionation in tellurium-bearing minerals from precious metal hydrothermal ore deposits. Geochimica et Cosmochimica Acta 202, 215-230.

Forrest, A., Kingsley, R. and Schilling, J.-G. (2009) Determination of Selenium and Tellurium in Basalt Rock Reference Materials by Isotope Dilution Hydride Generation-Inductively Coupled Plasma-Mass Spectrometry (ID-HG-ICP-MS). Geostandards and Geoanalytical Research 33, 261-269.

Fukami, Y., Kimura, J.-I. and Suzuki, K. (2018) Precise isotope analysis of tellurium by inductively coupled plasma mass spectrometry using a double spike method. Journal of Analytical Atomic Spectrometry 33, 1233-1242.

Gao L.Z., Z.C.H., Yin, C. Y., Shi X. Y., Wang Z.Q., Liu T. M. Liu P. J., Tang F. and Song B. (2008) SHRIMP zircon ages: basis for refining the chronostratigraphic classification of the Meso- and Neoproterozoic strate in North China Old Land. Acta Geoscience Sinica 29, 366-376.

Gerhardsson, L. (2015) Chapter 54 - Tellurium, in: Nordberg, G.F., Fowler, B.A., Nordberg, M. (Eds.), Handbook on the Toxicology of Metals (Fourth Edition). Academic Press, San Diego, pp. 1217-1228.

Goldfarb, R. (2015) Tellurium—The bright future of solar energy.

Hardisty, D.S., Lu, Z., Bekker, A., Diamond, C.W., Gill, B.C., Jiang, G., Kah, L.C., Knoll, A.H., Loyd, S.J., Osburn, M.R., Planavsky, N.J., Wang, C., Zhou, X. and Lyons, T.W. (2017) Perspectives on Proterozoic surface ocean redox from iodine contents in ancient and recent carbonate. Earth and Planetary Science Letters 463, 159-170.

Hayes, S.M. and Ramos, N.A. (2019) Surficial geochemistry and bioaccessibility of tellurium in semiarid mine tailings. Environmental Chemistry 16, 251-265.

Hein, J.R., Koschinsky, A. and Halliday, A.N. (2003) Global occurrence of tellurium-rich ferromanganese crusts and a model for the enrichment of tellurium. Geochimica et Cosmochimica Acta 67, 1117-1127.

Johnson, C.M. and Beard, B.L. (1999) Correction of instrumentally produced mass fractionation during isotopic analysis of fe by thermal ionization mass spectrometry. International Journal of Mass Spectrometry 193, 87-99.

Kashiwabara, T., Kubo, S., Tanaka, M., Senda, R., Iizuka, T., Tanimizu, M. and Takahashi, Y. (2017) Stable isotope fractionation of tungsten during adsorption on Fe and Mn (oxyhydr)oxides. Geochimica et Cosmochimica Acta 204, 52-67.

Korkisch, J. (2017) CRC Handbook of Ion Exchange Resins. Routledge.

Lee, D.S. and Edmond, J.M. (1985) Tellurium species in seawater. Nature 313, 782-785.

Li, C., Planavsky, N.J., Love, G.D., Reinhard, C.T., Hardisty, D., Feng, L., Bates, S.M., Huang, J., Zhang, Q., Chu, X. and Lyons, T.W. (2015) Marine redox conditions in the middle Proterozoic ocean and isotopic constraints on authigenic carbonate formation: Insights from the Chuanlinggou Formation, Yanshan Basin, North China. Geochimica et Cosmochimica Acta 150, 90-105.

Mitchell, K., Mansoor, S.Z., Mason, P.R.D., Johnson, T.M. and Van Cappellen, P. (2016) Geological evolution of the marine selenium cycle: Insights from the bulk shale δ82/76Se record and isotope mass balance modeling. Earth and Planetary Science Letters 441, 178-187.

Moynier, F., Fujii, T., Telouk, P. and Albarede, F. (2008) Isotope Separation of Te in Chemical Exchange System with Dyclohexano-18-crown-6. Journal of Nuclear Science and Technology 45, 10-14.

Perkins, W.T. (2011) Extreme selenium and tellurium contamination in soils--an eighty year-old industrial legacy surrounding a Ni refinery in the Swansea Valley. The Science of the total environment 412-413, 162-169.

Planavsky, N.J., Reinhard, C.T., Wang, X., Thomson, D., McGoldrick, P., Rainbird, R.H., Johnson, T., Fischer, W.W. and Lyons, T.W. (2014) Low Mid-Proterozoic atmospheric oxygen levels and the delayed rise of animals. Science 346, 635.
Planavsky, N.J., Slack, J.F., Cannon, W.F., O'Connell, B., Isson, T.T., Asael, D., Jackson, J.C., Hardisty, D.S., Lyons, T.W. and Bekker, A. (2018) Evidence for episodic oxygenation in a weakly redox-buffered deep mid-Proterozoic ocean. Chemical Geology 483, 581-594.

Qin, H.-B., Takeichi, Y., Nitani, H., Terada, Y. and Takahashi, Y. (2017) Tellurium Distribution and Speciation in Contaminated Soils from Abandoned Mine Tailings: Comparison with Selenium. Environ. Sci. Technol. 51, 6027-6035.

Rahman, M.M., MacDonald, C. and Cornett, R.J. (2018) Separation of tin from tellurium: performance of different extraction chromatographic materials. Separation Science and Technology 53, 2055-2063.

Rudge, J.F., Reynolds, B.C. and Bourdon, B. (2009) The double spike toolbox. Chemical Geology 265, 420-431.

Russell, R.D. (1971) The systematics of double spiking. Journal of Geophysical Research (1896-1977) 76, 4949-4955.

Schirmer, T., Koschinsky, A. and Bau, M. (2014) The ratio of tellurium and selenium in geological material as a possible paleo-redox proxy. Chemical Geology 376, 44-51.

Smith, C. (2012) History and Development of the Golden Wonder Mine: 1874 to 2011. LKA International.

Smith, D.B., Cannon, W.F., Woodruff, L.G., Solano, F. and Ellefsen, K.J. (2014) Geochemical and mineralogical maps for soils of the conterminous United States, Open-File Report, Reston, VA, p. 399.

Smithers, R.M. and Krouse, H.R. (1968) Tellurium isotope fractionation study. Can. J. Chem. 46, 583-591.

Sutton, S.J. and Maynard, J.B. (1993) Sediment- and basalt-hosted regoliths in the Huronian supergroup: role of parent lithology in middle Precambrian weathering profiles. Canadian Journal of Earth Sciences 30, 60-76.

Taylor, D.E. (1999) Bacterial tellurite resistance. Trends in Microbiology 7, 111-115.

Wang, X., Fitoussi, C., Bourdon, B. and Amet, Q. (2017) A new method of Sn purification and isotopic determination with a double-spike technique for geological and cosmochemical samples. Journal of Analytical Atomic Spectrometry 32, 1009-1019.

Wang, Z. and Becker, H. (2014) Abundances of Sulfur, Selenium, Tellurium, Rhenium and Platinum-Group Elements in Eighteen Reference Materials by Isotope Dilution Sector-Field ICP-MS and Negative TIMS. Geostandards and Geoanalytical Research 38, 189-209.

Yarema, M.C. and Curry, S.C. (2005) Acute Tellurium Toxicity From Ingestion of Metal-Oxidizing Solutions. Pediatrics 116, e319-e321.

Yierpan, A., König, S., Labidi, J., Kurzawa, T., Babechuk, M.G. and Schoenberg, R. (2018) Chemical Sample Processing for Combined Selenium Isotope and Selenium-Tellurium Elemental Investigation of the Earth's Igneous Reservoirs. Geochemistry, Geophysics, Geosystems 19, 516-533.

Zweibel, K. (2010) The Impact of Tellurium Supply on Cadmium Telluride Photovoltaics. Science 328, 699-701.

CHAPTER 3: ANTIMONY AND TELLURIUM ISOTOPIC FRACTIONATION INDUCED BY ADSORPTION TO GOETHITE AND ILLITE

Abstract

The fate and transport of the metalloids antimony (Sb) and tellurium (Te) is largely dictated by redox processes. However, in oxic environments, Te and Sb adsorb readily to mineral surfaces, a process that can greatly reduce their mobility. Recently, there has been increasing interest in developing the Sb and Te isotope ratios as tracers of redox reactions in modern or ancient settings, similar to other redox-sensitive elements. However, isotopic fractionation during adsorption, driven by differences in the energetics of the bonding environment between the adsorbed and aqueous species, has the potential to complicate efforts to track redox-driven geochemical changes using isotope ratios. Here, we examine the equilibrium isotopic shifts produced during adsorption of Sb(III) and Sb(V) and Te(IV) and Te(VI) to goethite and illite at pH 6 and 8. Adsorption of Sb(III) and Sb(V) produced differences in $\delta_{aqueous}$- $\delta_{adsorbed}$ of 0.31‰ to 0.39‰ and 0.22‰ to 0.28‰ for adsorption to goethite and illite, respectively, which were indistinguishable within analytical uncertainty. The isotopic fractionation during adsorption of Te(IV) to goethite and illite at pH 6 and 8 was even more muted. Te(VI) adsorption induced a significantly greater isotopic shift of ~0.65‰ for goethite. Sb(V) adsorption to goethite took 1 week to equilibrate isotopically, a much longer period than the other experiments, which attained isotopic equilibrium within hours. In addition, transient isotope effects prior to isotopic equilibrium for Sb(V) adsorption showed an initial decrease in δ^{123}Sb and subsequent rise to isotopically heavy values. In total, these isotope effects are smaller than redox-driven isotope effects by a factor of 3 and should be considered when using Sb or Te stable isotopes to track redox processes.

3.1 Introduction

Measurements of non-traditional stable isotope ratios have helped identify and quantify important pathways that control biogeochemical cycling of metals and metalloids in terrestrial and marine environments. The antimony (Sb) and tellurium (Te) stable isotope systems are currently being explored as new proxies for Sb and Te redox transformations (Wasserman and Johnson, 2020a). Sb and Te, while both trace elements, are considered economically valuable for photovoltaics, nanotechnology, hardening agents in alloys, flame-retardants, and catalysts for plastics (e.g. PET) (Filella et al., 2002; Westerhoff et al., 2008; Zweibel, 2010). In the last century, instances of elevated Sb and Te in soils and waters around mines and processing sites have increased, as demand and extraction of these elements has grown (Ashley et al., 2007; Wang et al., 2011; Wiklund et al., 2018). Because both elements are toxic to animals and humans at concentrations < 1 µg (Cooper and Harrison, 2009; Perez-D'Gregorio et al., 1988a), greater examination of the Sb and Te biogeochemical cycles is essential.

Like other multivalent elements, distinctions in geochemical behavior exist between oxidation states of Sb and Te. Sb(V) forms soluble oxyanions, while Sb(III) is significantly less soluble, forming Sb oxide and sulfide minerals (Filella et al., 2009). The ratio of the two Sb stable isotopes, ^{123}Sb/^{121}Sb, varies due to isotopic fractionation during abiotic and biological reduction and is a promising indicator of Sb biogeochemical processes (Rouxel et al., 2003). Te(VI) and Te(IV) are the more soluble counterparts to the more reduced Te oxidation states, Te(0) and Te(-II) which form insoluble phases. Containing eight isotopes, Te isotopically fractionates in laboratory reduction experiments and displays isotopic variation in natural samples (Baesman et al., 2007; Fukami et al., 2018). These results illustrate the potential of Te and Sb isotope systems as redox proxies, but overall little is known about the isotopic systematics of these two elements. In order to develop these tools, the potential for non-redox processes, such as adsorption, to also cause isotope ratios shifts must be examined.

Isotopic fractionation during adsorption occurs due to differences in metal(loid)-oxygen bond strength between the adsorbed and aqueous coordination spheres. For some redox-sensitive elements, isotope shifts due to adsorption are significant enough in magnitude to complicate redox-driven isotopic fractionation. For example, the largest isotopic fractionation of molybdenum (Mo) occurs during adsorption of MoO_4^{2-} to Mn oxides, during which the aqueous complex transforms from a tetrahedral to an octahedral species when adsorbed (Barling and Anbar, 2004; Wasylenki et al., 2011). Recently, significant Se isotopic fractionation was measured during Se(IV) adsorption to hematite and β-MnO_2 ($\Delta_{\text{aqueous-adsorbed}}{}^{82}Se/{}^{76}Se \sim 0.67$ to 1.24‰) (Xu et al., 2020). Consideration of Se isotopic fractionation during adsorption could alter interpretations of marine paleoredox condition based on the Se isotope record (Mitchell et al., 2012; Stüeken et al., 2015).

Adsorption can also mute redox-induced isotopic shifts if the fractionation factor is much smaller than isotopic fractionation produced by redox processes. Brown et al. (2018) showed that when complexed as Ca-CO_3-U, U(VI) reduction produced a fractionation factor of $\varepsilon^{238}U/{}^{235}U\sim$ 0.23 to 0.83‰. Previous studies had observed no significant or minimal isotopic fractionation during the reaction of dissolved U(VI) and FeS due to fast sorption of U (Stylo et al., 2015). Uranium isotopes are used extensively to monitor U mobility in contaminated sites (Jemison et al., 2020; Shiel et al., 2016) and as a marine paleoredox proxy (Brüske et al., 2020; Chen et al., 2017), and this result had major implications on interpretations of U isotope fractionation. This example highlights that, when not taken into account using a rigorous mass balance, adsorption can skew interpretation of isotopic fractionation factors or the extent of reaction progress.

As both Sb and Te isotopes have the potential to serve as redox proxies in modern and ancient environments, isotopic fractionation during adsorption could either complicate or enhance the use of these elements as redox proxies. This is especially important as both elements adsorb strongly to Fe (oxy)hydroxides and clay minerals (Hein et al., 2003a; Ilgen and Trainor, 2012; Leuz et al., 2006; Qin et al., 2017). Sb adsorption behavior is variable depending on oxidation state. Sb(III) adsorbs to goethite strongly over a full range of pH, but is easily oxidized on the timescale of a day (Leuz et al., 2006). Meanwhile, Sb(V) adsorption to Fe-(oxy)hydroxides and kaolinite is pH-dependent, decreasing with increasing pH (Essington et al., 2017). The mobility of both Te oxidized species, Te(IV) and Te(VI), is influenced by adsorption in oxic systems. As an irregularly coordinated pyramid, Te(IV) species are quickly scavenged in aqueous systems (Lee and Edmond, 1985). Te(VI) adsorbs strongly, but less than Te(IV), to goethite, ferrihydrite, and illite (Qin et al., 2017). Like other oxyanions (e.g. SeO_3^{2-}), inner-sphere complexation of Te could induce isotopic fractionation on goethite surfaces.

The relative influence of adsorption on both isotopic systems depends on the magnitude of the shifts accompanying redox-induced isotopic fractionation. Existing data of Sb isotopic fractionation shows significant shifts during abiotic and biological reduction. This is expressed as ε^{123}Sb, which, to a very close approximation, is equal to $\delta_{reactant} - \delta_{product}$, the isotopic difference between the reactant pool and the product flux. Sb isotopic fractionation has been measured during abiotic reduction by potassium iodide (ε^{123}Sb = -0.90‰) and sulfide (ε^{123}Sb = -1.42‰) in an HCl matrix (Mackinney, 2016; Rouxel et al., 2003). In addition, reduction by various bacterial cultures also produced a significant isotopic shift: Two anaerobic bacterial cultures amended with lactate and tryptone produced a product δ^{123}Sb ~ 0.7‰ less than the reactant during the reduction of $Sb(OH)_6^-$ to $Sb(OH)_3$ (Wasserman, 2018). In addition, natural isotopic variation of δ^{123}Sb displayed a range of 2.0‰ in a suite of hydrothermal sulfides (Rouxel et al., 2003) and ~1.0‰ in mine-affected river waters (Resongles et al., 2015), indicating that fractionating processes are ubiquitous in terrestrial and marine environments.

While few studies have examined Te isotopic fractionation in laboratory studies, results so far exhibit significant isotopic fractionation for abiotic and biological reduction. Baesman et al. (2007) showed that the reduction of Te(IV) and Te(VI) to Te nanorods produced $\varepsilon^{130/125}$Te ~ -4‰ and -5‰ for the two bacterial cultures, *Bacillus selenitireducens* and *Sulfurospirillum barnesii*, respectively. Abiotic isotopic fractionation has been similar in size for Te. Smithers and Krouse (1968) reported $\varepsilon^{130/125}$Te of -4.4‰ during Te(IV) reduction with sulfite, while reduction of Te(IV) with cysteine produced $\varepsilon^{130/125}$Te of -2.4‰. A range of $\delta^{130/125}$Te ~ 1.21‰ has been observed in various terrestrial sediments and similarly for chondritic meteorite samples (Fehr et al., 2018; Fukami et al., 2018; Wasserman and Johnson, 2020a).

Here, we present results of an experimental study to examine the isotope effects during adsorption to goethite (FeO(OH)) and illite ($(K,H)Al_2(Si,Al)_4O_{10}(OH)_2$-$nH_2O$). Illite and goethite provide an interesting comparison in this regard, due to their varying surface charge, structure, and active binding sites. The point of zero charge (pzc), or the pH at which the mineral surface is neutral, can influence the mode of adsorption. The pzc of goethite is 7.0 to 9.0 while that of illite is approximately 2.5 (Hussain et al., 1996; Venema et al., 1998). Within the range of pH examined here, illite is negatively charged while goethite is mostly positively charged. Therefore, negatively charged oxyanions of both Te and Sb will be electrostatically attracted to goethite and then undergo inner-sphere complexation. Adsorption to illite, meanwhile, must be primarily through inner-sphere complexation as both surface and ion are negative. Given the moderate magnitude of Sb and Te isotopic fractionation due to reduction, isotopic shifts as a result of adsorption need to be explored. We (1) present methods to measure δ^{123}Sb of Sb(III) and Sb(V), (2) report isotopic fractionation prior to and after isotopic equilibrium is reached, and (3) discuss likely mechanisms for isotopic fractionation and implications for applications of the Sb and Te isotope systems.

3.2 Methods

3.2.1 Experimental materials and stock solutions

The sorbent material used in this study was Bayferrox Yellow 910 synthetic goethite and illite obtained from Gavi Island, Italy (Ylagan et al., 2000). All substrates were powdered and sieved so that the grain diameter was between 0.15 mm and 0.25 mm. The synthetic matrix for every adsorption experiment had an ionic strength of 0.08 M (NH_4Cl, KCl, and NaCl) and was buffered by 3 g L^{-1} PIPES.

Sb stock solutions were prepared by dissolving Sb_2O_3 powder (Acros Organics, CAS 1309-64-4, lot AO312974) in a solution containing 2.0 M distilled HCl and 0.02% (m/v) ascorbate for the Sb(III) adsorption experiments and $SbCl_5$ (Sigma-Aldrich) in 2 M HCl for the Sb(V) experiments. All solutions containing Sb(III) were kept in amber glass vials or wrapped in aluminum foil to reduce the possibility of Sb(III) photo-oxidation. In order to ensure that Sb(III) was reduced, a 0.05% (m/v) KI and ascorbate solution was allowed to react with an aliquot of the dissolved Sb_2O_{3s} standard for 3 hours. Te stock solutions consisted of National Institute of Standards and Technology (NIST) 3156 Te concentration standard (lot no. 140830) in 2 M HCl and Alfa Aesar $H_2TeO_4 \bullet 2H_2O$ powder reagent (99% metals basis, low no. Y05A029) dissolved in 18.2 MΩ Milli-Q H_2O. The Te(IV) reagent was reacted in 5 M HCl on a hot plate at 90°C for 2 hours to ensure any Te(VI) present was reduced, while an aliquot of Alfa Aesar Te(VI) reagent was oxidized in 0.1 M HCl with 0.02 M $K_2S_2O_8$ for 1.5 hours to ensure any Te(IV) was oxidized to Te(VI).

3.2.2 Experimental setup

The pH of the synthetic matrix was adjusted in each reactor with HCl or NaOH prior to the addition of Te or Sb and measured periodically throughout the experiment. The pH of each experiment was adjusted to either 6 or 8 to span much of the range of environmentally relevant waters such as groundwater or seawater. In addition, Sb(V) adsorption is pH-dependent in this range and thought to form outer-sphere complexes at pH> 7. The behavior of Sb adsorption to illite over a wide range of pH has not been thoroughly investigated (Leuz et al., 2006). Several reactors from pH 3 to 10 were set up to examine the general adsorption affinity of Sb(III) and Sb(V) to illite over a wide pH range.

Reactors containing Sb(III) were purged with O_2-free $N_{2(g)}$ for 3 hours and crimp-sealed to prevent oxidation by dissolved O_2. Over the pH range examined here, the kinetics of oxidation are slow (significant reaction requiring weeks in contact with air) (Leuz and Johnson, 2005). However, there is evidence of fast oxidation of Sb(III) during adsorption onto Fe-(oxy)hydroxides in the presence of O_2 (Leuz et al., 2006). The reactors were also wrapped in aluminum foil to prevent photo-oxidation of Sb(III) (Kong et al., 2016). After the addition of Sb or Te, all reactors were allowed to equilibrate for 3 hours prior to the addition of solid. In order to maintain homogeneous conditions in each experiment, the reactors were agitated on a shaker table at 100 rpm. All experiments contained 1 $\mu g\ L^{-1}$ Te or 1.5 $\mu g\ L^{-1}$ Sb initially. Enough goethite or illite was added so that more than 50% of dissolved Te, and at least 20% of dissolved Sb was adsorbed after each sorbent addition (Table 3.1).

The reactors were sampled with a needle and syringe in 1-2 mL aliquots of the suspension, which were immediately filtered with a 0.22 µm nylon syringe filter. Sb(III) samples were taken in a low-light environment and immediately preserved with ascorbic acid, acidified with HCl to pH 2, and refrigerated. Approximately, 4 mL of $N_{2(g)}$ was injected into the Sb(III) reactors after sampling to maintain positive pressure. Sb(V) and Te samples were acidified with HCl to pH 2.0 and refrigerated.

Initially, batch reactor experiments were set up to identify how long each experimental condition needed for isotopic equilibrium to be achieved, and to examine any transient, kinetically driven isotope effects. For each condition tested, 2 mL of the illite or goethite experiment was sampled at several timepoints over 72 hours to 1 week and measured for Te, Sb(V), and Sb(III) concentrations and isotopes in the filtrate. Experiments for Sb(V) were sampled over a longer time period of 2.5 weeks, due to the long isotope equilibration time period for Sb(V) adsorption.

A second set of experiments was conducted with the aim of more precisely determining fractionation factors after isotopic equilibrium was achieved. This was carried out in a series of batch reactor experiments, where dissolved Sb or Te was subjected to multiple stages of isotopic equilibration after addition of adsorbent, followed by removal of adsorbent. Experiments containing Te(IV) and Te(VI) were allowed to react for 48 hours before sampling, in order for isotopic equilibrium to be reached. Sb(V) experiments were allowed to react for 1 week, while reactors containing Sb(III) were sampled after 12 hours. After each reactor was sampled, the entire suspension was filtered with a 0.22 µm PTFE syringe filter and transferred to a clean reactor. Subsequently, fresh sorbent was added to the reactor with 1 to 2 mL of matrix solution to initiate the next stage of adsorption. Each experiment was subject to three stages of sorbent addition. Each experiment was repeated at least twice.

3.2.3 Anion exchange procedures

3.2.3.1 Sb purification

A modified anion exchange procedure from (Łukaszczyk and Żyrnicki, 2010) was used to separate Sb from matrix interferences and separate Sb(III) from Sb(V). Approximately 1.5 mL of cleaned BioRad AG1-X8 resin (100-200 mesh, BioRad Laboratories) was loaded into 10 mL acid-cleaned polypropylene columns. All Sb samples were acidified to 1.5 M HCl at least 1 hr prior to column purification. Initially, the resin was cleaned with 30 mL of Milli-Q H_2O followed by 10 mL of 1.5 M HCl. Less than 1 mL of sample containing no more than 10 μg of Sb was loaded in a matrix of 0.02% (m/v) ascorbic acid and 1.5 M HCl. The Sb(V) fraction was eluted with 10 mL of 1.5 M HCl into a 25 mL borosilicate glass vial with Teflon-lined cap, and was later reduced by KI to Sb(III) for additional separation from Te, Sn, and the matrix. The Sb(III) fraction was collected via addition of 10 mL of 18.2 MΩ Milli-Q water. Both fractions were acidified with distilled concentrated HCl to 2 M HCl and reduced with 0.05% (m/v) KI prior to measurement by Hydride Generation Multi-collector Inductively Coupled Plasma Mass Spectrometry (HG MCICPMS).

3.2.3.2 Te purification

Unlike Sb, which only has two isotopes, there are eight Te isotopes, which allows for the development of a Te double spike. Any isotopic fractionation due to sample preparation or variations in instrumental mass bias can be corrected by the use of the double spike. After concentration measurements (see below), enough ^{120}Te-^{124}Te double spike was added so that the molar spike to sample ratio was ~1. The sample-spike mixture was allowed to equilibrate for at least 24 hours prior to sample purification.

Purification of Te extracted from digestions of the solids followed the “Fe-column” procedure as described in (Wasserman and Johnson, 2020a). Two anion exchange columns were used to purify aqueous Te samples from isobaric (Sn) and matrix interferences. The first column contained 1 mL BioRad AG1-X8 resin (100-200 mesh, BioRad Laboratories) and removed most of the sample matrix. Briefly, Te(VI) was reduced to Te(IV) by heating at 110°C in 5 M HCl for 2 hours and Te(IV) samples were acidified to 5 M HCl. The sample was loaded onto the column in 2 mL 5 M HCl followed by a rinse of 10 mL of 6 M HCl, 5 mL of 9 M HCl and elution of Te(IV) by 4 mL of 0.4 M HCl. The collected sample was dried down and dissolved in a solution of 1 mL 0.1 M HCl and 0.02 M $K_2S_2O_8$. Conversion from Te(IV) to Te(VI) was complete after heating this solution on the hot plate at 110°C for 90 minutes. The second column separated Sn, an isobaric interference, from Te. The oxidized sample was loaded onto a 1 mL column (AG1-X8 resin, 100-200 mesh) that had been pre-conditioned with 5 mL 0.4 M HCl. The Te(VI) fraction was immediately collected with 4 mL of 0.4 M HCl, while Sn(IV) was retained by the column.

3.2.4 Analytical methods

3.2.4.1 Sb and Te concentration measurements

All initial concentration measurements to monitor reaction progress and to calculate the addition of spike were made on an iCAP Q ICP-MS (Thermo Scientific Instruments). The isotopes ^{125}Te and ^{121}Sb were measured along with ^{57}Fe and ^{118}Sn. Te and Sb calibration standards and samples were diluted in 2% (v/v) HNO_3. An online internal standard containing 10 ng mL^{-1} ^{115}In was used to correct for instrumental drift and matrix effects. The limits of detection were 0.02 and 0.03 ng mL^{-1} and the limits of quantification were 0.3 and 0.4 ng mL^{-1} for Te and Sb, respectively.

The more precise Te concentrations reported below were obtained using isotope dilution. As for other isotope systems, this method takes advantage of the ^{120}Te-^{124}Te double spike addition to allow for calculation of the spike to sample ratio. The mass of spike added is known, and the concentration of the sample can be determined from the measured $^{124}Te_{spike}/^{126}Te_{sample}$ ratio.

In order to detect any Sb(III) oxidation over the course of an experiment, Sb(III) and Sb(V) were separated using anion-exchange procedures described above and measured on the iCAP ICP-MS. Both species were monitored over the course of each experiment.

3.2.4.2 Sb and Te isotope measurements and calculations

3.2.4.2.1 Te and Sb isotopic notation

Te and Sb isotopic ratios are expressed using delta notation, following conventions used in Rouxel et al. (2003) and (Wasserman and Johnson, 2020a):

$$\delta^{123}Sb = [\frac{^{123}Sb/^{121}Sb_{sample}}{^{123}Sb/^{121}Sb_{standard}} - 1] * 1000 \tag{3.1}$$

$$\delta^{130}Te = [\frac{^{130}Te/^{126}Te_{sample}}{^{130}Te/^{126}Te_{standard}} - 1] * 1000 \tag{3.2}$$

The sample ratio is reported as a per mil deviation from the average ratio of the two bracketing standards. In the case of Sb, this is the in-house Sb_2O_3 standard AOA14, while that for Te is NIST SRM 3156.

Assuming closed system behavior, the isotopic fractionation due to adsorption at isotopic equilibrium (Δ) can be calculated in the following manner.

$$\Delta_{aqueous-adsorbed} = \delta_{aqueous} - \delta_{adsorbed} \tag{3.3}$$

Extraction of the adsorbed δ^{123}Sb, however, had the potential to induce isotopic fractionation, as no Sb double spike exists to correct for isotopic fractionation during sample preparation. In addition, no method has been developed yet to separate Sb from potential matrix and isobaric interferences, like Fe, Te, Sn. Therefore, solid phase measurements were foregone in favor of solution-phase measurements that have the added advantage of enabling multi-stage experiments that yield higher precision determination of $\Delta_{\text{aqueous-adsorbed.}}$

Assuming the experiment displays closed system behavior, the fractionation at isotopic equilibrium ($\Delta_{\text{aqueous-adsorbed}}$) can be obtained via a mass balance model using only the aqueous data. Effectively, the $\Delta_{\text{aqueous-adsorbed}}$ describes the change in the dissolved Sb isotopic composition ($\delta^{123}Sb_{aq}$) from the initial isotopic composition ($\delta^{123}Sb_{o)}$ for a given fraction of Sb adsorbed (f_{ads}). This is expressed mathematically as,

$$\delta^{123}Sb_{aq} - \delta^{123}Sb_o = \Delta^{123}Sb * f_{ads} \tag{3.4}$$

Here, f_{ads} is equivalent to 1 - f_{aq}, where f_{aq} is the fraction of Sb remaining in solution after a single stage of adsorption. Both f_{ads} and f_{aq} be calculated using the aqueous concentration data. Over multiple steps (j) of repeated adsorption, the cumulative amount of adsorption can be expressed as

$$\Sigma f_{ads} = \sum_{i=1}^{j} f_{adsorbed,i} \tag{3.5}$$

The total change in $\delta^{123}Sb_{aq}$ from $\delta^{123}Sb_o$ will increase linearly with the cumulative adsorption fraction (Σf_{ads}), with the slope equal to $\Delta^{123}Sb_{\text{(aqueous-adsorbed)}}$:

$$\delta^{123}Sb_{aq} - \delta^{123}Sb_o = \Delta^{123}Sb * \Sigma f_{ads} \tag{3.6}$$

The addition of more stages increases Σf_{ads} and allows for a more precise determination of $\Delta^{123}Sb_{(aqueous\text{-}adsorbed)}$, as the greater range in Σf_{ads} provides greater "leverage" in constraining the slope.

All Δ^{123}Sb and Δ^{130}Te values were calculated using this method. Solid samples from four different Te adsorption experiments were digested and measured to provide an additional check on the validity of this model. The Δ^{123}Sb or Δ^{130}Te and associated standard uncertainties of these factors were calculated using a standard least squares linear regression method.

3.2.4.2.2 Hydride generation

Sb and Te isotope measurements were made using Hydride Generation (HG) MCICPMS (Nu Plasma, North Wales, UK) at the University of Illinois at Urbana-Champaign. Hydride generation converts Sb and Te to gaseous hydrides (H_3Sb and H_2Te). These species are delivered efficiently to the plasma, although recent work showed that the sensitivity of hydride generation for Te is roughly equivalent to that of desolvating nebulization methods (Wasserman and Johnson, 2020a). However, there are significant advantages to hydride generation, including the avoidance of non-hydride forming interferences like ^{130}Ba on ^{130}Te.

The methods for hydride generation of $H_2Te_{(g)}$ have been discussed at length in previous studies (Brennecka et al., 2017). Briefly, Te(VI) cannot be reduced to form $H_2Te_{(g)}$, so all Te in the sample was reduced by heating in 5 M HCl for 2 hours at 110°C prior to analysis. Subsequently, all standard, sample, and blank solutions were adjusted to 4.0 M HCl for introduction into the HG system.

Formation of $H_3Sb_{(g)}$ is more favorable for Sb(III) and Sb(V), so pre-reduction of Sb is crucial. KI acts as an effective reductant in acidic solutions, and ascorbate acts as a preservative

(Rouxel et al., 2003). All sample and standard matrices were adjusted to 2.0 M HCl with 0.05% (m/v) KI and ascorbic acid. Complete reduction took place over 3 hours.

The sample or standard solutions for both Te and Sb were reacted via on-line continuous mixing with a reducing solution of 0.2% $NaHB_4$ and 0.2% NaOH. Uptake rates of the sample and reductant in both systems were 0.9 mL min^{-1} and 0.5 mL min^{-1} respectively. $H_3Sb_{(g)}$ and $H_2Te_{(g)}$ were transferred into the plasma with an Ar carrier gas at 1.15 L min-^{1}.

3.2.4.2.3 Sb mass spectrometry

The two isotopes of Sb, ^{121}Sb (57.21%) and ^{123}Sb (42.79%), were measured using the Axial and L2 Faraday collectors connected to amplifiers with standard 10^{11} Ω resistors. There is one potential major isobaric interference, ^{123}Te, which can be corrected for up to [Te]:[Sb] ~ 1 by monitoring the intensity of ^{126}Te on the H3 collector. Other smaller interferences, like $^{122}TeH^+$ and $^{122}SnH^+$, are expected to be inconsequential and are not corrected for. Sn is a common trace metal in $NaBH_4$ and typically ^{117}Sn, which is monitored on the L4 collector cup is 20-25 mV. Given a similar hydride formation rate as Te (TeH^+/Te of 10^{-4} as observed from previous studies (Wasserman and Johnson, 2020a)), $^{122}SnH^+$ would contribute ± 0.0004‰ of the typical ^{123}Sb intensity. Contribution of $^{122}TeH^+$ is likely to be even less, considering the rarity of ^{122}Te and anion-exchange procedures to get rid of Te. Still, both ^{126}Te and ^{120}Sn are monitored to detect any significant interferences.

As there is no double spike for Sb isotope measurements to correct for drift in instrumental mass bias or matrix effects, rigorous quality checks are required. All samples are bracketed by the in-house standard (AOA14) from the stock of Sb_2O_3. Every 4 samples, a secondary fractionated standard, "FUCA15b" was measured (-0.78 ± 0.08 ‰). The $^{123}Sb/^{121}Sb$ of the bracketing standard was used to monitor drift in the instrumental mass bias over the run. If the bracketing standard varied by more than ± 0.10‰ (2σ) from the average AOA14 ^{123}Sb/^{121}Sb, the instrument was retuned. Duplicates analyses were measured for all samples and triplicates were measured for 80% of the samples in this study. Replicate analyses were not measured sequentially to ensure that the isotopic ratio was independent of the mass spectrometer conditions. Processed standards and experimental controls with the same matrix as the experiment were measured alongside samples to evaluate matrix effects on δ^{123}Sb. The δ^{123}Sb of controls were on average -0.01 ± 0.08 ‰ (n=12). Eight reactors containing blank solutions contained, on average, 0.03 ng mL^{-1} Sb.

Baseline noise was measured over an integration time of 10 seconds as the ion beam was deflected by the electrostatic analyzer, and subsequently corrected for. Approximately 0.75 to 1.5 ng mL^{-1} Sb was introduced to produce an intensity of 3.0 V – 5.0 V on ^{123}Sb for good counting statistics. Prior to each measurement session, a 1 ng mL^{-1} AOA14 standard spiked with 0.25 ng mL^{-1} Te was analyzed to check the Te correction. Measurements averaged three blocks of 10 measurements, each integrating over 3 seconds and peak centering on ^{121}Sb prior to each block. A complete washout of Sb memory was achieved by rinsing with 2.0 M HCl for 4 minutes after each analysis. The long-term precision of this method was 0.06‰ (2σ) (n = 82) based on multiple measurements of processed FUCA15 standards. On average, triplicate measurements over an analytical session had an average precision of 0.05‰ (2σ) (n = 19).

3.2.4.2.4 Te mass spectrometry

Te isotope measurements were set up following procedures in Wasserman and Johnson (2020). Briefly, ^{120}Te, ^{123}Te, ^{124}Te, ^{125}Te, ^{126}Te, and ^{128}Te were measured using Faraday cups L3, L1, Ax, H1, H2, and H4, which were connected to amplifiers with standard resistors. H5, which was used to measure ^{130}Te, has a 10^{10} Ω resistor, which had been installed to perform U isotope analyses with high ^{238}U intensities. Approximately 2.5 ng mL^{-1} Te produced 1.5 V on ^{130}Te, which allowed for good counting statistics and lower impact of baseline noise on less abundant isotopes (e.g. ^{126}Te). Sn, Xe, and hydride isobaric interferences were present on masses 120 (Sn), 124 (Sn), 126 (Sn and Xe), 128 (Xe), and 130 (Xe) and were mostly corrected for by on-peak zeroes prior to measurement. These interferences were corrected by measuring the intensities of ^{118}Sn on L4 and ^{132}Xe on H6, and calculating the residual intensities of ^{120}Sn, ^{124}Sn, ^{126}Sn, ^{126}Xe, ^{128}Xe, and ^{130}Xe assuming the natural isotopic composition of Sn and Xe and using the instrumental mass bias obtained in the Te data reduction. Hydrides were assumed to form at a constant rate ($TeH^+/Te \sim 10^{-4}$) determined at the beginning on the run. All of these corrections were incorporated into the iterative routine for the double spike reduction.

The bracketing standard, NIST SRM 3156, was measured every four samples. A secondary standard, Alfa Aesar Te(VI) (0.84 ± 0.09‰ (2σ)), was measured every 10 samples over the course of the run. ^{123}Te^{1}H^{+} impacts the ^{124}Te spike isotope, therefore, lower and higher spiked samples can differ isotopically if this interference was not corrected for. Prior to each run, low and high spiked standards were measured to obtain the TeH^{+}/Te correction, which was then used to correct for ^{123}Te^{1}H and ^{124}Te^{1}H. Care was taken to limit the precipitation of Te(0) in the hydride generation system, which can cause depression of signal and persistent memory (Brennecka et al., 2017). To accomplish this, solutions greater than 5 ng mL^{-1} Te were avoided and the sample probe was rinsed with 0.5 M HCl initially prior to a three-minute rinse with 2 M HCl. Seven experimental controls were on average 0.02 ± 0.11‰ (2σ) and reactors with only the matrix present contributed 0.05 ng Te (n=8). Based on 6 pairs of duplicates, the average uncertainty δ^{130}Te was 0.12‰ (2σ).

3.3 Results

3.3.1 Sb ion exchange separations and Sb(III) preservation

Antimony elution curves show the separation of Sb(V) and Sb(III) species using anion exchange chromatography (Figure 3.1). Sb(V) and Sb(III) in aqueous sample were separated completely from each other and from the rest of the matrix. Briefly, when the eluent was HCl with concentration between 1.0 M and 2.0 M, Sb(III) was retained on the resin, while Sb(V) was eluted with the matrix. Isobaric interferences, like Te(IV),Te(VI), and Sn(IV), eluted with the Sb(V) matrix, which could then be separated in the second purification step.

Fast oxidation of Sb(III) occurred during acidification with HCl in the absence of an oxidation inhibitor, possibly due to trace oxidants in the matrix like iodate in the stock HCl (Quentel et al., 2006). When ascorbic acid was not added as a preservative prior to acidification, Sb(III) was oxidized within a matter of minutes resulting in low recovery (<2%) of Sb(III).

3.3.2 Adsorption of Te and Sb to illite and goethite

Our results show that Sb(V) adsorption was greater for goethite rather than illite. Like previously observed behavior with other oxyanions (Balistrieri and Chao, 1987; Dixit and Hering, 2003), equilibrium Sb(V) adsorption to illite shows strong pH-dependence, decreasing in adsorption affinity above pH 6 (Figure 3.2). This is similar to the pH-dependence of Sb(V) to goethite reported by Leuz et al. (2006) A higher fraction of adsorbed Sb(V) on goethite was observed for pH 6 compared to pH 8 conditions in our experiments as well (Figure 3.3). Sb(III)adsorption, meanwhile, did not vary with increasing pH, possibly indicating similar adsorption mechanisms across the range of pH. Sb(III) also showed a higher affinity than Sb(V) for illite over the range of pH (Figure 3.2). There was no difference for Sb(III) adsorption between the two sorbents. Te(IV) and Te(VI) at pH 6, meanwhile, adsorbed to goethite and illite in similar magnitudes, with a greater amount of Te adsorbed to goethite relative to illite. This is consistent with the adsorption affinity for these two minerals in Qin et al. (2017).

Tellurium and antimony adsorption to both sorbents reached steady state on the order of hours (Figures 3.3 and 3.4). Within 1 hr, dissolved Sb concentrations reached equilibrium in all reactors (Figure 3.3). The loss of Sb(III) from solution after 24 hours is related to oxidation as indicated by the appearance of Sb(V) after this timepoint (Figure 3.3). Meanwhile, Te concentrations reach steady state after 3 hours in all conditions (Figure 3.4). No difference was observed between the Te(VI) and Te(IV) in terms of the kinetics of adsorption. Tellurium adsorption to illite achieved chemical equilibrium slightly more quickly than adsorption to goethite.

3.3.3 Sb and Te isotopic fractionation prior to isotopic equilibrium

Sb(III) adsorption to goethite and illite and Sb(V) adsorption to illite appeared to reach isotopic equilibrium within 10 hours (Figure 3.3). For Sb(III) adsorption to goethite, the increase in $\delta^{123}Sb_{aq}$ at 24 hours at pH 8 correlated with the onset of Sb(III) oxidation as shown in Figure 3.3. During adsorption of Sb(V) to goethite, $\delta^{123}Sb_{aq}$ reached isotopic equilibrium after ~1 week (Figure 3.5), a rather long time compared to other conditions.

Sb (V) adsorption to goethite and illite resulted in a non-linear evolution of $\delta^{123}Sb_{aq}$ prior to the attainment of isotopic equilibrium. Sb(V) reached isotopic equilibrium during adsorption on illite at 3 hours after an initial decrease in $\delta^{123}Sb_{aq}$ of -0.25 to -0.29‰ within the first hour and subsequent rise of 0.30 and 0.40‰ (Figure 3.5). Within the first 24 hours of Sb(V) adsorption on goethite, $\delta^{123}Sb$ decreased to ~0.5‰ isotopically lighter than the starting solution. No such transient decrease was observed in the first part of the Sb(III) experiment to illite or goethite (Figure 3.5).

During adsorption to illite, both Te(IV) and Te(VI) reached isotopic equilibrium at 3 hours (Figures 3.6A, 3.6C). Te(IV) and Te(VI) adsorption to goethite showed similar rapid isotopic equilibration (Figures 3.6B, 3.6D). Prior to isotopic equilibrium being reached, the evolution of δ^{130}Te did not display the distinct, early isotopic depletion observed with Sb(V).

3.3.4 Sb and Te equilibrium isotopic fractionation

The aqueous data from the Te and Sb equilibrium adsorption experiments fit well to predicted linear evolution (Equation 3.6) of aqueous δ^{123}Sb in multi-stage experiments (Figures 3.7 and 3.8). In addition, the δ^{130}Te of the solid falls on the predicted isotopic fractionation for adsorbed Te in the 4 cases where the solid was measured. In addition, no oxidation of Sb(III) occurred, as aqueous Sb(V) remained at undetectable levels (< 0.4 ng mL^{-1}) during the isotopic equilibrium experiments with Sb(III).

The adsorption of Sb produces a positive equilibrium Δ^{123}Sb for all conditions (Figure 3.7). The equilibrium Δ^{123}Sb of Sb(III) with goethite (pH 6: 0.31, pH 8: 0.32) and Sb(V) with goethite (pH 6: 0.39, pH 8: 0.34) is the same within analytical uncertainty (Table 3.2). Sb adsorption to goethite resulted in equilibrium Δ^{123}Sb values identical to those observed with adsorption to illite. Unpaired Student t-tests comparing Sb adsorption with illite and goethite showed no statistical difference between the means of the two groups ($p > 0.05$).

Tellurium adsorption to illite and goethite results in enrichment of ^{126}Te in the adsorbed fraction at equilibrium (Figure 3.8). In experiments with both illite and goethite, Te(VI) isotopic fractionation was larger than Te(IV). Indeed, equilibrium Δ^{130}Te was relatively small for Te(IV) adsorption to both minerals, ranging from Δ^{130}Te of 0.12 to 0.25‰ (Table 3.2). Adsorption to goethite by Te(VI) produced the largest Δ^{130}Te in this study of 0.68‰ at pH 6 and 0.64‰ at pH 8.

For both Te and Sb, very little pH-dependence of isotopic fractionation was observed. Even for Sb(V) adsorption to goethite and illite, which shows different sorption affinity between pH 6 and 8 (Figure 3.2), no difference in isotopic fractionation was observed between the two conditions (Table 3.2). Unsurprisingly, no significant isotopic difference was observed between the two pH conditions for Te during adsorption to goethite and illite (Table 3.2).

3.4 Discussion

3.4.1 Antimony column chemistry and mass spectrometry

The complete separation of Sb(V) and Sb(III) in Figure 3.1 reflects the formation of Sb chloride species. In 1.5 M HCl, Sb(V) formed a neutrally charged chloride species, $Sb(OH)_xCl_{(5-x)}^0$, and was immediately eluted from the column. Sb(III) formed negatively charged chloride species, $SbCl_6^{3-}$ and $SbCl_4^-$, which were retained on the resin during the 1.5 M HCl elution step (Łukaszczyk and Żyrnicki, 2010). Very quickly after the chloride concentration decreases following the addition of H_2O, Sb(III) is eluted as a soluble $Sb(OH)_3^0$ species.

While full recovery occurred for Sb(V) and Sb(III) in dilute solutions, the addition of more complex matrices may affect the separation and isotopically fractionate the collected fractions. For example, low-molecular organic species can complex with Sb(III) and could potentially overwhelm the anion adsorption capacity of the resin (Tella and Pokrovski, 2009). In addition, sulfide-bearing waters cannot be processed, as Sb(III) precipitates readily as metastibnite in acidic conditions. Purging volatiles from samples with N_2 could effectively drive off $H_2S_{(g)}$ and preserve speciation in these samples.

3.4.2 Te and Sb adsorption behavior

Both Te and Sb species show a high affinity for adsorption to illite and goethite. This is a result of the creation of bonds between the Te and Sb atoms and mineral surfaces through inner-sphere coordination mechanisms well documented in EXAFS studies (e.g. Kashiwabara et al. (2014a); Xi and Zhang (2017)). Guo et al. (2014) and showed that there are two Sb-Fe shells when Sb is adsorbed to goethite and similar results have been reported for Sb adsorption to kaolinite (Ilgen and Trainor, 2012). Qin et al. (2017) reported that at least one Te-Fe shell is present during adsorption of Te to goethite surfaces.

The adsorption affinity of a mineral surface can vary greatly depending on pH, due to changing aqueous speciation, mineral surface charge, and mineral structure. With increasing pH, fewer protonated sites exist on illite and goethite for Sb(V), as $Sb(OH)_6^-$ to bind to. This decreases the adsorption capacity as observed in Figure 3.2. Te does not show similar pH dependence, as both Te(IV) and Te(VI) are stronger Lewis bases than Sb(V). The average pKa for the first two deprotonation reactions of H_2TeO_3 and H_6TeO_6 are ~7.5 and 9, respectively (Qin et al., 2017). $Sb(OH)_3$ has an even higher pKa of 11.9. Meanwhile, the pKa of the first deprotonation reaction of $Sb(OH)_6^-$ is 2.8 (Qi and Pichler, 2017). Therefore, surface hydroxyl groups can serve a Lewis acids for Te(IV), Te(VI), and Sb(III) at higher pH than Sb(V), and Te adsorption is less-pH dependent

Previous studies have reported long periods required to reach steady-state concentrations during inner-sphere complexation as metalloid-oxygen bonds must be severed and reattached to the mineral surface (Leuz et al., 2006; Xu et al., 2020; Zhang et al., 2010). All Te and Sb aqueous concentrations reached chemical equilibrium within several hours at pH 6. Interestingly, there was no measurable difference between Sb(III) and Sb(V) concentrations in terms of time to reach steady state, despite differences in isotopic equilibration time and kinetic isotope effects between the two oxidation states. This result suggests that the relationship between the attainment of isotopic equilibrium and that of chemical equilibration is complex.

3.4.3 Behavior of Te and Sb isotopic fractionation during adsorption

The coordination geometries of the adsorbed oxyanions differ from those in the fluid; this drives isotopic fractionation. Metal and metalloid oxyanions can bond to surfaces as two different types of complexes, inner-sphere and outer-sphere. Inner-sphere complexes are direct linkages between the metal(loid) center and the mineral surface, while outer-sphere complexation involves electrostatic interaction between the hydration spheres on the oxyanion and water molecules on the mineral surface (Dzombak, 1990). Minimal isotopic fractionation occurs during outer-sphere complexation, as the reaction does not involve bonding to the metal(loid) and the first coordination shell remains undisturbed (Jemison et al., 2016). As described in Schauble (2004), at equilibrium, heavy isotopes partition preferentially into shorter, stiffer bonds to maximize the difference in vibrational energies for the reactant and product. Structural distortion of the oxyanion (e.g. Xu et al. (2020)) or transformation to different coordination geometry (Nielsen et al., 2013; Wasylenki et al., 2011) during adsorption can result in significant differences in the bond length and stiffness between the metal(loid) and oxygen. EXAFS studies confirm that no change in coordination number occurs for Te and Sb during adsorption to Fe oxides and clay minerals (Guo et al., 2014; Ilgen and Trainor, 2012; Qin et al., 2017). Therefore, the isotopic fractionation observed here must be due to distortion of the Te-O or Sb-O first coordination shells of the adsorbed species. Here, distortion refers to the lengthening of some or all Te-O and Sb-O bonds as the result of a loss of symmetry for the Te or Sb oxyanions when adsorbed. Similar mechanisms for isotopic fractionation have been proposed for tungstate adsorption to MnO_2, germanium (Ge) adsorption to goethite, and other instances of isotopic fractionation during adsorption (Brennecka et al., 2011; Kashiwabara et al., 2017;

Pokrovsky et al., 2014). The resulting magnitude and direction of isotopic fractionation depends on these molecular changes between surface and adsorbed species.

For all conditions, Δ^{123}Sb and Δ^{130}Te was positive, suggesting that distortion of the metal(loid)-oxygen bonds caused heavy isotopes to partition into the stiffer bonds of the aqueous phase. Modes of Te and Sb complexation to Fe oxides and clay minerals can give some insight into the mechanism of isotopic fractionation. For example, a higher number of bonds between the Sb or Te and the surface can lead to a greater distortion of the remaining Sb-O or Te-O (Brennecka et al., 2011). In addition, for bidentate linkages, or where the metalloid is bonded to two atoms on the mineral surface, distortion and isotopic fractionation can vary depending on if the two bonds are corner-sharing (mononuclear) or edge-sharing (binuclear) (Kashiwabara et al., 2017).

Sb(III) and Sb(V) isotopic fractionations during adsorption to illite and goethite are equal within analytical uncertainty. While $Sb(OH)_3$ is a trigonal pyramidal complex and $Sb(OH)_6^-$ is octahedral, both form similar corner- or edge-sharing bidentate-binuclear complexes without any coordination number change (Burton et al., 2020; Guo et al., 2014; Ilgen and Trainor, 2012; Mitsunobu et al., 2010). Reported average Sb-O bond length (Sb(III): 1.96 and Sb(V): 1.98) is also similar between species, suggesting no inherent difference in bond stiffness between the aqueous species (Ilgen and Trainor, 2012). This may contribute to the similarity in the magnitude of isotopic fractionation between Sb(III) and Sb(V).

Te(VI) adsorption produced a larger isotopic shift than Te(IV) adsorption. Te(IV) and Te(VI) oxyanions have pyramidal and irregularly coordinated octahedral geometry, respectively. EXAFS spectra indicate that Te(IV) forms monodentate linkages on goethite and ferrihydrite, while bidentate complexes bind Te(VI) oxyanions (Kashiwabara et al., 2014a). The presence of two linkages between Te(VI) and the surface may lead to distortion of the remaining Te-O bonds and loss of symmetry for the adsorbed species. Meanwhile, Te(IV)-O distortion, and thus isotopic fractionation, could be more muted given the reported monodentate linkage.

3.4.4 Mechanisms of isotopic fractionation prior to isotopic equilibrium

Isotopic equilibrium often lags significantly behind chemical equilibrium, as kinetic isotope effects that occur prior to chemical equilibrium being reached must be overprinted by ongoing isotopic exchange after concentrations have approached equilibrium (Bryan et al., 2015; Fernandez et al., 2019; Xu et al., 2020). This is the case for 3 of the 4 Sb experiments, where isotopic equilibrium was approached in between 3 and 10 hours, whereas concentrations reached steady state within 3 hours. In the 4th experiment, Sb(V) adsorption to goethite, concentrations approached a steady state within hours, where isotopic equilibration took ~1 week. In this 4th experiment, the long equilibration time may reflect recrystallization of goethite over time. Recently, Burton et al. (2020) showed that Sb(V) can be incorporated into the goethite matrix during the process of $Fe(II)_{(aq)}$-catalyzed recrystallization over a period of hours. While Fe(II) concentrations were likely very low and were not monitored over the course of our experiment, some type of recrystallization of the sorbent may have influenced the long duration of isotopic change. Such a mechanism for Te incorporation has been proposed for co-precipitation of ferrihydrite, but not for goethite (Kashiwabara et al., 2014a).

Decreases in δ^{123}Sb during the early stages of adsorption of Sb(V) to goethite and illite indicate that complex transient isotope effects occur during surface complexation. The decrease of aqueous δ^{123}Sb within the first hours for the illite and goethite Sb(V) experiments suggest that the mechanism of Sb(V) adsorption includes some unusual aspect, as no similar trend is observed for Sb(III), Te(IV), or Te(VI). Different modes of complexation can produce variable isotopic fractionation as examined by Kashiwabara et al. (2017) for tungstate. For example, lower affinity, bidentate-binuclear complexes may form first relative to bidentate-mononuclear complexes resulting in variable isotopic fractionation over time. However, the difference in distortion between bidentate-binuclear and bidentate-mononuclear complexes is expected to be small (Kashiwabara et al., 2017), whereas the negative excursions we observed are significant (~ 0.2‰) and suggest a substantial distortion. Another explanation could arise from the presence of aqueous Sb chloride complexes. Łukaszczyk and Żyrnicki (2010) reported that Sb(V) formed $Sb(OH)_xCl_{(5-x)}{}^0{}_{(aq)}$ species in dilute solutions of HCl. This Sb chloride complex may be enriched in ^{121}Sb relative to $Sb(OH)_6^-$ due to the weaker bonding environment. These aqueous species could possibly adsorb less readily than $Sb(OH)_6^-$ due to weaker electrostatic attraction of the neutrally charged species, $Sb(OH)_xCl_{(5-x)}{}^0{}_{(aq)}$. The complexation of isotopically heavy $Sb(OH)_6^-$ would drive the aqueous $\delta^{123}Sb$ to lighter values initially and then increase once $Sb(OH)_xCl_{(5-x)}{}^0{}_{(aq)}$ adsorbs. Unfortunately, few studies exist that examine Sb(V) chloride species and we cannot confirm if Sb-Cl complexes are significant in our matrix. Accordingly, this scenario is speculative at present, but in general we note that aqueous speciation effects like the proposed one may lead to complex kinetic isotope effects.

Unlike the results for Sb(V) adsorption, aqueous $\delta^{130}Te$ increases monotonically until isotopic equilibrium is reached. For both Te(IV) and Te(VI), isotopic equilibrium is achieved only a few hours after chemical equilibrium. EXAFS spectra verify that no change in coordination geometry readily take place during Te adsorption to illite or goethite at circumneutral pH (Qin et al., 2017). Therefore, the lack of kinetic isotope effects prior to isotopic equilibrium is not surprising.

3.4.5 Effects of adsorbent and pH

As shown in previous studies with other elements, isotopic fractionation can be variable depending on the mineral adsorbent (Goldberg et al., 2009; Jemison et al., 2016; Xu et al., 2020). With the exception of Te(VI), there were no major sorbent-dependent differences in the observed Δ^{123}Sb or Δ^{130}Te. Therefore, it appears that isotopic fractionation is dominantly influenced by the formation of inner-sphere complexes and not by electrostatic attraction.

Evidence for inner-sphere complexation of Te and Sb to clay minerals has been observed in field settings and experiments at circumneutral pH and the results of these studies can suggest possible mechanisms of isotopic fractionation. Octahedrally-coordinated aluminum oxides or various Fe or Al hydroxide coatings are sites where inner-sphere complexation has been suggested to take place for other oxyanions, selenite and arsenate (Mohapatra et al., 2007; Peak et al., 2006). EXAFS spectra of Sb(V) and Sb(III) adsorption on kaolinite show both forming bidentate-binuclear corner-sharing and monodendate complexes on aluminum oxides at pH 5 (Ilgen and Trainor, 2012). While the chemical mechanism of adsorption has not been explored for Te, adsorption envelopes show very little variation in Te adsorption affinity from pH 3 through 10 indicating the prevalence of inner-sphere complexation (Qin et al., 2017). Indeed, Se(IV), which is somewhat chemically analogous to Te(IV), forms exclusively bidentate-binuclear complexes on montmorillonite, another 2:1 clay mineral (Peak et al., 2006). Therefore, like Sb, monodentate or bidentate adsorbed Te species are likely present. This does not preclude the existence of outer-sphere complexes though.

Adsorption behavior of Te and Sb to goethite is better studied. Te(IV), Te(VI), and Sb(III) are known to adsorb to goethite and other Fe-(oxy)hydroxides as inner-sphere complexes over a wide range of pH (Guo et al., 2014; Hein et al., 2003b; Leuz et al., 2006; Qin et al., 2017).

Sb(V) unequivocally forms predominantly inner-sphere complexes at pH <7, but both inner-sphere and outer-sphere complexes have been reported at higher pH (Leuz et al., 2006). During inner-sphere adsorption, both Sb(III) and Sb(V) form bidentate binuclear corner and edge-sharing complexes (Burton et al., 2020; Scheinost et al., 2006). The slightly smaller Δ^{123}Sb measured for illite could be due to the propensity of Sb species to form only corner-sharing bidentate complexes (Ilgen and Trainor, 2012). As the bond distances between the Fe-O and Sb-O octahedra are shorter for edge-sharing complexes, a greater degree of symmetry loss would be expected during the formation of these complexes, resulting in a larger Δ^{123}Sb for goethite.

Our results show very little difference isotopically between the two pH conditions examined here. Despite the adsorption affinity being very different for Sb(V) at pH 6 and 8 for illite and goethite, the fractionation factors did not vary within analytical uncertainty. A similar lack of pH dependence for isotopic fractionation has been noted for Se(IV) adsorption to Fe and Al oxides despite a larger range of pH being investigated (Xu et al., 2020). The isotopic fractionation of Ge, another oxyanion, also shows no variation with pH (Pokrovsky et al., 2014). As these studies suggest, the degree of surface protonation does not affect the isotopic fractionation produced. Instead, the physicochemical factors that influence ligand formation to the mineral surface matter.

As goethite and illite did not change structurally in the pH range examined here, Te and Sb modes of complexation were presumably similar at pH 6 and 8. While it has been proposed that outer-sphere complexes dominate at pH > 7 for Sb(V) adsorption to Al- and Fe-(oxy)hydroxides (Leuz et al., 2006), inner-sphere complexes must dominate at higher pH 8, as the presence of large amounts of outer-sphere complexes should mute any isotopic fractionation induced by inner-sphere coordination. Higher pH conditions than those examined in this study may show decreased Δ^{123}Sb as the proportion of outer-sphere complexes increase. In addition, in a more acidic pH range, Δ^{130}Te may be muted by increased electrostatic attraction and outer-sphere complexation between the positively charged $H_2TeO_3^+$ and negatively charged illite (Brookins, 1988). Such explorations are outside of the scope of this study and should be considered in future work.

3.4.6 Implications of Sb and Te isotopic fractionation

Elucidating Sb and Te biogeochemical transformations is central to understanding the fate and transport of these metalloids, as emerging contaminants and as economically valuable elements. Because adsorption to common minerals is a major immobilizing pathway, the magnitude of isotopic fractionation associated with this process has profound influence on global and local Te and Sb isotopic budgets. Like other non-traditional stable isotope systems (W, Mo, Se), adsorption produces a positive $\Delta_{(\text{aqueous-adsorbed})}$ for Te and Sb (Kashiwabara et al., 2017; Mitchell et al., 2013; Wasylenki et al., 2011; Xu et al., 2020). Transport of Te and Sb in oxic surficial environments is dominantly controlled by adsorption to Fe-(oxy)hydroxides and clays (Hayes and Ramos, 2019; Ilgen and Trainor, 2012; Qin et al., 2017; Scheinost et al., 2006). Given our results, dissolved Sb and Te in rivers and other waterways should be isotopically heavier than sediments or soils containing these mineral sorbents and this, in turn, would influence the Te or Sb isotopic composition of the oceans.

Adsorption and incorporation of Te into ferromanganese crusts has been proposed to be the largest sink of dissolved Te in the ocean. Kashiwabara et al. (2014a) determined that Te in crusts was dominantly incorporated as Te(VI) into ferrihydrite through co-precipitation. While we did not measure adsorption on ferrihydrite directly, the Δ^{130}Te of adsorption to goethite suggests that oxic ocean waters may be driven toward isotopically heavy compositions as a result of (1) adsorption and co-precipitation of Te(VI) on ferromanganese crusts, (2) particulate scavenging in the water column (Lee and Edmond, 1985), and (3) input of isotopically heavy rivers. The second and third processes may drive δ^{130}Te in sediments to isotopically heavy values as well. Indeed, (Wasserman and Johnson, 2020a) reported that the δ^{130}Te of a Pacific Ocean diagenetic ferromanganese nodule, Nod-P-1, was +0.50‰. To fully characterize Te isotope fractionating processes in this archive, further research is needed to measure Te isotopic fractionation during adsorption to Mn oxides and oxidation of Te(IV).

The δ^{123}Sb of modern seawater is likely influenced by similar processes, but on longer timescales as Sb is a quasi-conservative element. Rouxel et al. (2003) observed that North Atlantic seawater was approximately 0.20‰ heavier than pelagic clays, a range similar to the Δ^{123}Sb for adsorption to illite and goethite. Given this observation, the export of Sb to pelagic sediments via adsorption may control the modern marine Sb isotope budget. It is unclear how past seawater δ^{123}Sb varied under marine anoxia. Prior to the appearance of Fe oxides, seawater Sb isotopic variation could have been controlled by adsorption of $Sb(OH)_3$ to clays. However, the formation of Sb(III) sulfide species under Proterozoic euxinic conditions may also contribute to possible variations in Precambrian seawater δ^{123}Sb (Reinhard et al., 2013). Future examinations of δ^{123}Sb in modern and geologic records of seawater should focus on adsorption as an important sink of marine Sb.

In most systems, the fractionation factor measured at isotopic equilibrium can effectively be applied to interpret the Te and Sb isotopic budget. However, at shorter time-scales, Sb(V) adsorption to goethite may be influenced by the kinetic isotope effects observed in this study. Kinetic isotopic fractionation of Sb would be impactful in regimes where Fe-oxide dissolution and reprecipitation occurs on in less than a week, for example, at a fluctuating water table

(Yabusaki et al., 2017), In such a setting, the isotopic effects adsorption would be difficult to untangle from other reactions that produce kinetic isotope effects, like reduction. In addition, isotope effects of incorporation of Sb(V) into goethite due to Fe(II)-remineralization should be further examined, as this process is thought to be a major sink of Sb (Burton et al., 2020).

Given the known range of Te and Sb isotopic fractionation during reduction (ε^{130}Te ~-1.9 to -4.0‰; ε^{123}Sb ~-0.9 to -1.4‰) (Baesman et al., 2007; Mackinney, 2016; Smithers and Krouse, 1968), isotopic fractionation during adsorption of Te(VI) and Sb to common minerals should be taken into account and explored in further detail. The Δ^{123}Sb values obtained in this study are 20 to 40% of the magnitude of isotopic fractionation due to reduction (Mackinney, 2016; Rouxel et al., 2003). Te(VI) isotopic fractionation during adsorption is 20 to 35% of the magnitude of that produced during reduction (Baesman et al., 2007; Smithers and Krouse, 1968). Hayes and Ramos (2019) and others have noted that Te(VI) is the most abundant species in mine tailings and related sediments due to its thermodynamic stability in oxic environments. In surficial weathering environments, isotopic fractionation due to adsorption of Te(VI) onto goethite will drive waters and weathering products heavier as these elements undergo multiple cycles of adsorption. However, in systems with fluctuating redox conditions, where Sb or Te oxyanions may be partially adsorbed or reduced, contributions from both fractionating processes may be present. In this case, adsorption can lead to an overestimation of the extent of Sb(V) or Te(VI) reduction. In addition, the impact of adsorption would be most apparent at lower magnitudes of reduction when less isotopic fractionation has occurred. Disentangling redox and adsorption processes is less problematic at larger extents of reduction.

3.5 Conclusions

This study reports the first evidence of isotopic fractionation for adsorption of Te and Sb onto mineral surfaces. Inner-sphere complexation causes light isotopes to partition into the adsorbed species on goethite or illite. This is due to the distortion of the Te-O or Sb-O bonds in the adsorbed species, relative to aqueous species. No differences were observed between Δ^{123}Sb(III) and Δ^{123}Sb(V), likely due to similar mechanisms of complexation. However, compared to Sb(III), Sb(V) isotopic exchange during adsorption of goethite was very slow, possibly due to recrystallization of the sorbent. Δ^{130}Te measured during adsorption of Te(VI) to goethite produced the largest isotopic fractionation for all conditions examined, possibly due to the bidentate mode of complexation of Te(VI) to goethite.

The isotopic fractionation during adsorption of Te(VI) or Sb most likely contributes significantly to natural isotopic variation observed in oxic environments. Care must be taken, though, to disentangle adsorption from competing processes, like reduction, as both processes fractionate the isotopes in a similar manner and magnitude. As attenuation of Te and Sb in oxic environments is primarily controlled by the presence of Fe-(oxy)hydroxides, these results have major implications for the global Te and Sb isotope budget and the applications of these isotope systems to trace elemental mobility on a local scale.

3.6 Tables and Figures

Table 3.1. Initial solid to liquid ratio for each condition tested.

Ratio of goethite mass to liquid volume (g L^{-1})

Te(IV)		**Te(VI)**		**Sb(III)**		**Sb(V)**	
pH 6	**pH 8**	**pH 6**	**pH 8**	**pH 6**	**pH 8**	**pH 6**	**pH 8**
0.2	0.2	0.5	0.5	0.2	0.2	0.2	0.5

Ratio of illite mass to liquid volume (g L^{-1})

Te(IV)		**Te(VI)**		**Sb(III)**		**Sb(V)**	
pH 6	**pH 8**	**pH 6**	**pH 8**	**pH 6**	**pH 8**	**pH 6**	**pH 8**
3	3	4	4	6	6	7	7

Table 3.2. Magnitude of isotopic equilibrium fractionation for the multi-stage, high precision experiments.

$\Delta_{aq\text{-}ads}$ (‰, 2σ)

	Illite		**Goethite**	
pH	**6.0**	**8.0**	**6.0**	**8.0**
Sb(III)	0.22 ± 0.07	0.23 ± 0.13	0.31 ± 0.11	0.32 ± 0.09
Sb(V)	0.25 ± 0.12	0.28 ± 0.03	0.39 ± 0.08	0.34 ± 0.08
Te(IV)	0.25 ± 0.08	0.24 ± 0.05	0.20 ± 0.07	0.12 ± 0.03
Te(VI)	0.32 ± 0.05	0.30 ± 0.08	0.68 ± 0.09	0.64 ± 0.12

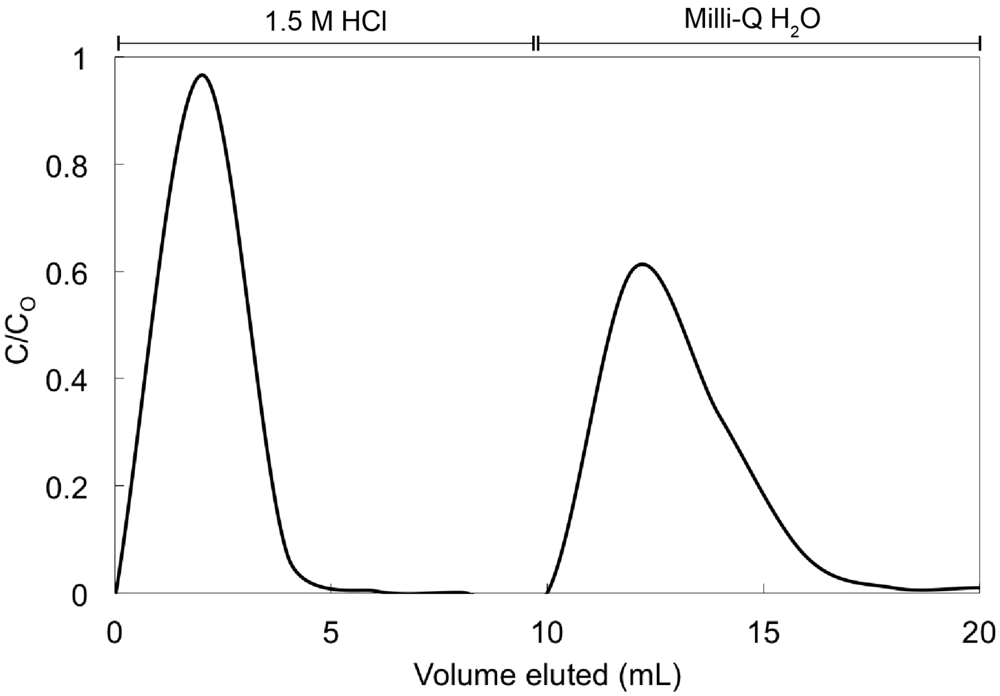

Figure 3.1. Elution of Sb(V) (first peak) and Sb(III) (second peak) species with a sample load of 1.0 µg Sb(V) and 1.0 µg Sb(III). Brackets above the plot indicate the volume of 1.5 M HCl and Milli-Q H_2O in the procedure.

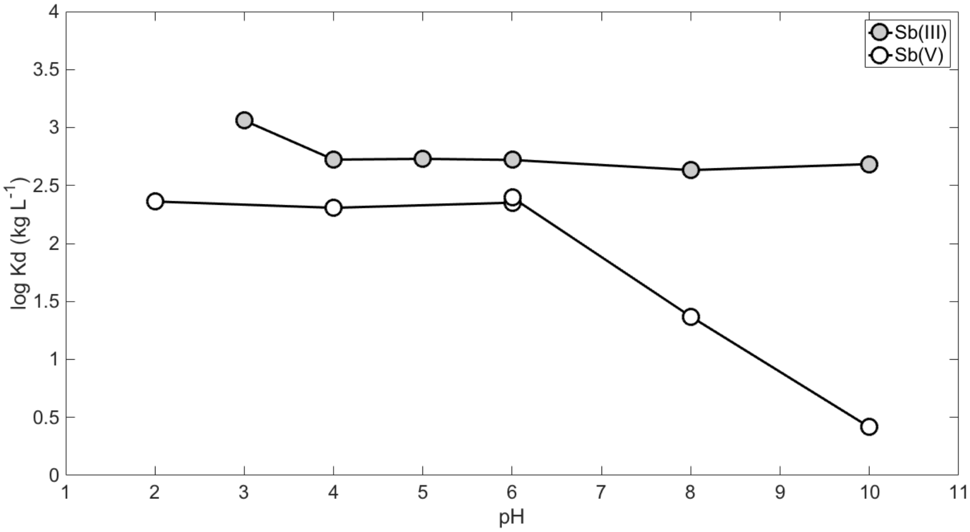

Figure 3.2. Adsorption of Sb(V) and Sb(III) to illite over a range of pH. Log(Kd) is the log of the ratio of the concentration of Sb in solution (μg L^{-1}) to the mass of Sb adsorbed per kg of illite (μg kg^{-1}) at equilibrium.

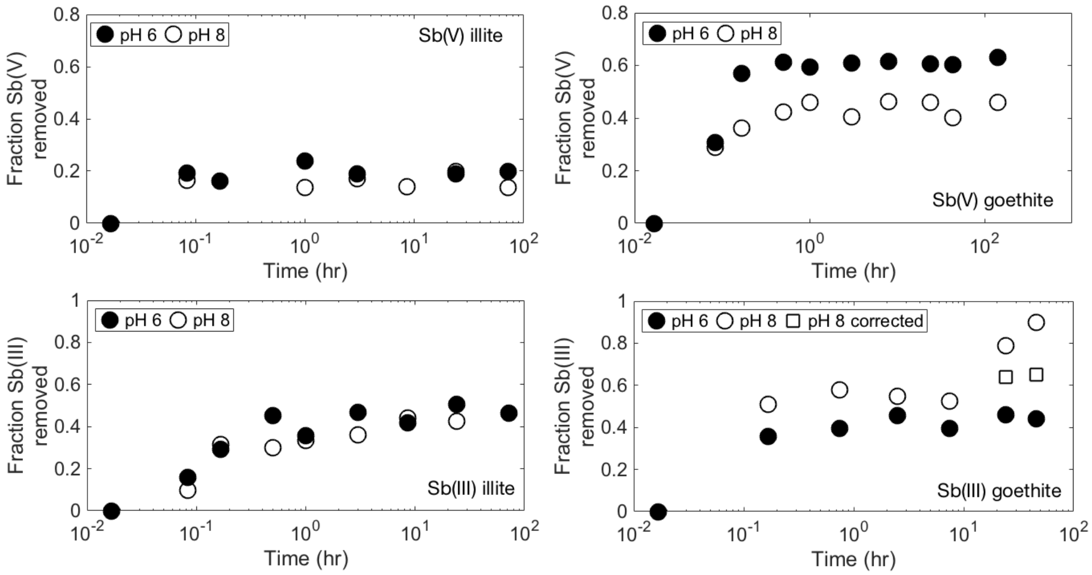

Figure 3.3. Fraction of total Sb adsorbed over after addition of 0.02 g goethite or 0.1 g illite for both pH conditions. Open squares in the Sb(III) goethite experiment show corrected fraction of Sb(V) in the pH 8 condition. Sb(V) remained below the limit of detection in the other Sb(III) conditions.

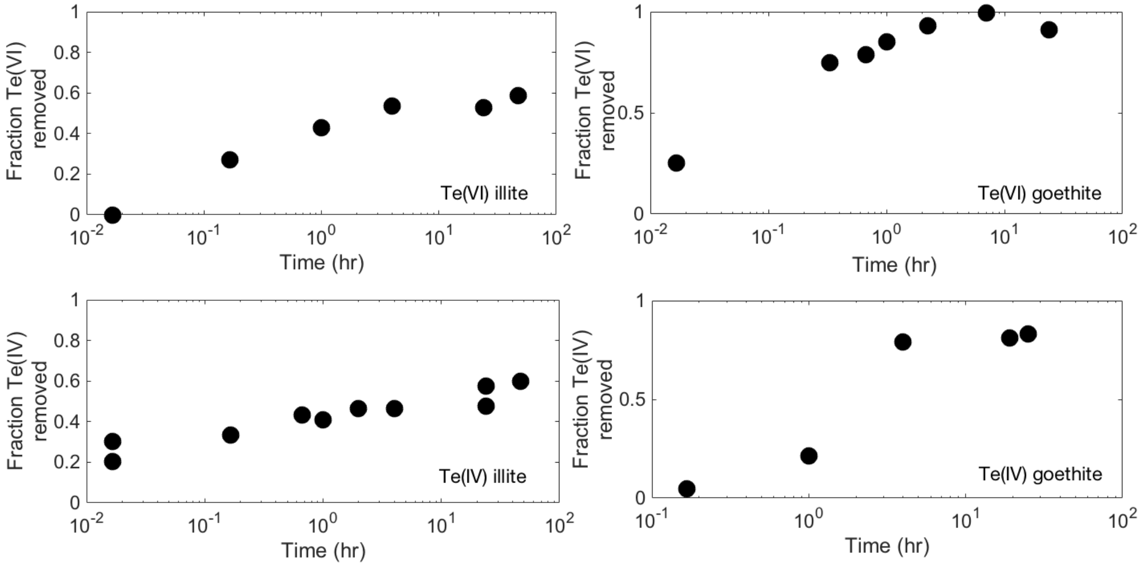

Figure 3.4. Fraction of total Te adsorbed over time after addition of goethite or illite as shown in Te(VI) to illite, Te(VI) to goethite, Te(IV) to illite, and Te(IV) to illite. The solution matrix was adjusted to pH 6.

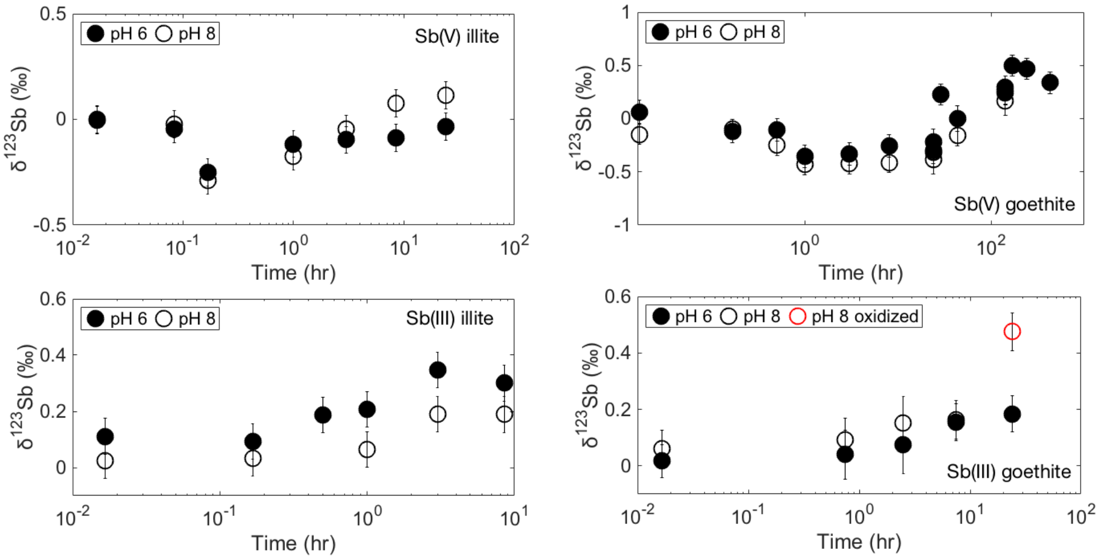

Figure 3.5. δ^{123}Sb of dissolved Sb over the course of the kinetic experiments. The red circle in the Sb(III) goethite plot is affected by oxidation of Sb(III). Error bars denote twice the standard deviation for 3 pairs of triplicate measurements made during each analytical session.

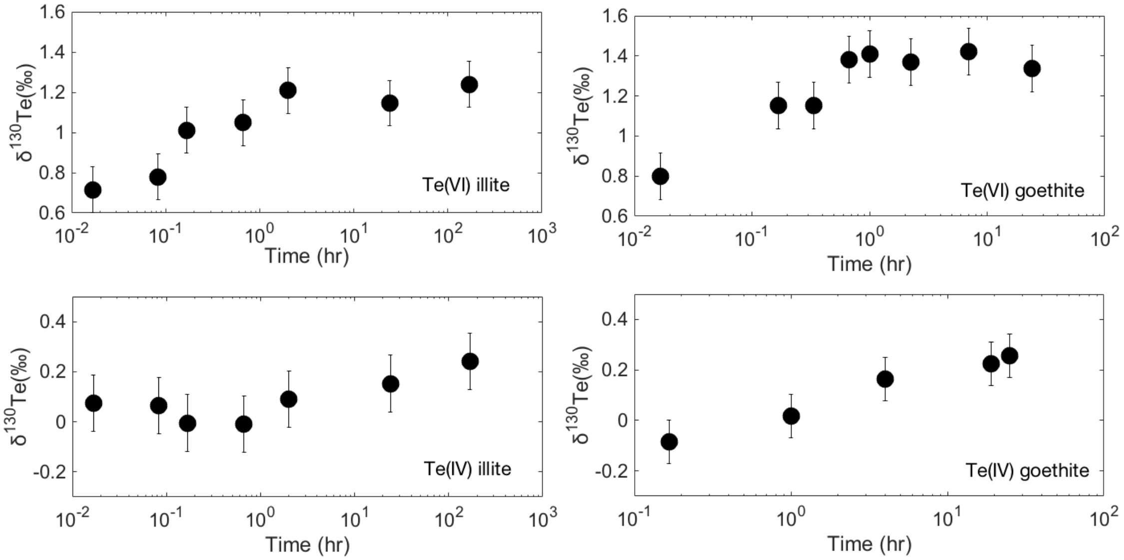

Figure 3.6. δ^{130}Te of dissolved Te as a function of time at pH 6. Error bars denote twice the standard deviation for 3 pairs of duplicate measurements made during each analytical session.

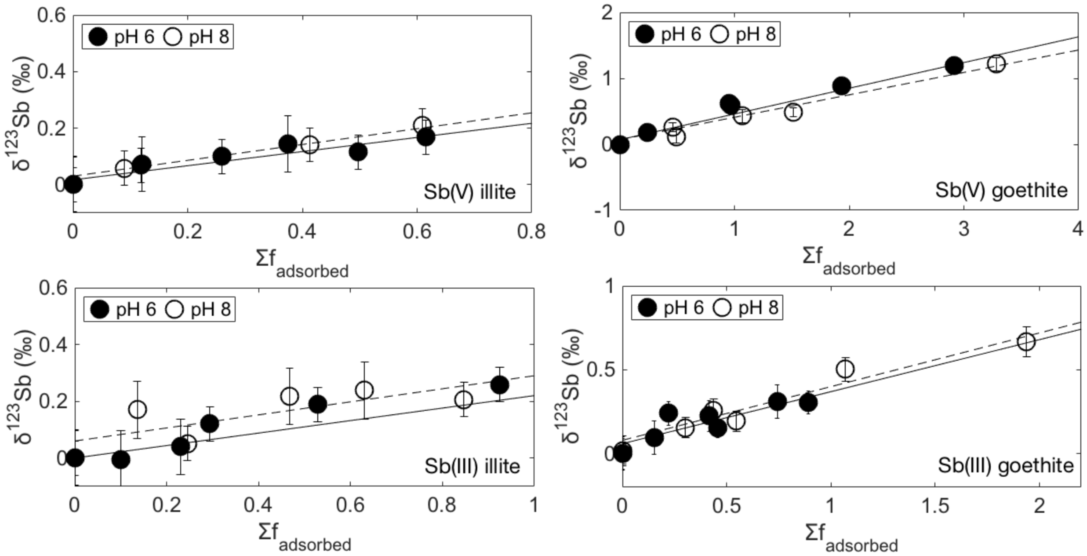

Figure 3.7. δ^{123}Sb of dissolved Sb over the cumulative fraction of Sb adsorbed. Error bars represent twice the uncertainty for four pairs of triplicates in an analytical session. Solid and dashed black lines show the slopes of the linear regression for pH 6 and pH 8 conditions, respectively.

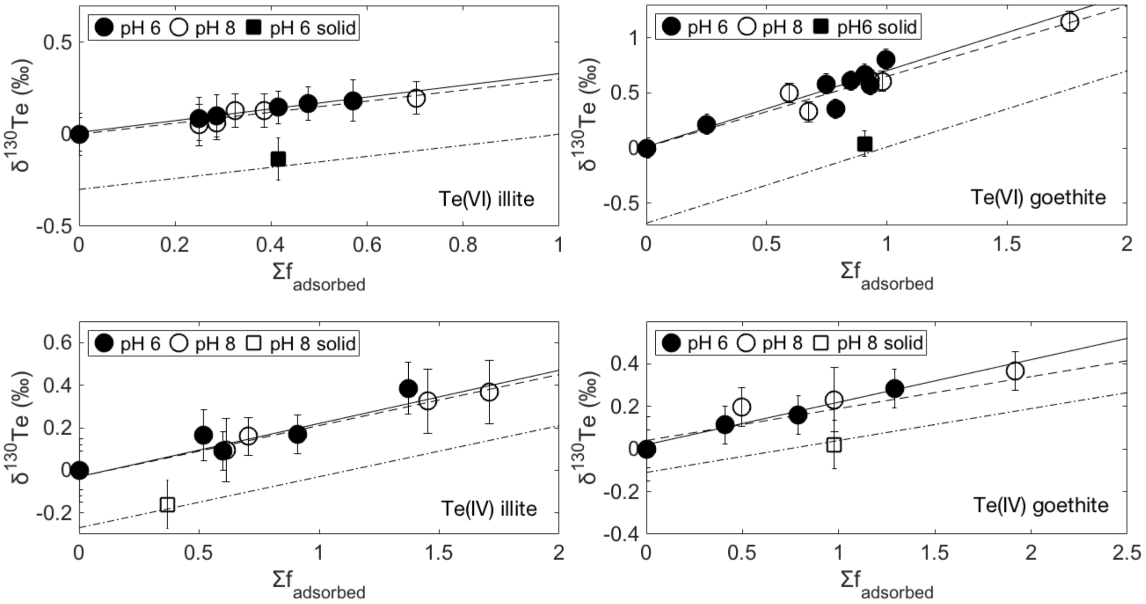

Figure 3.8**.** δ^{130}Te of dissolved Te versus the cumulative fraction of Te adsorbed over multiple cycles of sorbent addition. Error bars represent twice the uncertainty for three pairs of duplicates for each analytical session. Solid and dashed black lines show the slopes of the linear regression for aqueous δ^{130}Te at pH 6 and pH 8, respectively. The dashed (-:-:-) line is the predicted model of the adsorbed δ^{130}Te as calculated based on the aqueous δ^{130}Te measurements.

3.7 References

Ashley, P.M., Graham, B.P., Tighe, M.K. and Wolfenden, B.J. (2007) Antimony and arsenic dispersion in the Macleay River catchment, New South Wales: a study of the environmental geochemical consequences. Australian Journal of Earth Sciences 54, 83-103.

Baesman, S.M., Bullen, T.D., Dewald, J., Zhang, D., Curran, S., Islam, F.S., Beveridge, T.J. and Oremland, R.S. (2007) Formation of Tellurium Nanocrystals during Anaerobic Growth of Bacteria That Use Te Oxyanions as Respiratory Electron Acceptors. Appl. Environ. Microbiol. 73, 2135-2143.

Balistrieri, L.S. and Chao, T.T. (1987) Selenium Adsorption by Goethite. Soil Science Society of America Journal 51, 1145-1151.

Barling, J. and Anbar, A.D. (2004) Molybdenum isotope fractionation during adsorption by manganese oxides. Earth and Planetary Science Letters 217, 315-329.

Brennecka, G.A., Borg, L.E., Romaniello, S.J., Souders, A.K., Shollenberger, Q.R., Marks, N.E. and Wadhwa, M. (2017) A renewed search for short-lived 126Sn in the early Solar System: Hydride generation MC-ICPMS for high sensitivity Te isotopic analysis. Geochimica et Cosmochimica Acta 201, 331-344.

Brennecka, G.A., Wasylenki, L.E., Bargar, J.R., Weyer, S. and Anbar, A.D. (2011) Uranium Isotope Fractionation during Adsorption to Mn-Oxyhydroxides. Environmental Science & Technology 45, 1370-1375.

Brookins, D.G. (1988) Eh-pH diagrams for geochemistry. Springer.

Brown, S.T., Basu, A., Ding, X., Christensen, J.N. and DePaolo, D.J. (2018) Uranium isotope fractionation by abiotic reductive precipitation. Proceedings of the National Academy of Sciences 115, 8688.

Brüske, A., Weyer, S., Zhao, M.Y., Planavsky, N.J., Wegwerth, A., Neubert, N., Dellwig, O., Lau, K.V. and Lyons, T.W. (2020) Correlated molybdenum and uranium isotope signatures in modern anoxic sediments: Implications for their use as paleo-redox proxy. Geochimica et Cosmochimica Acta 270, 449-474.

Bryan, A.L., Dong, S., Wilkes, E.B. and Wasylenki, L.E. (2015) Zinc isotope fractionation during adsorption onto Mn oxyhydroxide at low and high ionic strength. Geochimica et Cosmochimica Acta 157, 182-197.

Burton, E.D., Hockmann, K. and Karimian, N. (2020) Antimony Sorption to Goethite: Effects of Fe(II)-Catalyzed Recrystallization. ACS Earth and Space Chemistry 4, 476-487.

Chen, X., Romaniello, S.J. and Anbar, A.D. (2017) Uranium isotope fractionation induced by aqueous speciation: Implications for U isotopes in marine CaCO3 as a paleoredox proxy. Geochimica et Cosmochimica Acta 215, 162-172.

Cooper, R.G. and Harrison, A.P. (2009) The exposure to and health effects of antimony. Indian Journal of Occupational and Environmental Medicine 13, 3-10.

Dixit, S. and Hering, J.G. (2003) Comparison of Arsenic(V) and Arsenic(III) Sorption onto Iron Oxide Minerals: Implications for Arsenic Mobility. Environmental Science & Technology 37, 4182-4189.

Dzombak, D.A.M., F.M.M. (1990) Surface Complexation Modeling-Hydrous Ferrix Oxide. John Wiley, New York.

Essington, M., Stewart, M. and Vergeer, K. (2017) Adsorption of Antimonate by Kaolinite. Soil Science Society of America Journal 81, 514-525.

Fehr, M.A., Hammond, S.J. and Parkinson, I.J. (2018) Tellurium stable isotope fractionation in chondritic meteorites and some terrestrial samples. Geochimica et Cosmochimica Acta 222, 17-33.

Fernandez, N.M., Zhang, X. and Druhan, J.L. (2019) Silicon isotopic re-equilibration during amorphous silica precipitation and implications for isotopic signatures in geochemical proxies. Geochimica et Cosmochimica Acta 262, 104-127.

Filella, M., Belzile, N. and Chen, Y.-W. (2002) Antimony in the environment: a review focused on natural waters: I. Occurrence. Earth-Science Reviews 57, 125-176.

Filella, M., Williams, P.A. and Belzile, N. (2009) Antimony in the environment: knowns and unknowns. Environmental Chemistry 6, 95-105.

Fukami, Y., Kimura, J.-I. and Suzuki, K. (2018) Precise isotope analysis of tellurium by inductively coupled plasma mass spectrometry using a double spike method. Journal of Analytical Atomic Spectrometry 33, 1233-1242.

Goldberg, T., Archer, C., Vance, D. and Poulton, S.W. (2009) Mo isotope fractionation during adsorption to Fe (oxyhydr)oxides. Geochimica et Cosmochimica Acta 73, 6502-6516.

Guo, X., Wu, Z., He, M., Meng, X., Jin, X., Qiu, N. and Zhang, J. (2014) Adsorption of antimony onto iron oxyhydroxides: Adsorption behavior and surface structure. Journal of Hazardous Materials 276, 339-345.

Hayes, S.M. and Ramos, N.A. (2019) Surficial geochemistry and bioaccessibility of tellurium in semiarid mine tailings. Environmental Chemistry 16, 251-265.

Hein, J.R., Koschinsky, A. and Halliday, A.N. (2003a) Global occurrence of tellurium-rich ferromanganese crusts and a model for the enrichment of tellurium. Geochimica et Cosmochimica Acta 67, 1117-1127.

Hein, J.R., Koschinsky, A. and Halliday, A.N. (2003b) Global occurrence of tellurium-rich ferromanganese crusts and a model for the enrichment of tellurium. Geochimica et Cosmochimica Acta 67, 11.

Hussain, S.A., Demirci, Ş. and Özbayoğlu, G. (1996) Zeta Potential Measurements on Three Clays from Turkey and Effects of Clays on Coal Flotation. Journal of Colloid and Interface Science 184, 535-541.

Ilgen, A.G. and Trainor, T.P. (2012) Sb(III) and Sb(V) Sorption onto Al-Rich Phases: Hydrous Al Oxide and the Clay Minerals Kaolinite KGa-1b and Oxidized and Reduced Nontronite NAu-1. Environ. Sci. Technol. 46, 843-851.

Jemison, N.E., Bizjack, M.T., Johnson, T.M. and Druhan, J.L. (2020) Influence of physical and chemical hydrology on bioremediation of a U-contaminated aquifer informed by reactive transport modeling incorporating 238U/235U ratios. Geochimica et Cosmochimica Acta 269, 303-328.

Jemison, N.E., Johnson, T.M., Shiel, A.E. and Lundstrom, C.C. (2016) Uranium Isotopic Fractionation Induced by U(VI) Adsorption onto Common Aquifer Minerals. Environmental Science & Technology 50, 12232-12240.

Kashiwabara, T., Kubo, S., Tanaka, M., Senda, R., Iizuka, T., Tanimizu, M. and Takahashi, Y. (2017) Stable isotope fractionation of tungsten during adsorption on Fe and Mn (oxyhydr)oxides. Geochimica et Cosmochimica Acta 204, 52-67.

Kashiwabara, T., Oishi, Y., Sakaguchi, A., Sugiyama, T., Usui, A. and Takahashi, Y. (2014) Chemical processes for the extreme enrichment of tellurium into marine ferromanganese oxides. Geochimica et Cosmochimica Acta 131, 150-163.

Kong, L., He, M. and Hu, X. (2016) Rapid photooxidation of Sb(III) in the presence of different Fe(III) species. Geochimica et Cosmochimica Acta 180, 214-226.

Lee, D.S. and Edmond, J.M. (1985) Tellurium species in seawater. Nature 313, 782-785.
Leuz, A.-K. and Johnson, C.A. (2005) Oxidation of Sb(III) to Sb(V) by O2 and H2O2 in aqueous solutions. Geochimica et Cosmochimica Acta 69, 1165-1172.

Leuz, A.-K., Mönch, H. and Johnson, C.A. (2006) Sorption of Sb(III) and Sb(V) to Goethite: Influence on Sb(III) Oxidation and Mobilization. Environmental Science & Technology 40, 7277-7282.

Łukaszczyk, L. and Żyrnicki, W. (2010) Speciation analysis of Sb(III) and Sb(V) in antileishmaniotic drug using Dowex 1×4 resin from hydrochloric acid solution. Journal of Pharmaceutical and Biomedical Analysis 52, 747-751.

Mackinney, J. (2016) Antimony isotopes as indicators of redox reactions in aqueous systems: fractionation during Sb(V) reduction by sulfide and isotope exchange kinetics between dissolved Sb(III) and Sb(V), IDEALS.

Mitchell, K., Couture, R.-M., Johnson, T.M., Mason, P.R.D. and Van Cappellen, P. (2013) Selenium sorption and isotope fractionation: Iron(III) oxides versus iron(II) sulfides. Chemical Geology 342, 21-28.

Mitchell, K., Mason, P.R.D., Van Cappellen, P., Johnson, T.M., Gill, B.C., Owens, J.D., Diaz, J., Ingall, E.D., Reichart, G.-J. and Lyons, T.W. (2012) Selenium as paleo-oceanographic proxy: A first assessment. Geochimica et Cosmochimica Acta 89, 302-317.

Mitsunobu, S., Takahashi, Y., Terada, Y. and Sakata, M. (2010) Antimony(V) Incorporation into Synthetic Ferrihydrite, Goethite, and Natural Iron Oxyhydroxides. Environ. Sci. Technol. 44, 3712-3718.

Mohapatra, D., Mishra, D., Chaudhury, G.R. and Das, R.P. (2007) Arsenic adsorption mechanism on clay minerals and its dependence on temperature. Korean Journal of Chemical Engineering 24, 426-430.

Nielsen, S.G., Wasylenki, L.E., Rehkämper, M., Peacock, C.L., Xue, Z. and Moon, E.M. (2013) Towards an understanding of thallium isotope fractionation during adsorption to manganese oxides. Geochimica et Cosmochimica Acta 117, 252-265.

Peak, D., Saha, U.K. and Huang, P.M. (2006) Selenite Adsorption Mechanisms on Pure and Coated Montmorillonite: An EXAFS and XANES Spectroscopic Study. Soil Science Society of America Journal 70, 192-203.

Perez-D'Gregorio, R.E., Miller, R.K. and Baggs, R.B. (1988) Maternal toxicity and teratogenicity of tellurium dioxide in the wistar rat: Relationship to pair-feeding. Reproductive Toxicology 2, 55-61.

Pokrovsky, O.S., Galy, A., Schott, J., Pokrovski, G.S. and Mantoura, S. (2014) Germanium isotope fractionation during Ge adsorption on goethite and its coprecipitation with Fe oxy(hydr)oxides. Geochimica et Cosmochimica Acta 131, 138-149.

Qi, P. and Pichler, T. (2017) Competitive adsorption of As(III), As(V), Sb(III) and Sb(V) onto ferrihydrite in multi-component systems: Implications for mobility and distribution. Journal of Hazardous Materials 330, 142-148.

Qin, H.-B., Takeichi, Y., Nitani, H., Terada, Y. and Takahashi, Y. (2017) Tellurium Distribution and Speciation in Contaminated Soils from Abandoned Mine Tailings: Comparison with Selenium. Environmental Science & Technology 51, 6027-6035.

Quentel, F., Filella, M., Elleouet, C. and Madec, C.-L. (2006) Sb(III) oxidation by iodate in seawater: A cautionary tale. Science of The Total Environment 355, 259-263.

Reinhard, C.T., Planavsky, N.J., Robbins, L.J., Partin, C.A., Gill, B.C., Lalonde, S.V., Bekker, A., Konhauser, K.O. and Lyons, T.W. (2013) Proterozoic ocean redox and biogeochemical stasis. Proceedings of the National Academy of Sciences 110, 5357.

Resongles, E., Freydier, R., Casiot, C., Viers, J., Chmeleff, J. and Elbaz-Poulichet, F. (2015) Antimony isotopic composition in river waters affected by ancient mining activity. Talanta 144, 851-861.

Rouxel, O., Ludden, J. and Fouquet, Y. (2003) Antimony isotope variations in natural systems and implications for their use as geochemical tracers. Chemical Geology 200, 25-40.

Scheinost, A.C., Rossberg, A., Vantelon, D., Xifra, I., Kretzschmar, R., Leuz, A.-K., Funke, H. and Johnson, C.A. (2006) Quantitative antimony speciation in shooting-range soils by EXAFS spectroscopy. Geochimica et Cosmochimica Acta 70, 3299-3312.

Shiel, A.E., Johnson, T.M., Lundstrom, C.C., Laubach, P.G., Long, P.E. and Williams, K.H. (2016) Reactive transport of uranium in a groundwater bioreduction study: Insights from high-temporal resolution 238U/235U data. Geochimica et Cosmochimica Acta 187, 218-236.

Smithers, R.M. and Krouse, H.R. (1968) Tellurium isotope fractionation study. Can. J. Chem. 46, 583-591.

Stüeken, E.E., Buick, R., Bekker, A., Catling, D., Foriel, J., Guy, B.M., Kah, L.C., Machel, H.G., Montañez, I.P. and Poulton, S.W. (2015) The evolution of the global selenium cycle: Secular trends in Se isotopes and abundances. Geochimica et Cosmochimica Acta 162, 109-125.

Stylo, M., Neubert, N., Wang, Y., Monga, N., Romaniello, S.J., Weyer, S. and Bernier-Latmani, R. (2015) Uranium isotopes fingerprint biotic reduction. Proceedings of the National Academy of Sciences 112, 5619.

Tella, M. and Pokrovski, G.S. (2009) Antimony(III) complexing with O-bearing organic ligands in aqueous solution: An X-ray absorption fine structure spectroscopy and solubility study. Geochimica et Cosmochimica Acta 73, 268-290.

Venema, P., Hiemstra, T., Weidler, P.G. and van Riemsdijk, W.H. (1998) Intrinsic Proton Affinity of Reactive Surface Groups of Metal (Hydr)oxides: Application to Iron (Hydr)oxides. Journal of Colloid and Interface Science 198, 282-295.

Wang, X., He, M., Xi, J. and Lu, X. (2011) Antimony distribution and mobility in rivers around the world's largest antimony mine of Xikuangshan, Hunan Province, China. Microchemical Journal 97, 4-11.

Wasserman, N.L. and Johnson, T.M. (2020) Measurements of mass-dependent Te isotopic variation by hydride generation MC-ICP-MS. J. Anal. At. Spectrom. 35, 307-319.

Wasserman, N.M., J.; Johnson, T.M; Kulp, T (2018) Development of Sb Isotopes as Tracers of Sb Mobility in the Environment. Goldschmidt Abstracts 2018, 2743.

Wasylenki, L.E., Weeks, C.L., Bargar, J.R., Spiro, T.G., Hein, J.R. and Anbar, A.D. (2011) The molecular mechanism of Mo isotope fractionation during adsorption to birnessite. Geochimica et Cosmochimica Acta 75, 5019-5031.

Westerhoff, P., Prapaipong, P., Shock, E. and Hillaireau, A. (2008) Antimony leaching from polyethylene terephthalate (PET) plastic used for bottled drinking water. Water Research 42, 551-556.

Wiklund, J.A., Kirk, J.L., Muir, D.C.G., Carrier, J., Gleason, A., Yang, F., Evans, M. and Keating, J. (2018) Widespread Atmospheric Tellurium Contamination in Industrial and Remote Regions of Canada. Environmental Science & Technology 52, 6137-6145.

Xi, J. and Zhang, S. (2017) Adsorption and desorption of Sb(III) on goethite. IOP Conference Series: Earth and Environmental Science 100, 012145.

Xu, W., Zhu, J.-M., Johnson, T.M., Wang, X., Lin, Z.-Q., Tan, D. and Qin, H. (2020) Selenium isotope fractionation during adsorption by Fe, Mn and Al oxides. Geochimica et Cosmochimica Acta 272, 121-136.

Yabusaki, S.B., Wilkins, M.J., Fang, Y., Williams, K.H., Arora, B., Bargar, J., Beller, H.R., Bouskill, N.J., Brodie, E.L., Christensen, J.N., Conrad, M.E., Danczak, R.E., King, E., Soltanian, M.R., Spycher, N.F., Steefel, C.I., Tokunaga, T.K., Versteeg, R., Waichler, S.R. and Wainwright, H.M. (2017) Water Table Dynamics and Biogeochemical Cycling in a Shallow, Variably-Saturated Floodplain. Environ. Sci. Technol. 51, 3307-3317.

Ylagan, R.F., Altaner, S.P. and Pozzuoli, A. (2000) Reaction Mechanisms of Smectite Illitization Associated with Hydrothermal Alteration from Ponza Island, Italy. Clays and Clay Minerals 48, 610-631.

Zhang, L., Zhang, M., Guo, X., Liu, X., Kang, P. and Chen, X. (2010) Sorption characteristics and separation of tellurium ions from aqueous solutions using nano-TiO2. Talanta 83, 344-350.

Zweibel, K. (2010) The Impact of Tellurium Supply on Cadmium Telluride Photovoltaics. Science 328, 699-701.

CHAPTER 4: SELENIUM ISOTOPE SHIFTS DURING THE OXIDATION OF SELENIDE-BEARING MINERALS

Abstract

Mobilization of the toxic contaminant, selenium (Se), from rock and soil is largely driven by oxidation, where selenides, elemental Se, and organically-bound Se are more insoluble than Se(IV) and Se(VI) oxyanions. In Se-impacted ecosystems, isotopic fractionation of Se ($^{82}Se/^{76}Se$) can be used to track attenuating processes, like abiotic and biological reduction of Se(IV) and Se(VI). Isotope effects associated with oxidative dissolution of Se-bearing minerals have not been studied, but could be significant during incongruent dissolution.

We examined the isotopic evolution of dissolved Se(IV) and Se(VI) during the oxidation of ferroselite ($FeSe_2$) and berzelianite (Cu_2Se) with H_2O_2 and O_2. In all experiments, Se(VI) produced by oxidation was isotopically heavy relative to the starting mineral composition. This isotopic shift arises from oxidation of Se(IV), reduction of oxidized Se by mineral phases, and/or isotopic exchange between Se(IV) and Se(VI). At lower concentrations of H_2O_2, isotopic fractionation associated with reduction of Se(IV) to Se(0) on ferroselite is apparent. At higher concentrations of H_2O_2, this effect is diluted by a higher flux of Se(IV) created by more rapid mineral oxidation and/or diminished reduction rate. As Se(VI) is more mobile than Se(IV) in oxygenated environments, the results of this study suggest that isotopically heavy Se(VI) observed in previous studies is to be expected in most environments when oxidative dissolution of Se-bearing minerals occurs.

4.1 Introduction

Selenium (Se) is a metalloid incorporated into seleno-proteins, which help maintain redox homeostasis and thyroid hormone metabolism in humans and animals (Arthur et al., 1992; Cox et al., 2016; Labunskyy et al., 2014). Ingestion of higher dosages of Se by humans can lead to selenosis, a condition with neurological, dermal, and cardiovascular complications (Lenz and Lens, 2009). Therefore, the US EPA drinking water maximum contaminant level is 50 ng mL^{-1} (EPA, 2018). Bioaccumulation of Se on an ecological level is a more prevalent issue. High levels of replacement of cysteine and methionine by selenocysteine and selenomethionine can disrupt protein function and result in lethal concentrations in organisms at higher trophic levels (fish, waterfowls, amphibians) (Luoma and Presser, 2009; Ohlendorf, 1989; Ohlendorf et al., 1990). In 2016, the EPA established that in lotic and lentic waters average Se must not exceed 1.5 and 3 ng mL^{-1}, respectively (EPA, 2018).

In Western North America, seleniferous marine shales (e.g. Mancos Shale, Colorado) are the source of elevated Se in watersheds (Kulp and Pratt, 2004; Presser et al., 2004; Presser and Swain, 1990; Presser et al., 1994; Trelease, 1950). Oxidative weathering of these formations occurs naturally, but can be exacerbated by irrigation or excavation during mining (Lemly, 2004; Stillings, 2010). In these systems, Se mobility is primarily controlled by oxidation state, where Se(VI) and Se(IV) form soluble, mobile oxyanions (SeO_4^{2-}, $HSeO_3^-$, SeO_3^{2-}) in oxygenated waters. The more reduced forms, Se(0) and Se(-II), meanwhile, exist as insoluble phases in low-temperature environments, or as organically-complexed Se. Abiotic and biological reduction of Se(IV) and Se(VI) in surface and groundwaters draining these formations are important processes controlling Se bioavailability and environmental impact. It is, therefore, necessary to quantify Se oxyanion microbial or abiotic reduction in order to assess the long-term impact of this contaminant on the local ecosystems.

Selenium stable isotopic fractionation (^{82}Se/^{76}Se) can be used to track reduction and other biogeochemical transformations of Se (Johnson, 2004). Isotopic fractionation factors, or the difference between the reactant and instantaneous product ($\varepsilon^{82/76}$Se) varies for Se(VI) and Se(IV) abiotic or biological reduction. Microbial or abiotic reduction of Se(VI) to Se(IV) produces $\varepsilon^{82/76}$Se of -3.90 to -11.04‰ while $\varepsilon^{82/76}$Se of Se(IV) reduction to Se(0) ranged from -8.25 to -12.60‰ (Ellis et al., 2003; Herbel et al., 2000; Johnson and Bullen, 2003; Johnson et al., 1999). Methylation and volatilization of Se results in a similar magnitude $\varepsilon^{82/76}$Se ~ -4.5‰ (Schilling et al., 2011). Non-redox processes, like adsorption to Fe-oxides and Mn-oxides, can induce small isotopic shifts between the adsorbed and aqueous Se species of up to 1.0‰ and 1.24‰, respectively (Johnson et al., 1999; Mitchell et al., 2013; Xu et al., 2020). Numerous studies have used this framework to elucidate Se fate and transport in natural systems (Basu et al., 2016; Clark and Johnson, 2010; Schilling et al., 2015).

Isotopic fractionation during oxidative dissolution of Se has been observed to be minimal in a very small number of experiments. Two laboratory studies reported $\varepsilon^{82/76}$Se < 1.0‰ during the oxic incubation of a soil slurry and oxidation of Se(IV) by a very basic solution with 30% H_2O_2 (Johnson, 2004; Johnson et al., 1999). However, isotopic fractionation in the first experiment may have been muted by competing adsorption and reduction reactions, and the conditions in the second experiment are not naturally relevant. If significant isotope shifts occur during the release of Se oxyanions from rocks and soils, variations in $\delta^{82/76}$Se of waters may not exclusively indicate reduction or adsorption. No research has addressed potential isotope effects during oxidative dissolution of selenide-bearing minerals using environmentally relevant conditions.

Here, we present results of experiments that measured Se isotopic fractionation during the oxidative dissolution of two selenide-bearing minerals, berzelianite (Cu_2Se) and ferroselite ($FeSe_2$) by H_2O_2 and, in one experiment with ferroselite, by O_2. Hydrogen peroxide is an environmentally relevant oxidant of iron sulfides and presumably, iron selenides (Lefticariu et al., 2006; Schoonen et al., 2010). Indeed, H_2O_2 production can be self-catalyzed by pyrite and O_2 or water through surface-catalyzed reactions with Fe^{2+} and Fe^{3+} (Borda et al., 2001; Descostes et al., 2004; Gil-Lozano et al., 2017; Lowson, 1982). In O_2-free solutions, the oxidation of surface bound Fe(II) will impose a redox gradient from the reduced disulfide to the oxidized surface, causing bound H_2O or O_2 to disassociate into hydroxyl radicals (Ma and Lin, 2013). Subsequent recombination with other radicals or reactions with Fe^{2+} will form H_2O_2. In oxygenated waters, H_2O_2 is an intermediate in the electron transfer from pyrite to dissolved O_2 and increases the kinetics of pyrite oxidation (Schoonen et al., 2010). The experiments conducted in this study represent naturally relevant reactions occurring during the oxidative weathering of shales and the results presented here can inform future Se isotope studies in such environments.

4.2 Materials and Methods

Berzelianite (Harz, Germany) and ferroselite (Temple Mountain, USA) mineral specimens were obtained from the University of Utrecht (Netherlands). The berzelianite was pulverized and homogenized with a mortar and pestle, and sieved to a grain size of 150 to 250 μm. The ferroselite grain dimensions were measured using a Nikon SMZ18 stereoscopic microscope ranging in diameter from ~0.6 to 1.6 mm. The chemical composition of the grains was inspected before and after reaction using SEM/EDS analysis in environmental mode (Tescan

Vega 3). All minerals were weighed and stored in N_2-purged 15 mL amber borosilicate vials with butyl rubber stoppers. In order to remove particles or ferric hydroxide rinds, all minerals were rinsed with N_2-purged 18.2 MΩ Milli-Q and ethanol and subsequently dried under a N_2 atmosphere (Schoonen et al., 2010).

All batch reactors contained a synthetic groundwater matrix with an ionic strength of 0.08 M, at pH 7 to 7.25. For the experiments with berzelianite, the solution was buffered with PIPES (3 g L^{-1}) and held at a pH of 7.0. In the other experiments, $NaHCO_3$ was added to the matrix for a final concentration of 0.5 mM HCO_3^-. The formation of Fe(III)-(oxy)hydroxide rinds can passivate the surface of iron sulfides and terminate the oxidation reaction of Fe(II) at neutral pH (Caldeira et al., 2010). The presence of carbonate species increases the kinetics of oxidation, primarily by the facilitating oxidation of dissolved Fe(II) through formation of Fe(III)-carbonate inner-sphere complexes on mineral surfaces (Evangelou et al., 1998). These complexes act as an electron conduit from reduced sulfide or selenide phases to $O_{2(aq)}$. Both of the aqueous solutions used in the ferroselite and berzelianite experiments were purged with O_2-free N_2 prior to addition and allowed to equilibrate with the mineral for at least seven hours. Average blank contribution from 4 reactors was 0.05 ng Se.

The addition of H_2O_2, as the oxidant, initiated each experiment, except for one ferroselite experiment that was open to air. Multiple vials for each experimental condition were created, so that one vial could be sacrificed at each time point. Enough 30% H_2O_2 was added to each set of vials to attain a final concentration of 0.40 mM ("Berz-Low") or 1.0 mM H_2O_2 ("Berz-High) for the berzelianite oxidation experiments (Table 4.1). These concentrations were chosen to reflect waters fully saturated and less saturated with respect to O_2. Similar amounts of H_2O_2 were planned to the "F2" (0.40 mM) and F3 (1.0 mM) of the ferroselite experiments. However, the observed reaction rates indicate that the H_2O_2 stock solution was degraded and far less oxidant was added than expected (see Results and Discussion section). An additional third experiment of ferroselite was conducted with 0.1 mM H_2O_2 ("F1") (Table 4.1). Vials in one ferroselite experiment were left open to the air ("FA"), under an inverted beaker, to prevent contamination, evaporation and to allow equilibration with air. Agitation with Teflon-coated stir bars allowed homogeneous reaction conditions over the course of the each experiment. Experiments were conducted in parallel, rather than via repeated sampling of vials over time. Vials were sacrificed at various timepoints by withdrawing the liquid with a 5 mL syringe and filtering with a 0.22 μm syringe filter. All samples were acidified with HCl to pH 2 and refrigerated. All time points were measured for $\delta^{82/76}$Se in the ferroselite experiments, while $\delta^{82/76}$Se was obtained for samples taken prior to 72 hours. To obtain the starting $\delta^{82/76}$Se of the each solid, 0.02 g each of ferroselite and berzelianite was digested in concentrated HCl at 110°C for 24 hours. An aliquot of the digested sample was diluted to 0.01 M HCl and stored for analysis.

Concentrations of digested minerals, total dissolved Se, Se(IV) (see Se(VI)-Se(IV) separation procedure below), Cu, and Fe of the aqueous samples were measured by iCAP ICP-MS (Thermo-Finnegan). All sample matrices were adjusted to 2% (v/v) HNO_3 prior to measurement. Calibration curves for each element were calculated based on measurements of the Agilent Multi-Element Calibration Standard 2A, and validated with measurements of a trace metal standard, NIST SRM 1643F. ^{73}Ge and ^{115}In, were used as internal standards to monitor instrumental drift and correct for matrix effects. Average limits of quantification for Se, Cu, and Fe was 0.1, 0.04 and 0.1 ng mL^{-1}, respectively.

Separation of Se(VI) from Se(IV), and separation of Se from matrix and isobaric interferences is accomplished by an established anion-exchange chromatographic procedure as described in previous studies (Clark and Johnson, 2010; Ellis et al., 2003; Tan et al., 2020). Briefly, 1 mL of cleaned AG1-X8 (100-200 mesh, Bio-Rad Laboratories), was conditioned with 10 mL H_2O in a 10 mL Bio-Rad polyprep column. Approximately 50 or 100 ng of Se in the acidified sample was loaded onto the column and rinsed with 5 mL of H_2O. Se(IV) was then eluted in 5 mL 0.1 M HCl and Se(VI) was eluted in 5 M HCl. The average $\delta^{82/76}$Se of 7 processed SRM-3149 standards for this procedure was 0.08 ± 0.12‰ (2σ). Both fractions were collected in 25 mL borosilicate glass vials with Teflon-lined caps. The molarity of the Se(VI) samples was adjusted to 5.0 ± 0.1 M HCl and Se(VI) was reduced to Se(IV) by heating at 90°C for 2 hours. The matrix for both fractions was subsequently adjusted to 2.0 ± 0.1 M HCl. All samples were purged with N_2 to remove interfering Br species and left uncapped for 10 hours in a hood to equilibrate with atmospheric Kr.

As Se has seven stable isotopes (^{74}Se, ^{76}Se, ^{77}Se, ^{78}Se, ^{79}Se, ^{80}Se, ^{82}Se), correction for isotopic fractionation during preparation and drifts in instrumental mass bias can be accomplished by a double spike approach. This is a well-established technique (Schilling et al., 2015; Schilling et al., 2014), where a known mass of ^{77}Se-^{74}Se double spike solution is added prior to sample preparation. Enough double spike was added so that the ratio of ^{77}Se/^{78}Se was ~2.

Selenium isotope ratios were measured by Hydride Generation Multi-Collector Inductively Coupled Mass Spectrometry (HG MC-ICPMS) at the University of Illinois at Urbana-Champaign. This was accomplished using a Nu Plasma MC-ICPMS (Nu Instruments Ltd.) with a standard Faraday cup and ion counter configuration and an in-house hydride generation system following methods as described in previous studies (Clark and Johnson, 2010; Mitchell et al., 2013; Schilling et al., 2015; Schilling et al., 2014; Schilling et al., 2011). Hydride generation converts Se(IV) to $H_2Se_{(g)}$ by online continuous reaction of $NaBH_4$ with Se(IV) in an

HCl matrix. We used a solution of 0.4% (m/v) $NaBH_4$ and 0.2% (m/V) NaOH combined with a flow rate of 1 mL min^{-1} and 0.5 mL min^{-1} for the sample and reductant, respectively.

All Se isotopes were measured by Faraday collectors, with ^{78}Se on the Axial collector. Some of the interferences, ($^{36}Ar^{40}Ar$, $^{38}Ar^{40}Ar$, ^{82}Kr), were corrected almost completely by on-peak zeroes using a 2.0 M HCl blank solution. Residual ArAr was further subtracted by measurements of $^{40}Ar^{40}Ar$ on H5 and calculation of intensities of $^{36}Ar^{40}Ar$ and $^{38}Ar^{40}Ar$ using assumed natural isotopic composition of Ar and the instrumental mass bias determined from the Se isotopes. The isobaric interferences, ^{74}Ge, $H^{75}As$, $H^{79}Br$, and $H^{81}Br$, were corrected by monitoring ^{73}Ge, ^{75}As, and 79Br on the IC0 ion counter, and the L4 and H2 Faraday collectors, respectively. An iterative routine was employed to correct for these interferences and calculate $^{82}Se/^{76}Se$. The double spike concentration was calibrated such that $^{82}Se/^{76}Se$ measurements of the sample-spike mixture were converted to precise concentrations of Se were obtained by isotope dilution. The Se concentration values reported in Table 4.2 were determined this way.

Each sample's $^{82}Se/^{76}Se$ ratio is reported relative to the standard NIST SRM 3149 (Lot no. 992106) are expressed using the following delta notation (‰):

$$\delta^{82/76}Se = [\frac{^{82}Se/^{76}Se_{sample}}{^{82}Se/^{76}Se_{standard}} - 1] * 1000 \tag{4.1}$$

The NIST SRM 3149 solution was analyzed before and after blocks of five samples, and in-house standard MH495 was measured every 10 samples to ensure consistent offset of ~3.50‰ between MH495 and NIST SRM 3149. At least 15% of the samples measured over the analytical session were duplicates. The working measurement uncertainty, based on results of 10 pairs of duplicate samples, was 0.14‰ (2σ).

4.3 Results and Discussion

4.3.1 Concentration results and patterns of reaction

Concentration data from all experiments is given in Table 4.2 and Figure 4.1. For experiments F2 and F3, total aqueous Se concentrations reached steady state after 24 hours (Figure 4.1A). The extent of oxidation was limited and a lower mass of Se was released compared to F1 (Table 4.2, Figure 4.1). Therefore, we infer that the H_2O_2 concentrations were much lower than the intended concentrations, possibly due to degradation of the stock solution. For experiments F1 and FA, Se concentrations continued to increase after 1.5 weeks (Table 4.2). Fe aqueous concentrations were mostly below the limit of quantification (1.8 nM) over the course of the experiment.

In the berzelianite experiments, Cu and Se concentrations increased in a 3:1 ratio over the course of the experiments (Figure 4.1B). This is somewhat greater than the 2:1 stoichiometry of the mineral. Selenium concentrations reached steady state at 72 hours for Berz-High, while Se concentrations in Berz-Low increased over the entire experiment (1.5 weeks).

The addition of H_2O_2 increased the kinetics of Se oxidation initially, as seen in Berz-Low and Berz-High (Figure 4.1B). Hydrogen peroxide can serve as an electron acceptor on fresh pyrite surfaces before desorbing and forming hydroxyl radicals through the Fenton reaction (Gil-Lozano et al., 2017). During this reaction, H_2O_2 oxidizes Fe^{2+} and reduce Fe^{3+} to produce water and the reactive oxygen species, $OH^{\bullet}$, $HO_2^{\bullet}$, and $O_2^{-\bullet}$. The $OH^{\bullet}$ and $O_2^{-\bullet}$ species can break down to form H_2O and O_2, while the combination of two $OH^{\bullet}$ can generate H_2O_2 (Gil-Lozano et al., 2017). Schoonen et al. (2010) reported a 40% increase in pyrite oxidation rate with the addition of H_2O_2 relative to a pyrite oxidation experiment with O_2 and catalase to decompose H_2O_2.

Only a small fraction (<1.8%) of the Se present in each mineral was released over the course of each experiment (Table 4.1). Accordingly, ferroselite and berzelianite oxidation must have been limited by the availability of oxidant. Decomposition of H_2O_2, known to occur on Fe(III)-(oxy)hydroxide patches on pyrite, produces O_2, which is a less effective oxidant than H_2O_2 (Schoonen et al., 2010). For acid-washed pyrite, this reaction occurs over a timescale of hours, similar to the timescale of oxidation in our experiments. Experiment FA, which was well mixed with air over the course of the experiment, displayed the highest final concentration of dissolved Se (Table 4.2). In this experiment, electron transfer to adsorbed $O_{2(aq)}$ from non-oxidized ferroselite surfaces could have produced low levels of H_2O_2, which would act as an oxidant as described previously (Schoonen et al., 2010). Constant agitation of the mineral grains could have caused exposure of new unoxidized surfaces as the grains fractured. Therefore, slow, continuous production of H_2O_2 throughout the experiment may account for the continuous slow oxidation observed in FA (Figure 4.1A).

4.3.2 Lack of isotopic fractionation in total dissolved Se for most experiments

In most of the experiments (FA, F1, Berz-Low, and Berz-High) the $\delta^{82/76}$Se values of total dissolved Se are generally close to that of the bulk mineral composition, (Figure 4.2). Differences are less than 0.5‰ in all cases except the 24 hr. time points for both berzelianite experiments. Given that the differences are very small (<0.5‰) at all other times (Figure 4.2), and by examining patterns in the Se(VI) and Se(IV) isotopic composition time trends (see below), we infer, speculatively, that the Berz-Low Se(IV) and Berz-High Se(VI) samples were interchanged during preparation or analysis. If this apparent error is corrected, the $\delta^{82/76}$Se values of total dissolved Se match the minerals values within 0.5‰ in all cases. Regardless of the actual source of error, we disregard the results from these two samples in favor of the strong pattern observed with the other 17 data points from these four experiments.

The observed lack of isotopic contrast between the minerals and total dissolved Se in these four experiments is consistent with a simple model for dissolution of solid phases. Isotopic effects that occur as the surface of a dissolving solid are expected to be muted by a simple mass balance principle that is known as the “rind effect”(Wang et al., 2015). Kinetic isotopic fractionation could occur during the dissolution of an individual monolayer, but as dissolution proceeds, each monolayer must be completely removed before deeper layers can be accessed. The quantitative conversion of each monolayer to dissolved species negates any kinetic effects occurring as atoms are removed from the surface. For any kinetic isotope effect, the surface becomes increasingly fractionated relative to the bulk solid, until the point where the dissolution flux matches the bulk solid isotopically. This must occur by the time several monolayers have been removed. In our experiments, Se concentrations at the first time points show that many atomic monolayers (~100’s) were dissolved, and thus, transient kinetic effects from simple dissolution of the solids are not expected to affect the results. Therefore, a change in the total dissolved isotopic composition would indicate a loss of Se(IV) or Se(VI) mass from solution, due to processes like adsorption or reduction. Any isotopic fractionation of Se(IV) and Se(VI) in these experiments most likely occurs due to interactions between Se(IV) and Se(VI).

There are exceptions to this rule. Isotopic fractionation during dissolution of solid phases has been observed for reductive dissolution of Fe(III)-oxyhydroxides (Brantley et al., 2004; Wiederhold et al., 2006; Wu et al., 2011), proton promoted dissolution of zinc in biotite (Weiss et al., 2014), and for silicon isotopes during basalt weathering (Ziegler et al., 2005). Wu et al. (2011) reported that dissolved Fe(II) produced was 3.0‰ lighter than the solid, which was attributed to very rapid attainment of isotopic equilibrium between the surface Fe(III) and the aqueous Fe(II). This rapid equilibration is unusual, and arises from the fact that only one electron transfer is need to complete Fe(II)-Fe(III) isotopic exchange. The oxidative dissolution of Se-bearing solids in our experiments would not be expected to produce similar isotope effects: multiple electron transfers would need to take place between the reduced Se solid and Se(IV), and major coordination changes are also needed to enable isotopic exchange.

4.3.3 Generation of high $\delta^{82/76}$Se-Se(VI)

In all experiments, with the exception of Berz-High, $\delta^{82/76}$Se-Se(VI) is greater than $\delta^{82/76}$Se-Se(IV) and the mineral over the course of the experiment. Dissolved Se(VI) quickly evolves to be isotopically much heavier than Se(IV) in the FA, F1, and Berz-Low experiments (Figure 4.3). These isotope effects coincide with increasing production of Se(IV) relative to Se(VI) prior to H_2O_2 being completely consumed (Figures 4.1 and 4.4). The $\delta^{82/76}$Se of Se(VI) increased 3.0‰ within the first hour for Berz-Low and 6.0‰ in 40 minutes for FA and F1 (Figure 4.3). Similar increases in the $\delta^{82/76}$Se of the Se(IV) fraction are not observed. In the Berz-Low experiment, Se(IV) remained 1‰ isotopically light relative to the bulk mineral composition. Meanwhile, in FA and F1 $\delta^{82/76}$Se of Se(IV) remained unchanged relative to the mineral (Figure 4.3A). These observations show that different processes are controlling the isotopic evolution of Se(VI) and Se(IV) for these experiments.

The data clearly require some process that drives Se(VI) toward greater $\delta^{82/76}$Se values. Kinetic isotope effects during Se(IV) oxidation could drive Se(VI) isotopically heavier. As shown by Schauble (2004), if the transition state and products of a reaction contain stronger metal(loid)-oxygen bonds, the fractionation due to electron transfer should be positive (product is heavy). While there are no studies that have shown electron transfer occurs through an Se(V) intermediate species, the Se(VI)-O bond length, 1.66-1.68 Å, is known to be shorter than Se(IV)-O bond length, 1.72-1.74 Å (Foster et al., 2003; Li and Liu, 2011; Peak, 2006). The shorter bonds are stiffer and drive the isotopic fractionation. This pathway is a plausible explanation for the isotopic fractionation observed within the first hours in Experiments FA, F1, and Berz–Low (Figure 4.3).

As a result of this reaction, Se(IV) would be driven isotopically lighter. This is observed within the first few timepoints for Berz-Low, Berz-High, and slightly in F1 (Table 4.3, Figure 4.3). There is no observable decreased in $\delta^{82/76}$Se-Se(IV) for FA. In both FA and F1, only a very small fraction of the Se(IV) pool is oxidized to Se(VI) (Figure 4.4). Therefore, the expected isotopic shift is very small for those experiments.

Isotopic exchange between dissolved Se(VI) and Se(IV) could also produce isotopically heavy Se(VI) and light Se(IV). However, recent work by Tan et al. (2020) shows that measurable isotopic exchange occurs very slowly (on the order of 10^5 years to reach equilibrium). If this process occurs rapidly enough, though, the offset between Se(IV) and Se(VI) would tend to increase over the course of the experiment as the reaction moves toward isotopic equilibrium. This is observed in experiments FA and F1 (Figure 4.3A). Previous studies have theoretically calculated equilibrium isotope fractionation factors for Se(IV) and Se(VI) of 13.78 to 13.28‰ (Li and Liu, 2011); a substantial evolution toward isotopic equilibrium could thus contribute to the observed offsets of up to ~14‰. However, unless the mineral surface or some other catalyst in our experiments greatly increased the rate of isotopic exchange, the process is likely far too slow to drive the observed isotopic shifts.

Reduction of Se(VI) to Se(IV), and Se(IV) to Se(0), by sulfide or selenide minerals could drive the Se(VI) and Se(IV) in solution toward isotopically heavy compositions as well. EDS analysis with SEM indicated the presence of trace sulfide phases in the ferroselite specimen but not in the berzelianite. Mitchell et al. (2013) reported that partial Se(VI) reduction to Se(IV) and Se(0) occurred by reaction with pyrite and mackinawite, while Se(IV) reduction by iron sulfides occurred more rapidly, reaching completion in a few hours. Abiotic reduction of Se(VI) by green rust has been shown to induce a fractionation of ~ $\varepsilon^{82}Se/^{76}Se$~ -11‰ (Johnson and Bullen, 2003), while reduction of Se(IV) and Se(VI) by reaction with mackinawite resulted in $\varepsilon^{82}Se/^{76}Se$~ -10‰ and $\varepsilon^{82}Se/^{76}Se$~ -3.0‰, respectively (Mitchell et al., 2013). The isotopic offsets observed in Figure 4.3 agree with this range of fractionation.

Se(VI) or Se(IV) reduction could be coupled to selenide oxidation to Se(0). This would occur as follows for Se(VI) reduction by ferroselite and berzelianite:

$$FeSe_2 + HSeO_4^- + 2H^+ = 2Se(0) + Fe^{2+} + HSeO_3^{2-} + H_2O$$

$\Delta G_r°$ = -88.307 kJ mol^{-1} (Dean, 1979; Hatten, 1977)

$$Cu_2Se + HSeO_4^- + 2H^+ = Se(0) + 2Cu^+ + HSeO_3^- + H_2O$$

$\Delta G_r°$ = -59.646 kJ mol^{-1} (Dean, 1979; Krivovichev, 2017)

While reduction of Se(VI) by sulfide and selenide is overall thermodynamically favorable, in our conditions, the reduction rate would be limited by available mineral surface sites. The unreacted mineral surface area is small (1.5 to 9 mm^2). Nevertheless, if reduction by sulfide of Se(VI) or Se(IV) is possible as observed in previous studies, selenide is a more likely reductant because it is present in greater amounts. Consequently, the non-stoichiometric increase in Cu:Se observed in Figure 4.1 could be a result of this process, where partial reduction of Se(IV) to insoluble Se(0) would increase the ratio of Cu to total dissolved Se above that of the mineral.

If reduction of Se oxyanions occurred in our experiments, we would expect the rate constant for Se(IV) to be greater than that of Se(VI), due to the kinetic favorability of the former reaction and the higher adsorption affinity of Se(IV). However, large increases in $\delta^{82/76}$Se of Se(IV) were not present in F1 or Berz-Low (Figure 4.3A). This indicates that significant amounts of Se(0) are not being precipitated and was confirmed by a lack of Se(0) observed on the reacted mineral by SEM analysis. Continuous addition by unfractionated Se(IV) may dilute and mute any increase in $\delta^{82/76}$Se for the Se(IV) due to its reduction in experiment FA. As shown in Figure 4.4A, the rate of Se(IV) production is higher than Se(VI) production. Therefore, small amounts of reduction may have occurred simultaneously with high production of Se(IV).

4.3.4 Total dissolved $\delta^{82/76}$Se is isotopically heavy relative to ferroselite in F2 and F3

Unlike the four experiments discussed above, FA, F1, Berz-Low, and Berz-High, where $\delta^{82/76}$Se of total dissolved Se matched that of the oxidized mineral, total dissolved $\delta^{82/76}$Se in F2 and F3 is 5.0 to 6.0‰ isotopically heavier than the starting ferroselite composition (Figure 4.2; Table 4.3). Both Se(IV) and Se(VI) fractions increased to 6.0‰ within the first few hours (Figure 4.3A). After 24 hours, both fractions decreased slightly over the remainder of the experiment. This timing coincides with decrease in the rate of mineral oxidation (Figure 4.1A).

In these experiments, much less oxidant was added than in FA and F1, as indicated by the low amount of dissolved Se released and the early plateau of aqueous Se concentrations (Table 4.1). The less oxidizing conditions in the F2 and F3 experiments may have allowed significant reduction of Se(IV) on the less-oxidized mineral surface, while at the same time decreasing the influx of new Se(IV) that would tend to dilute the effects of reduction-related $\delta^{82/76}$Se increases. The sharp increase in $\delta^{82/76}$Se of Se(IV) seems to be indicative of isotopic fractionation during reduction of Se(IV) and lesser impact of fractionation due to oxidation of Se(IV) to Se(VI), which would drive $\delta^{82/76}$Se lower. In addition, the smaller Se(IV):Se(VI) ratio in these experiments relative to that in FA and F1 was likely driven by greater amounts of Se(IV) removal via reduction (Figure 4.4A).

Adsorption of Se(IV) can also contribute to heavy $\delta^{82/76}$Se. High attenuation of Se(IV) from seleniferous soils has been ascribed to adsorption of Se(IV) to Fe-(oxy)hydroxide (Dowdle and Oremland, 1998; Zawislanski and Zavarin, 1996). Inner-sphere adsorption of Se(IV) to mineral surface can induce isotopic fractionation of Se(IV). This occurs as a result of differences between the vibrational energies of the Se-O bonds for the adsorbed and aqueous species. Xu et al. (2020) found that $\Delta^{82/76}Se_{aqueous\text{-}solid}$ was 0.67 to 0.87‰ at equilibrium isotopic fractionation between Se(IV) adsorbed onto Fe_2O_3 at pH 7-8 and dissolved Se(IV), while isotopic fractionation induced by Se(VI) adsorption was <0.2‰. If significant Se adsorption were to occur, $\delta^{82/76}$Se of aqueous Se(IV) would become isotopically heavy over the course of the experiment, while $\delta^{82/76}$Se of Se(VI) would show a smaller offset. However, the increase in $\delta^{82/76}$Se in the experiment is much larger than the range of fractionation for adsorption. In addition, given the small surface area of the ferroselite grains used in these experiments (1.5 – 9 mm^2), a small proportion of Se(IV) would be adsorbed by oxidized Fe(III) patches. While adsorption of may be occurring, other processes like reduction of Se(IV) to Se(0) are much more likely to be driving $\delta^{82/76}$Se isotopically heavier.

4.3.5 Muted isotopic fractionation with higher H_2O_2 concentrations in Berz-High

$\delta^{82/76}$Se values of Se(VI) in the Berz-High experiment are significantly less elevated relative to those of Berz-Low. In Berz-High, an initial 1.2‰ increase in $\delta^{82/76}$Se of Se(VI) and corresponding 1.0‰ decrease of Se(IV) could reflect early isotope effects associated with oxidation (Figure 4.3B). However, $\delta^{82/76}$Se of Se(VI), with the exception of the timepoint at 24 hours, returned to relatively unfractionated values afterward. Based on these results, the addition of higher amounts of H_2O_2 produces a smaller increase of $\delta^{82/76}$Se-Se(VI). A recently published framework relating Marcus Theory to isotopic fractionation could explain this. As dictated by Marcus theory, which connects the kinetics of outer-sphere electron transfer to the thermodynamics of the reaction, the magnitude of kinetic isotopic fractionation for the oxidation of Se(IV) is related to the $\Delta G_r°$, or the standard free energy of a reaction (Joe-Wong and Maher, 2020; Marcus, 1997). As $\Delta G_r°$ becomes more negative, and the reaction becomes more favorable, isotopic fractionation due to differences in vibrational energies of the heavy and light isotopes decreases.

In this experiment, higher H_2O_2 concentrations could increase the logK of the oxidation reaction and drive $\Delta G_r°$ more negative, decreasing ε^{82}Se/^{76}Se of Se(IV) oxidation (Joe-Wong and Maher, 2020). This could explain why a 1.0‰ difference is observed between $\delta^{82/76}$Se of the Se(IV) and Se(VI) fraction, as opposed to the 5.0‰ difference observed between Se(IV) and Se(VI) in Berz-Low (Figure 4.3B). Similarly, the only previously published oxidation experiment of Se(IV), which reported no isotopic fractionation, used 3% H_2O_2 and was conducted in a strongly basic solution with a fast oxidation rate (Johnson, 2004). Based on these results and the general predictions of Marcus theory, we suggest that the weak isotopic fractionation apparent in the Berz-High experiment was a consequence of the higher concentration of oxidant.

4.3.6 Summary of the processes observed in these experiments

The experiments presented here show a complex interplay of processes affecting the dissolved $\delta^{82/76}$Se of Se(IV) and Se(VI). With the exception of the later stages of one experiment (Berz-High), the dissolved Se(VI) is isotopically heavier than the mineral and the Se(IV) fraction. Four processes could be responsible for driving Se(VI) isotopically heavier: (1) kinetic isotope fractionation during the oxidation of Se(IV) to Se(VI), (2) abiotic reduction of Se(VI) and Se(IV) by selenide and/or sulfide minerals, (3) isotopic exchange between Se(IV) and Se(VI) progressing toward isotopic equilibrium, and (4) to a lesser extent, adsorption of Se(IV) to Fe-(oxy)hydroxides. The relative impacts of these reactions on $\delta^{82/76}$Se and production of Se(IV) and Se(VI) are dependent on the oxidant concentration. At low oxidant concentrations (F2 and F3), reduction and/or adsorption drive $\delta^{82/76}$Se-Se(IV) the total dissolved $\delta^{82/76}$Se to more positive values. With the addition of more oxidant, the rate of mineral oxidation exceeds reduction/adsorption of Se(IV) and thus the isotopic effects of those processes are muted. In addition, possible kinetic isotope effects during oxidation of Se(IV) to Se(VI) could be responsible for Se(IV) and Se(VI) isotopic shifts in the first time steps of BH, BL, FA, and F1. Overall, future experiments are necessary to parse these reactions.

4.4 Environmental Implications

Understanding Se isotopic systematics contributes to ongoing efforts to understand the biogeochemical cycle in modern and ancient environments (Basu et al., 2016; Clark and Johnson, 2010; Mitchell et al., 2012; Schilling et al., 2015; Zhu et al., 2014). Until this point, isotopic fractionation during oxidative dissolution was usually assumed to be minimal and therefore was not taken into account when quantifying Se transformations. Our results show that significant isotopic offsets between dissolved Se(VI) and Se(IV) can occur within hours of H_2O_2 or $O_{2(aq)}$ oxidation of selenide-bearing minerals, driven by isotopic fractionation caused by oxidation, isotopic exchange, and/or reduction. Although our experiments only address one set of reactions out of many taking place during oxidative weathering environments, these simple experiments reveal a strong tendency for the released Se(VI) to be isotopically heavy by up to several per mil. We suggest that similar processes should operate in natural environments and produce similar isotopic shifts.

A second insight arises from our observation that the Se(VI) isotopic fractionation is more pronounced for lower H_2O_2 conditions more similar to environmentally relevant conditions (<1 μM) (Yuan et al., 2017). In the subsurface, "dark" H_2O_2 production is highest in transitional redox environments, where production of isotopically heavy Se(VI) is likely to take place (Yuan et al., 2017). Therefore, Se isotopic fractionation due to oxidative dissolution could be more pronounced in variable redox-settings such as a fluctuating water table.

The tendency for Se(VI) to be isotopically heavy relative to the oxidizing minerals under almost all conditions has implications for the use of Se isotopes to better understand modern environmental processes and ancient earth system evolution. At low rates of mineral oxidation (i.e. less oxidizing conditions), reduction of oxidized Se(IV) can drive this fraction isotopically heavy relative to its source rock. However, Se(VI) is more soluble than Se(IV), due to its lower adsorption affinity, and is typically more mobile in weathering environments (Clark and Johnson, 2010). Therefore, waters draining seleniferous shales should contain Se(VI) that is significantly isotopically heavier than more reduced species or host rock. This would drive the overall flux of Se from these environments isotopically heavy as Se(VI) is more mobile than Se(IV).

Indeed, there is evidence for this offset in dissolved Se(VI) and Se(IV) isotope values reported in previous studies. Clark and Johnson (2010) observed Se(VI) isotope values in waterways and groundwater draining the Mancos Shale that were 2.3 to 3.0‰ heavier than Se(IV) and two digests of the Mancos Shale. Zhu et al. (2014) reported that $\delta^{82/76}$Se of Se-bearing gypsum and seep waters draining Yutangba Plateau (China) shales were 2.5 to 2.7‰

isotopically heavier than moderately weathered shales. The consistent differences between $\delta^{82/76}$Se of Se(VI) and more reduced pools suggest similar fractionating mechanisms at these two sites where weathering of shales is occurring and may be indicative of oxidative dissolution processes occurring at the mineral grain scale.

Extrapolation of our results to quantify Se fluxes in the environment requires consideration of field rates of oxidative dissolution and other sources of Se. The kinetics of chemical reactions in natural settings are often orders of magnitude lower than those obtained from laboratory experiments (Jung and Navarre-Sitchler, 2018; White and Brantley, 2003). The isotopic evolution of Se(VI) at lower rates of reaction, similar to experiments F2 and F3, will depend on the reductants or adsorbants present. In addition, while selenide phases are important hosts of Se in marine sediments, elemental and organically-bound Se composes the majority of the refractory fraction in lightly weathered shales and Se-impacted soils (Stillings, 2010; Zawislanski and Zavarin, 1996). The fractionating mechanisms discussed here can inform future examinations of isotopic fractionation during Se(0) and organically-bound Se oxidation, and will help constrain the Se isotope effects during oxidative dissolution of seleniferous shales.

4.5 Conclusions

We present the first evidence of significant isotopic fractionation during oxidative dissolution of selenide-bearing minerals. The isotopic shift is most evident for the dissolved Se(VI) fraction; all experiments resulted in $\delta^{82/76}$Se-Se(VI) increasing to values that in some cases reached as high as 14‰. Several processes could be responsible for this evolution, oxidation of Se(IV), including reduction by sulfide/selenide, or isotopic exchange between the two dissolved species. The isotopic fractionation of dissolved Se(IV) was more muted except when very low levels of oxidant were present. This observation suggests that Se(IV) reduction is coupled to mineral oxidation, but may be overprinted by high fluxes of unfractionated Se(IV) when mineral oxidation rates are high. Given these results, the weathering flux of Se from Se-bearing rocks and soils, overall, should be dominated by isotopically heavy Se(VI), as this species is more soluble and mobile than Se(IV). This conclusion has implications for the usage of Se isotopes to track immobilizing reactions in modern and ancient settings.

4.6 Tables and Figures

Table 4.1. Conditions of mineral dissolution experiments.

	Ferroselite ($FeSe_2$)				**Berzelianite (Cu_2Se)**	
	FA	**F1**	**F2**	**F3**	**Berz -Low**	**Berz-High**
Mass (g)/ Volume (mL)	0.0001	0.0001	0.00004	0.00004	0.003	0.003
$H_2O_{2(aq)}$ (mM)	0	0.1	0.4*	1*	0.4	1
pH	7.25	7.25	7.15	7.15	7.00	7.00
% of Se in mineral released	1.81	1.60	0.80	0.40	0.80	1.51
$\delta^{82/76}$Se Mineral	0.36 ± 0.22‰ (2σ, n=3)				-3.85 ± 0.18‰ (2σ, n=4)	

*Intended concentrations. Actual concentrations must have been much lower (see text).

Table 4.2. Concentrations of dissolved Se, Se(IV), Se(VI), and Cu. All concentration units are in micromolar. Fe concentrations were below the limit of detection in the ferroselite experiments. All concentrations were obtained by isotope dilution, with the exception of Cu, Berz-Low and Berz-High samples at 72 hr, 98 hr, and 252 hr, which were measured by iCAP Q ICP-MS.

	Ferroselite							
Time	**FA**				**F1**			
Hr	**Se(IV)**	**Se(VI)**	**Total Se**	**Se(IV):Se(VI)**	**Se(IV)**	**Se(VI)**	**Total Se**	**Se(IV):Se(VI)**
0.67	0.42	0.06	0.48	6.95	0.72	0.21	0.93	3.41
4	0.81	0.11	0.93	7.09	2.20	0.34	2.54	6.47
21	4.60	0.14	4.74	33.20	8.53	0.26	8.78	33.34
46	13.31	0.38	13.70	34.86	13.31	0.31	13.62	43.19
168	67.84	1.63	69.47	41.51	35.18	1.06	36.24	33.12
Time	**F2**				**F3**			
Hr	**Se(IV)**	**Se(VI)**	**Total Se**	**Se(IV):Se(VI)**	**Se(IV)**	**Se(VI)**	**Total Se**	**Se(IV):Se(VI)**
0.08	0.07	0.14	0.21	0.51	0.12	0.18	0.29	0.66
0.50	0.15	0.24	0.38	0.61	0.07	0.18	0.26	0.41
1.00	0.31	0.26	0.58	1.20	0.19	0.22	0.41	0.88
6	0.56	0.46	1.02	1.21	0.28	0.24	0.52	1.14
24	0.80	0.47	1.26	1.69	0.25	0.38	0.63	0.66
72	1.21	0.68	1.89	1.78	0.48	0.53	1.00	0.90
144	1.23	0.60	1.83	2.05	0.32	0.47	0.78	0.69

	Berzelianite									
Time	**Berz -Low**					**Berz-High**				
Hr	**Se(IV)**	**Se(VI)**	**Total Se**	**Se(IV):Se(VI)**	**Cu**	**Se(IV)**	**Se(VI)**	**Total Se**	**Se(IV)/Se(VI)**	**Cu**
0.17	0.08	0.03	0.11	2.18	BLD	0.04	0.09	0.13	0.41	0.03
1	0.10	0.11	0.21	0.91	0.01	0.16	0.31	0.47	0.53	0.04
4.5	0.36	0.17	0.53	2.13	0.12	0.34	0.31	0.64	1.10	1.04
11.5	0.37	0.14	0.51	2.70	0.18	0.45	0.25	0.70	1.75	1.12
24	0.72	0.12	0.84	5.76	0.23	1.34	0.80	2.13	1.68	1.37
48	1.10	0.27	1.37	4.00	1.05	1.68	0.82	2.50	2.04	4.68
72	ND	ND	1.85	ND	3.36	ND	ND	3.14	ND	7.27
98	ND	ND	1.98	ND	3.74	ND	ND	2.97	ND	7.24
252	ND	ND	3.20	ND	7.27	ND	ND	2.82	ND	7.91

ND is not determined

Table 4.3. Se isotope values ($\delta^{82/76}$Se) of Se(IV), Se(VI), and total dissolved Se with associated uncertainties for all samples.

Ferroselite										
Time	**FA**					**F1**				
Hr	**$\delta^{82/76}$Se - Se(IV)**	**2σ**	**$\delta^{82/76}$Se - Se(VI)**	**2σ**	**$\delta^{82/76}$Se - Total**	**$\delta^{82/76}$Se - Se(IV)**	**2σ**	**$\delta^{82/76}$Se - Se(VI)**	**2σ**	**$\delta^{82/76}$Se - Total**
0.67	ND	-	5.92	0.15	ND	-4.23	0.14	5.83	0.12	-1.95
4	-0.41	0.15	ND	-	ND	-1.19	0.12	6.21	0.12	-0.20
21	-0.68	0.12	8.07	0.14	-0.46	-1.07	0.12	7.90	0.12	-0.81
46	-0.25	0.12	9.57	0.14	-0.15	-0.87	0.12	8.87	0.12	-0.65
168	-0.15	0.12	14.16	0.15	0.18	-0.67	0.12	10.56	0.13	-0.34
Time	**F2**					**F3**				
Hour	**$\delta^{82/76}$Se - Se(IV)**	**2σ**	**$\delta^{82/76}$Se - Se(VI)**	**2σ**	**$\delta^{82/76}$Se - Total**	**$\delta^{82/76}$Se - Se(IV)**	**2σ**	**$\delta^{82/76}$Se - Se(VI)**	**2σ**	**$\delta^{82/76}$Se - Total**
0.08	5.56	0.16	3.29	0.16	4.76	ND	-	2.91	0.16	ND
0.50	ND	-	3.44	0.13	ND	ND	-	4.54	0.13	ND
1.00	ND	-	4.55	0.13	ND	ND	-	3.80	0.13	ND
6	ND	-	6.07	0.13	ND	5.43	0.16	5.49	0.13	5.46
24	4.49	0.13	5.20	0.13	4.94	5.25	0.16	6.38	0.13	5.70
72	2.98	0.13	4.99	0.13	4.27	ND	-	5.62	0.15	ND
144	2.32	0.16	4.65	0.13	3.89	ND	-	5.23	0.15	ND
Berzelianite										
Time	**Berz -Low**					**Berz-High**				
Hr	**$\delta^{82/76}$Se - Se(IV)**	**2σ**	**$\delta^{82/76}$Se - Se(VI)**	**2σ**	**$\delta^{82/76}$Se - Total**	**$\delta^{82/76}$Se - Se(IV)**	**2σ**	**$\delta^{82/76}$Se - Se(VI)**	**2σ**	**$\delta^{82/76}$Se - Total**
0.17	-4.94	0.13	-2.66	0.13	-4.22	-4.67	0.13	-3.27	0.13	-3.67
1	-5.20	0.13	-1.47	0.13	-3.25	-4.80	0.13	-2.60	0.13	-3.36
4.5	-4.55	0.13	ND	0.13	ND	-3.93	0.13	-3.75	0.13	-3.84
11.5	-4.61	0.13	-0.78	0.13	-3.57	-4.11	0.13	-3.57	0.13	-3.91
24	-3.26	0.13	-0.01	0.13	-2.85	-4.76	0.17	-5.52	0.17	-5.02
48	-4.81	0.15	-0.33	0.13	-3.87	-4.32	0.15	-4.49	0.15	-4.37

ND: not determined

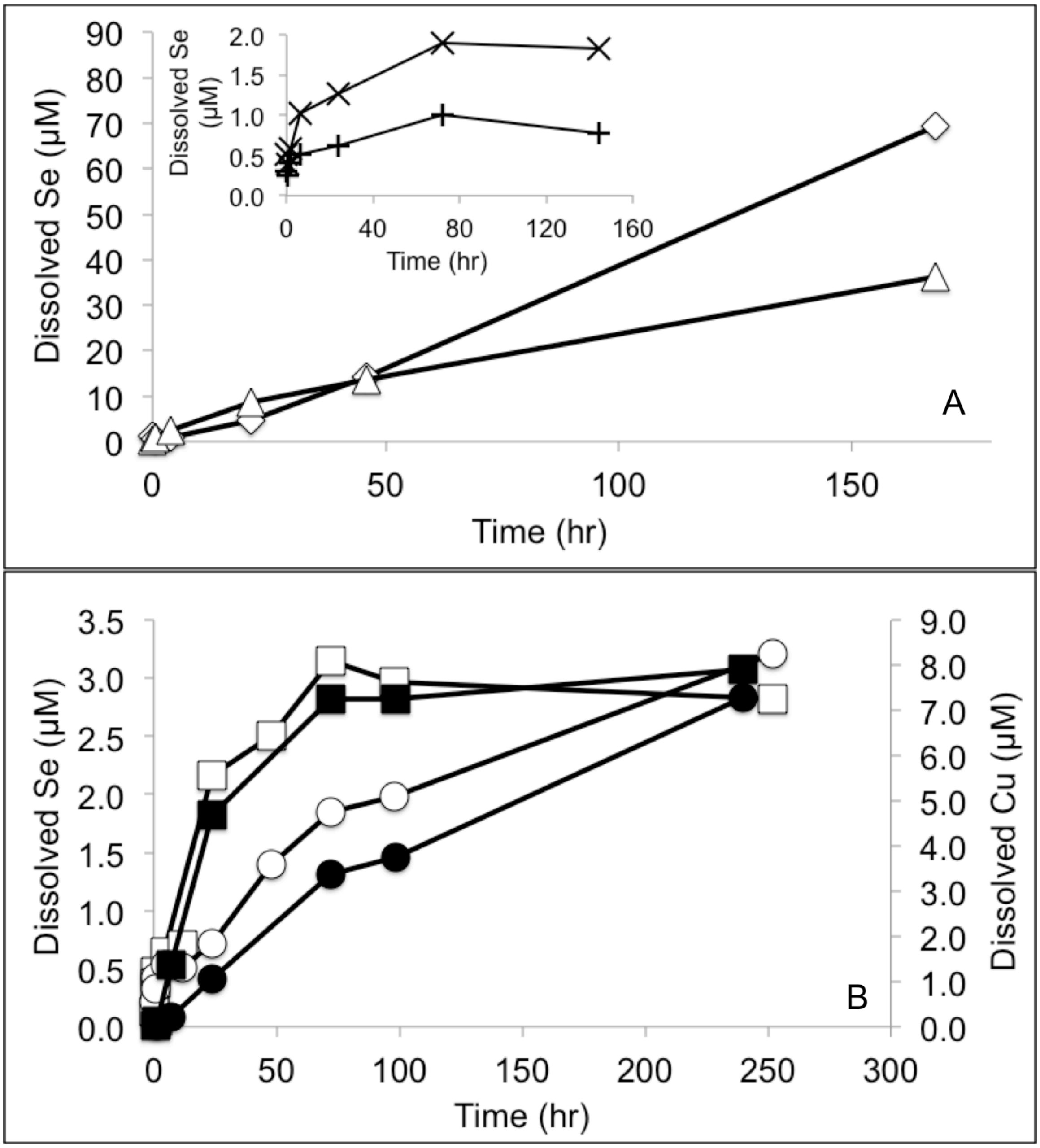

Figure 4.1. Evolution of total dissolved Se and Cu concentrations during the oxidation of ferroselite and berzelianite. Uncertainties (2σ) in concentrations are smaller than the symbols. (A) Selenium concentrations for FA and F1 are denoted by diamonds and triangles. In the inset, F2 and F3 are represented by (+) and (x), respectively. (B) White circles and squares indicate Se concentrations for Berz-Low and Berz-High, respectively, while black symbols denote Cu concentrations in Berz-Low and Berz-High.

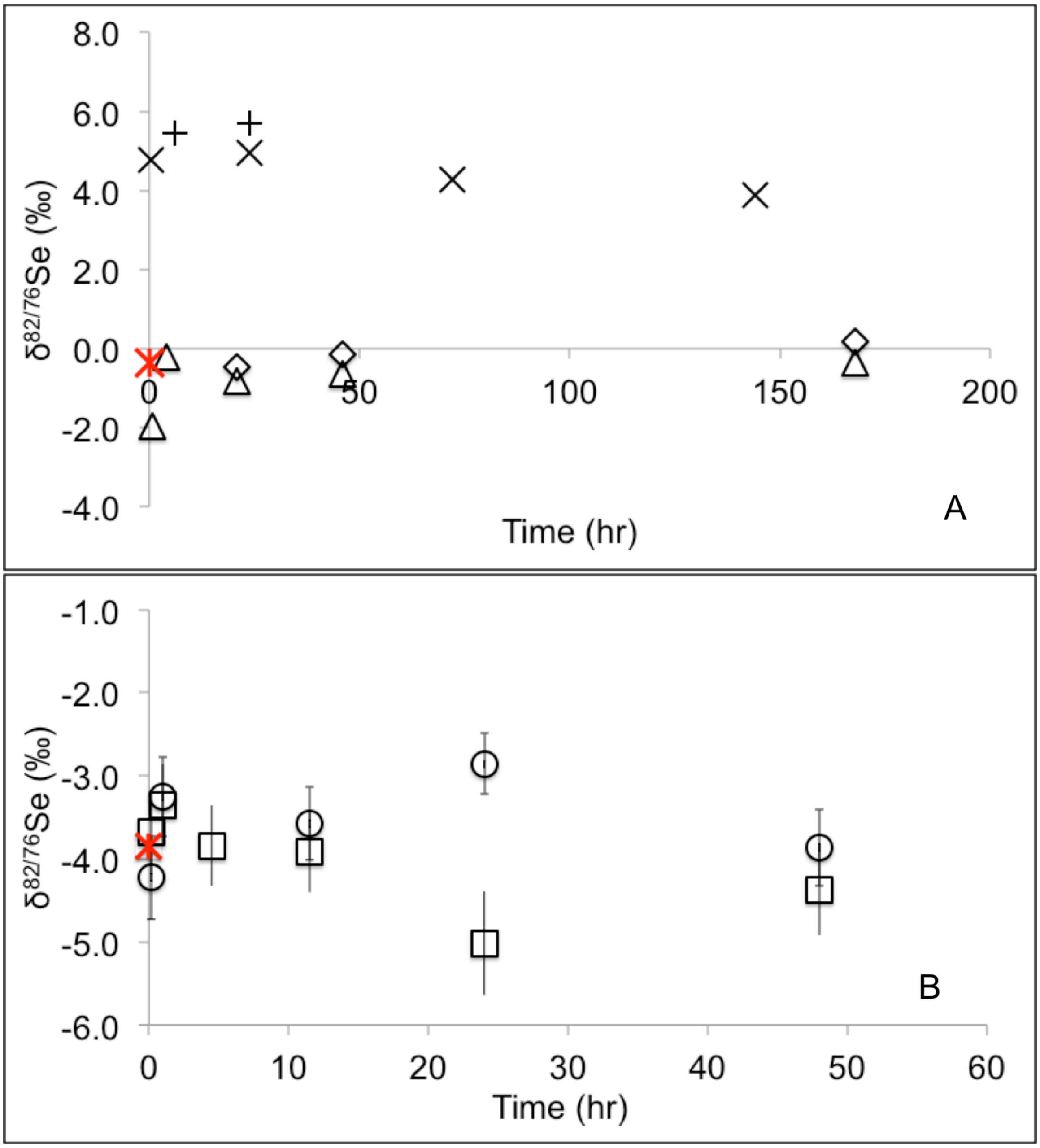

Figure 4.2. $\delta^{82/76}$Se values of total dissolved Se for (A) ferroselite experiments and (B) berzelianite experiments over time. Red stars represent the mineral isotopic compositions. (A) Uncertainties (2σ) are smaller than the symbols. Diamonds, triangles, +, and x indicate FA, F1, F2, and F3 respectively. (B) Squares and circles refer to $\delta^{82/76}$Se of Berz-High and Berz-Low, respectively.

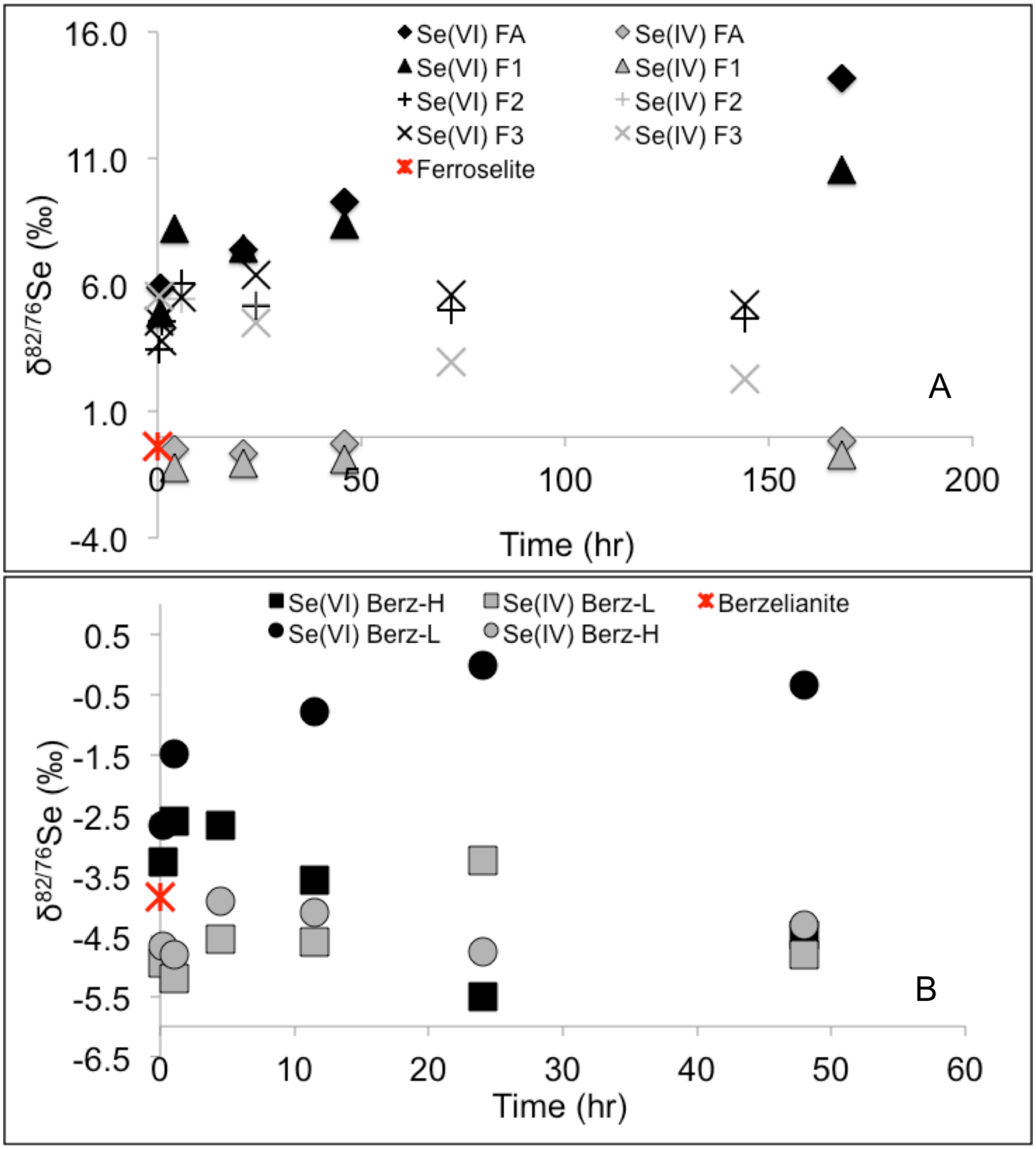

Figure 4.3. Isotopic evolution of dissolved Se(IV) and Se(VI) during the oxidative dissolution of (A) ferroselite and (B) berzelianite. Symbols assignments are the same as in earlier figures. Black symbols represent Se(VI) and grey symbols represent Se(IV). Error bars (2σ) are smaller than the symbols.

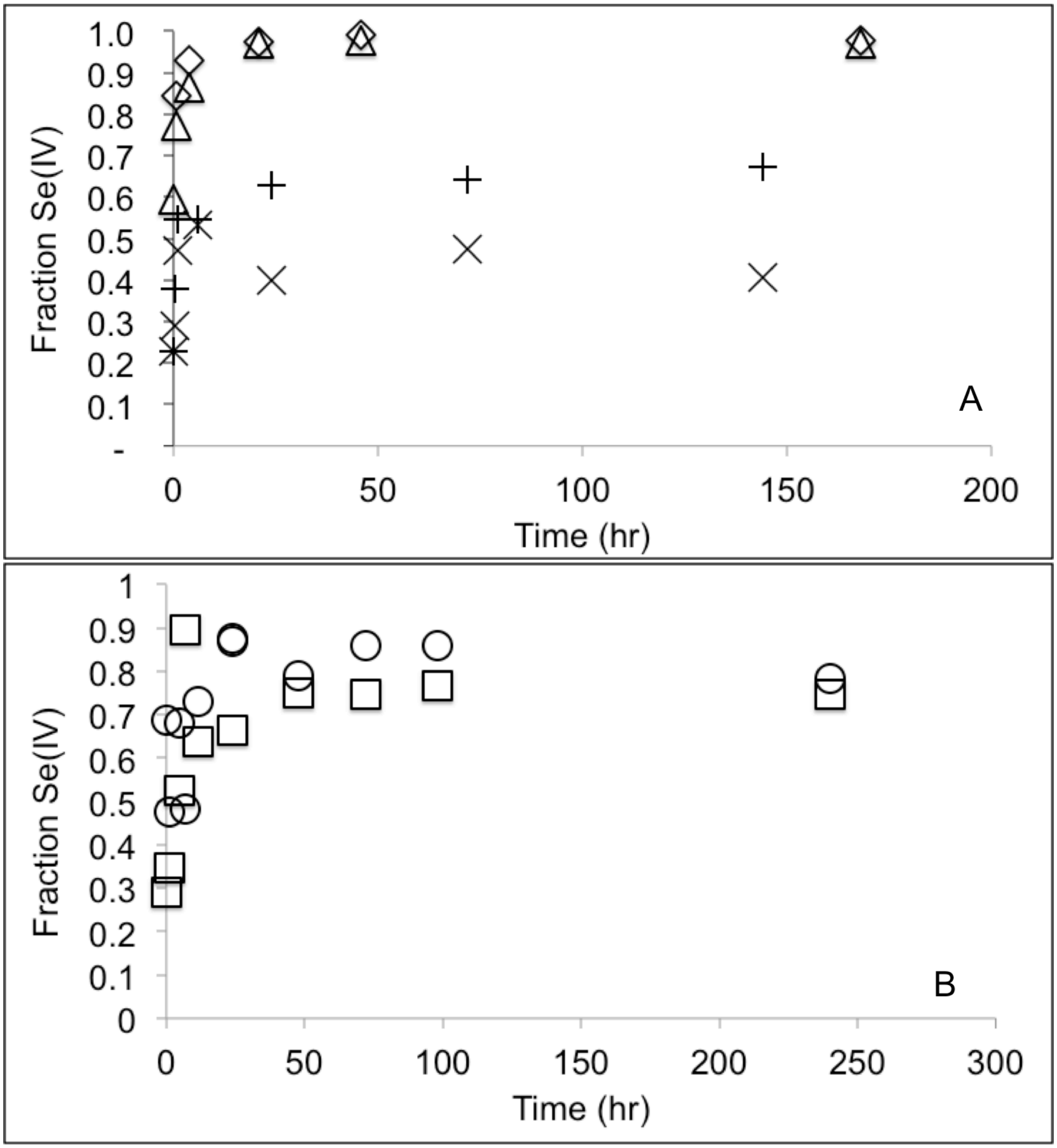

Figure 4.4. Fraction of dissolved Se(IV) relative to total dissolved Se during the oxidation of (A) ferroselite and (B) berzelianite over time. (A) Diamonds, triangles, +, and x indicate to FA, F1, F2, and F3 respectively. (B) Squares and circles refer to Berz-High and Berz-Low, respectively. Uncertainties (2σ) for fraction of dissolved Se(IV) are smaller than the symbols.

4.7 References

Arthur, J.R., Nicol, F. and Beckett, G.J. (1992) The role of selenium in thyroid hormone metabolism and effects of selenium deficiency on thyroid hormone and iodine metabolism. Biological Trace Element Research 34, 321-325.

Basu, A., Schilling, K., Brown, S.T., Johnson, T.M., Christensen, J.N., Hartmann, M., Reimus, P.W., Heikoop, J.M., Woldegabriel, G. and DePaolo, D.J. (2016) Se Isotopes as Groundwater Redox Indicators: Detecting Natural Attenuation of Se at an in Situ Recovery U Mine. Environmental Science & Technology 50, 10833-10842.

Borda, M.J., Elsetinow, A.R., Schoonen, M.A. and Strongin, D.R. (2001) Pyrite-Induced Hydrogen Peroxide Formation as a Driving Force in the Evolution of Photosynthetic Organisms on an Early Earth. Astrobiology 1, 283-288.

Brantley, S.L., Liermann, L.J., Guynn, R.L., Anbar, A., Icopini, G.A. and Barling, J. (2004) Fe isotopic fractionation during mineral dissolution with and without bacteria1 1Associate editor: J. B. Fein. Geochimica et Cosmochimica Acta 68, 3189-3204.

Caldeira, C.L., Ciminelli, V.S.T. and Osseo-Asare, K. (2010) The role of carbonate ions in pyrite oxidation in aqueous systems. Geochimica et Cosmochimica Acta 74, 1777-1789.

Clark, S.K. and Johnson, T.M. (2010) Selenium Stable Isotope Investigation into Selenium Biogeochemical Cycling in a Lacustrine Environment: Sweitzer Lake, Colorado. Journal of Environmental Quality 39, 2200-2210.

Cox, A.G., Tsomides, A., Kim, A.J., Saunders, D., Hwang, K.L., Evason, K.J., Heidel, J., Brown, K.K., Yuan, M., Lien, E.C., Lee, B.C., Nissim, S., Dickinson, B., Chhangawala, S., Chang, C.J., Asara, J.M., Houvras, Y., Gladyshev, V.N. and Goessling, W. (2016) Selenoprotein H is an essential regulator of redox homeostasis that cooperates with p53 in development and tumorigenesis. Proceedings of the National Academy of Sciences 113, E5562.

Dean, J.A. (1979) Lange's Handbook of Chemistry, 12th ed. McGraw-Hill, New York, NY.
Descostes, M., Vitorge, P. and Beaucaire, C. (2004) Pyrite dissolution in acidic media. Geochimica et Cosmochimica Acta 68, 4559-4569.

Dowdle, P.R. and Oremland, R.S. (1998) Microbial Oxidation of Elemental Selenium in Soil Slurries and Bacterial Cultures. Environmental Science & Technology 32, 3749-3755.

Ellis, A.S., Johnson, T.M., Herbel, M.J. and Bullen, T.D. (2003) Stable isotope fractionation of selenium by natural microbial consortia. Chemical Geology 195, 119-129.

EPA (2018) 2018 Edition of the Drinking Water Standards and Health Advisories Tables. U.S. Environmental Protection Agency, Washington, DC.

Evangelou, V.P., Seta, A.K. and Holt, A. (1998) Potential Role of Bicarbonate during Pyrite Oxidation. Environmental Science & Technology 32, 2084-2091.
Foster, A.L., Brown, G.E. and Parks, G.A. (2003) X-ray absorption fine structure study of As(V) and Se(IV) sorption complexes on hydrous Mn oxides. Geochimica et Cosmochimica Acta 67, 1937-1953.

Gil-Lozano, C., Davila, A.F., Losa-Adams, E., Fairén, A.G. and Gago-Duport, L. (2017) Quantifying Fenton reaction pathways driven by self-generated H2O2 on pyrite surfaces. Scientific Reports 7, 43703.

Hatten, H., J. (1977) Geochemistry of selenium: formation of ferroselite and selenium behavior in the vicinity of oxidizing sulfide and uranium deposits. Geochimica et Cosmochimica Acta 41, 1665-1678.

Herbel, M.J., Johnson, T.M., Oremland, R.S. and Bullen, T.D. (2000) Fractionation of selenium isotopes during bacterial respiratory reduction of selenium oxyanions. Geochimica et Cosmochimica Acta 64, 3701-3709.

Joe-Wong, C. and Maher, K. (2020) A model for kinetic isotope fractionation during redox reactions. Geochimica et Cosmochimica Acta 269, 661-677.

Johnson, T.M. (2004) A review of mass-dependent fractionation of selenium isotopes and implications for other heavy stable isotopes. Chemical Geology 204, 201-214.

Johnson, T.M. and Bullen, T.D. (2003) Selenium isotope fractionation during reduction by Fe(II)-Fe(III) hydroxide-sulfate (green rust). Geochimica et Cosmochimica Acta 67, 413-419.

Johnson, T.M., Herbel, M.J., Bullen, T.D. and Zawislanski, P.T. (1999) Selenium isotope ratios as indicators of selenium sources and oxyanion reduction. Geochimica et Cosmochimica Acta 63, 2775-2783.

Jung, H. and Navarre-Sitchler, A. (2018) Scale effect on the time dependence of mineral dissolution rates in physically heterogeneous porous media. Geochimica et Cosmochimica Acta 234, 70-83.

Krivovichev, V.C., M.; Vishnevsky, A. (2017) The Thermodynamics of Selenium Minerals in Near-Surface Environments. Minerals 7, 188.

Kulp, T.R. and Pratt, L.M. (2004) Speciation and weathering of selenium in upper cretaceous chalk and shale from South Dakota and Wyoming, USA. Geochimica et Cosmochimica Acta 68, 3687-3701.

Labunskyy, V.M., Hatfield, D.L. and Gladyshev, V.N. (2014) Selenoproteins: molecular pathways and physiological roles. Physiological reviews 94, 739-777.

Lefticariu, L., Pratt, L.M. and Ripley, E.M. (2006) Mineralogic and sulfur isotopic effects accompanying oxidation of pyrite in millimolar solutions of hydrogen peroxide at temperatures from 4 to 150°C. Geochimica et Cosmochimica Acta 70, 4889-4905.

Lemly, A.D. (2004) Aquatic selenium pollution is a global environmental safety issue. Ecotoxicology and Environmental Safety 59, 44-56.

Lenz, M. and Lens, P.N.L. (2009) The essential toxin: The changing perception of selenium in environmental sciences. Science of The Total Environment 407, 3620-3633.

Li, X. and Liu, Y. (2011) Equilibrium Se isotope fractionation parameters: A first-principles study. Earth and Planetary Science Letters 304, 113-120.

Lowson, R.T. (1982) Aqueous oxidation of pyrite by molecular oxygen. Chemical Reviews 82, 461-497.

Luoma, S.N. and Presser, T.S. (2009) Emerging Opportunities in Management of Selenium Contamination. Environmental Science & Technology 43, 8483-8487.

Ma, Y. and Lin, C. (2013) Microbial Oxidation of Fe2+ and Pyrite Exposed to Flux of Micromolar H2O2 in Acidic Media. Scientific Reports 3, 1979.

Marcus, R.A. (1997) Electron transfer reactions in chemistry theory and experiment. Journal of Electroanalytical Chemistry 438, 251-259.

Mitchell, K., Couture, R.-M., Johnson, T.M., Mason, P.R.D. and Van Cappellen, P. (2013) Selenium sorption and isotope fractionation: Iron(III) oxides versus iron(II) sulfides. Chemical Geology 342, 21-28.

Mitchell, K., Mason, P.R.D., Van Cappellen, P., Johnson, T.M., Gill, B.C., Owens, J.D., Diaz, J., Ingall, E.D., Reichart, G.-J. and Lyons, T.W. (2012) Selenium as paleo-oceanographic proxy: A first assessment. Geochimica et Cosmochimica Acta 89, 302-317.

Ohlendorf, H.M. (1989) Bioaccumulation and Effects of Selenium in Wildlife. Selenium in Agriculture and the Environment, 133-177.

Ohlendorf, H.M., Hothem, R.L., Bunck, C.M. and Marois, K.C. (1990) Bioaccumulation of selenium in birds at Kesterson Reservoir, California. Archives of Environmental Contamination and Toxicology 19, 495-507.

Peak, D. (2006) Adsorption mechanisms of selenium oxyanions at the aluminum oxide/water interface. Journal of Colloid and Interface Science 303, 337-345.

Presser, T.S., Piper, D.Z., Bird, K.J., Skorupa, J.P., Hamilton, S.J., Detwiler, S.J. and Huebner, M. (2004) The phosphoria formation: A model for forecasting global selenium sources to the environment. Handbook of exploration and environmental geochemistry 8, 299-319.

Presser, T.S. and Swain, W.C. (1990) Geochemical evidence for Se mobilization by the weathering of pyritic shale, San Joaquin Valley, California, U.S.A. Applied Geochemistry 5, 703-717.

Presser, T.S., Sylvester, M.A. and Low, W.H. (1994) Bioaccumulation of selenium from natural geologic sources in western states and its potential consequences. Environmental Management 18, 423-436.

Schauble, E.A. (2004) Applying Stable Isotope Fractionation Theory to New Systems. Reviews in Mineralogy and Geochemistry 55, 65-111.

Schilling, K., Johnson, T.M., Dhillon, K.S. and Mason, P.R.D. (2015) Fate of Selenium in Soils at a Seleniferous Site Recorded by High Precision Se Isotope Measurements. Environmental Science & Technology 49, 9690-9698.

Schilling, K., Johnson, T.M. and Mason, P.R.D. (2014) A sequential extraction technique for mass-balanced stable selenium isotope analysis of soil samples. Chemical Geology 381, 125-130.

Schilling, K., Johnson, T.M. and Wilcke, W. (2011) Isotope Fractionation of Selenium During Fungal Biomethylation by Alternaria alternata. Environmental Science & Technology 45, 2670-2676.

Schoonen, M.A.A., Harrington, A.D., Laffers, R. and Strongin, D.R. (2010) Role of hydrogen peroxide and hydroxyl radical in pyrite oxidation by molecular oxygen. Geochimica et Cosmochimica Acta 74, 4971-4987.

Stillings, L.L.A., Michael C. (2010) Kinetics of selenium release in mine waste from the Meade Peak Phosphatic Shale, Phosphoria Formation, Wooley Valley, Idaho, USA. Chemical Geology 269, 113-123.

Tan, D., Zhu, J.-M., Wang, X., Johnson, T.M., Li, S. and Xu, W. (2020) Equilibrium fractionation and isotope exchange kinetics between aqueous Se(IV) and Se(VI). Geochimica et Cosmochimica Acta 277, 21-36.

Trelease, S.F.B., Orville A. (1950) Selenium. Journal of the American Pharmaceutical Association 39, 364-364.

Wang, X., Johnson, T.M. and Lundstrom, C.C. (2015) Isotope fractionation during oxidation of tetravalent uranium by dissolved oxygen. Geochimica et Cosmochimica Acta 150, 160-170.

Weiss, D.J., Boye, K., Caldelas, C. and Fendorf, S. (2014) Zinc Isotope Fractionation during Early Dissolution of Biotite Granite. Soil Science Society of America Journal 78, 171-179.

White, A.F. and Brantley, S.L. (2003) The effect of time on the weathering of silicate minerals: why do weathering rates differ in the laboratory and field? Chemical Geology 202, 479-506.

Wiederhold, J.G., Kraemer, S.M., Teutsch, N., Borer, P.M., Halliday, A.N. and Kretzschmar, R. (2006) Iron Isotope Fractionation during Proton-Promoted, Ligand-Controlled, and Reductive Dissolution of Goethite. Environmental Science & Technology 40, 3787-3793.

Wu, L., Beard, B.L., Roden, E.E. and Johnson, C.M. (2011) Stable Iron Isotope Fractionation Between Aqueous Fe(II) and Hydrous Ferric Oxide. Environmental Science & Technology 45, 1847-1852.

Xu, W., Zhu, J.-M., Johnson, T.M., Wang, X., Lin, Z.-Q., Tan, D. and Qin, H. (2020) Selenium isotope fractionation during adsorption by Fe, Mn and Al oxides. Geochimica et Cosmochimica Acta 272, 121-136.

Yuan, X., Nico, P.S., Huang, X., Liu, T., Ulrich, C., Williams, K.H. and Davis, J.A. (2017) Production of Hydrogen Peroxide in Groundwater at Rifle, Colorado. Environmental Science & Technology 51, 7881-7891.

Zawislanski, P.T. and Zavarin, M. (1996) Nature and Rates of Selenium Transformations: A Laboratory Study of Kesterson Reservoir Soils. Soil Science Society of America Journal 60, 791-800.

Zhu, J.-M., Johnson, T.M., Clark, S.K., Zhu, X.-K. and Wang, X.-L. (2014) Selenium redox cycling during weathering of Se-rich shales: A selenium isotope study. Geochimica et Cosmochimica Acta 126, 228-249.

Ziegler, K., Chadwick, O.A., Brzezinski, M.A. and Kelly, E.F. (2005) Natural variations of δ30Si ratios during progressive basalt weathering, Hawaiian Islands. Geochimica et Cosmochimica Acta 69, 4597-4610.

CHAPTER 5: TELLURIUM CONCENTRATIONS AND ISOTOPIC FRACTIONATION AS INDICATORS OF THE RISE OF ATMOSPHERIC O_2

Abstract

The expansion of multi-cellular life is thought to have been triggered by the increased environmental availability of O_2 during the Neoproterozoic Oxidation Event after low levels of O_2 during the mid-Proterozoic. This is supported by the isotopic fractionation of redox-sensitive elements in near shore sediments and paleosols. For the Cr and U isotope systems, isotopic fractionation in the geologic record deviates from average crustal values after levels of O_2 were high enough to initiate redox cycling induce redox-driven isotopic fractionation. This oxidative threshold, or when insoluble Cr(III) or U(IV) were oxidized to their more soluble forms, is dependent on the thermodynamic behavior of each element. Based on known Te thermodynamic data, tellurium (Te) stable isotopes could be sensitive to lower levels of O_2 than Cr and higher concentrations of O_2 than the U paleoredox proxy. We examined Te enrichments and isotopic fractionation in a suite of paleosols and ironstone formations. Tellurium loss from the paleosols is apparent after the Great Oxidation Event, in addition to Te isotopic fractionation in paleosols and ironstone formations deviating from average unweathered crustal isotope values after the initiation of the Great Oxidation Event. While this dataset is limited, the results of this study are promising for the use of Te isotopes as a proxy of oxidative weathering and atmospheric oxygen.

5.1 Introduction

Advances in understanding the evolution of life have been bolstered in the last two decades by new approaches to studying past redox conditions. The energetic conditions for the development of multicellular life theoretically require an environment with at least 1% of present atmospheric levels (PAL) of O_2 (Payne et al., 2011). Possibly not coincidentally, the emergence of complex multicellular life correlates with the rise in atmospheric pO_2 concentrations close to modern levels. However, the timing of this rise is debated along with the influence of atmospheric O_2 on the oxygenation of the marine environment, which is where multicellular life is thought to originate. A complete assessment of O_2 levels in both the marine system and the atmosphere is necessary in order to understand what triggered the emergence of metazoans.

Quantification of atmospheric pO_2 prior to the appearance of animals in the Neoproterozoic fossil record reflects a step-wise increase in O_2 from the Archean through the Phanerozoic (Lyons et al., 2014). The presence of mass-independent fractionation of sulfur isotopes in sediments prior to 2.45 Ga is interpreted as pO_2 less than 10^{-5} PAL (Farquhar and Wing, 2003). The disappearance of this signal, in addition to the loss of pyrite and redox-sensitive metals in paleosols, and appearance of Fe(III)-rich sandstones mark a phase of increasing O_2 known as the Great Oxidation Event (Canfield, 2004; Holland, 2002, 2006). This period is coincident with numerous large igneous provinces (Ciborowski and Kerr, 2016; Marty et al., 2019) and large-scale glaciations (Gumsley et al., 2017; Zakharov et al., 2017). Oxygen levels during this period are thought to have increased up to 0.1 PAL (Lyons et al., 2014). At 2.06 Ga, a global carbon isotope excursion, known as the Lomagundi isotope excursion, marked high rates of organic carbon burial, and a subsequent precipitous drop to low pO_2 over most of the Proterozoic (Hodgskiss et al., 2019; Schidlowski et al., 1976). Planavsky et al. (2014)

established an upper limit of 0.01 PAL over the Mesoproterozoic based on the Cr isotope record of paleosols and near-shore sediments. This estimate is based on the pO_2 required to oxidize Mn^{2+} given a standard fluid-soil residence time, as manganese oxides are considered the only environmentally relevant abiotic oxidants of Cr(III). Prior to 0.8 Ga, or the initiation of Neoproterozoic Oxidation Event, the Cr isotope record did not deviate from average crustal values, indicating minimal redox cycling and isotopic fractionation. Non-crustal Cr isotope values at the Neoproterozoic Oxidation Event point to O_2 rising to levels above 0.01 PAL (Planavsky et al., 2014), closely followed by the appearance of Ediacaran biota (Droser and Gehling, 2015).

Recent studies show that this secular increase in pO_2 is not without complications. There are several lines of evidence for transient increases in O_2 a half billion years prior to the Great Oxidation Event (Anbar et al., 2007; Crowe et al., 2013; Duan et al., 2010). These studies are based on observations of Cr, Mo, and U isotopic fractionation deviating from crustal values in paleosols or shales. As Lalonde and Konhauser (2015) argue though, some of these signals in paleosols may reflect local O_2 production from microbial mats.

The Cr isotope evidence for low Mesoproterozoic pO_2 has been interrogated more extensively. In 1.4 Ga near-shore sediments, Zhang et al. (2016) recorded trace metal enrichment and the presence of biomarkers that were interpreted to reflect eukaryotic diversification. Other explorations of individual formations in shallow marine settings show small episodes of oxygenation at 1.4 Ga and 1.1 Ga (Canfield et al., 2018; Diamond and Lyons, 2018; Gilleaudeau et al., 2016; Kendall et al., 2009). To complicate the Cr isotope proxy further, non-redox processes, such as ligand-promoted dissolution, have been recognized as potentially important isotope fractionating processes of Cr isotopes (Saad et al., 2017). In the wake of these new studies, more in-depth examinations of the Cr isotope record in shales and paleosols have been published (Cole et al., 2018; Cole et al., 2016; Colwyn et al., 2019). These studies still indicate that pO_2 levels were low prior to the Neoproterozoic Oxidation Event at 0.8 Ga.

Improving the constraints on the atmospheric O_2 record requires the development of more proxies sensitive to different levels of O_2 in diverse environmental settings. In particular, concentrations and isotope measurements of a range of redox-sensitive elements in paleosols and near-shore sediments could improve interpretations of redox conditions in individual formations. Here, we examined the novel tellurium (Te) stable isotope system as a candidate for such a paleoredox proxy. Prior to the increase of appreciable pO_2, Te should be present as Te(0), trace tellurides in sulfide phases, or telluride minerals (Wang and Becker, 2013; Yierpan et al., 2018). Like Cr or U isotopes, isotopic fractionation would be initiated when the oxidation of reduced, insoluble phases occurred, and Te(IV) and Te(VI) could undergo reduction and adsorption. This "oxidative threshold" occurs at conditions more reducing that the transition of Cr(III) to Cr(VI) (Figure 5.1). Therefore, Te isotopes should be more sensitive to the appearance of oxidizing conditions than Cr and may provide new constraints on Precambrian pO_2. Te isotopes may also be less sensitive than other paleoredox proxies, like U isotopes, which track whiffs of O_2 prior to the GOE. Here, we examine this premise using Te concentration and isotope data in paleosols and ironstone formations ranging from 3.0 to 0.016 Ga.

Tellurium is a metalloid with 4 oxidation states, -II, 0, IV, and VI. As a reduced species, Te(0) is extremely insoluble relative to Te(IV) and Te(VI), which form soluble oxyanions, H_2TeO_3, $HTeO_3^-$, H_2TeO_4, and $HTeO_4^-$ (McPhail, 1995). Tellurium isotopes ($\delta^{130/26}$Te) have been shown to fractionate in a variety of laboratory studies. Biological and abiotic reduction of Te(IV) and Te(VI) results in a difference between the instantaneous reduced product and reactant of up to 4‰ (Baesman et al., 2007; Smithers and Krouse, 1968). Adsorption to goethite and illite at circumneutral pH produces an equilibrium isotope effect of ~0.20‰ for Te(IV) to illite and goethite, ~0.30‰ for Te(VI) to illite and 0.65‰ for Te(VI) to goethite (Wasserman, in prep).

5.2 Methods and Materials

5.2.1 Samples

All samples were obtained from the Department of Earth and Planetary Sciences at Yale University (New Haven, CT) and are characterized in the references provided in Table 5.1. Tellurium, Fe, and Ti concentrations were measured in twelve paleosols. Due to low Te concentrations and limited sample mass, Te isotopes were measured in samples from eight of these paleosols. These paleosols are all derived from igneous rocks, except for the Olive Hill formation, which is developed on shale (Table 5.1) (Smyth, 1984). None of the paleosols are subject to significant grades of metamorphism (Colwyn et al., 2019). Therefore, non-fractionated Te isotope values should reflect crustal $\delta^{130/126}$Te (see Results).

Six ironstone formations were measured for Te concentrations and isotopes. Ironstones, as described by Planavsky et al. (2014), are near-shore sandy or sility, iron-rich sedimentary units. They are unlike banded iron formations, which do not occur in the Phanerozoic, and are found in shallower marine environments. The ironstones are made up of cemented Fe-rich oolitic grains, that consist of usually concentric hematite coatings around a sand or silt matrix. As Te is quickly scavenged in the marine water column (Lee and Edmond, 1985), the ironstone formations would be an important sink of continental fluxes of Te. In addition, these deposits are not located close to hydrothermal activity (Planavsky et al., 2014), so little contribution from hydrothermal sources of Te would be present.

5.2.2 Sample preparation and mass spectrometry

Digestion and measurement procedures of samples followed methods described in Wasserman and Johnson (2020b). For concentration measurements, powdered samples were weighed and digested using in 4 or 8 mL of reverse aqua regia for 24 hours. A small aliquot of the sample was dried down and re-dissolved in 5% (v/v) HNO_3 for measurement by a Thermo iCAP Q ICP-MS. Sample preparation for Te isotope measurements involved the addition of ^{120}Te-^{124}Te double spike to correct for isotopic fractionation during sample preparation and drifts in instrumental mass bias. Matrix and isobaric interferences (Fe, Sn, Sb) were separated from Te using previously described anion-exchange procedures (Wasserman and Johnson, 2020b). Briefly, Te in the sample was reduced to Te(IV) in 6 M HCl and loaded on a 3 mL anion exchange column. Iron, antimony, and the majority of the matrix were removed using an HCl-HF mixture and Te was eluted in 1 M HNO_3. Tellurium was purified from Sn, an isobaric interference, using a second anion exchange column. After oxidation of the sample using 0.02 M $K_2S_2O_8$, the sample was loaded onto a column with 1 mL AG1-X8 (100-200 mesh) resin. In low molarity HCl, Te(VI) was eluted while Sn remained on the column. Samples were then dried down and re-dissolved in 5 M HCl, after which the sample was reduced to Te(IV) and diluted to 2 M HCl with Milli-Q H_2O. Concentrations were measured on the iCAP Q ICP-MS. During concentration measurements, online addition of ^{115}In and ^{73}Ge were used as internal standards to correct for matrix effects on signal suppression or enhancement. The limit of quantification for Te, Fe, and Ti is 0.2, 0.4. and 0.2 ng g^{-1}.

Tellurium stable isotope measurements were made on a Nu Plasma (Nu Instruments, UK) Multi-Collector Inductively Coupled Plasma Mass Spectrometer (MC-ICP-MS) at the University of Illinois at Urbana-Champaign. An in-house hydride generation system was used for a sample introduction system coupled to the MC-ICP-MS. Through on-line addition, the sample in 4 M HCl was reacted with a solution of 0.2% (w/v) $NaBH_4$ and 0.2% (w/v) NaOH, converting Te(IV) to $H_2Te_{(g)}$ which was carried in an Ar stream into the plasma. All Te isotopes were monitored using Faraday cups including masses 118 and 132. A "blank" 4 M HCl solution was measured prior to the sample for on-peak background subtraction. Additional subtractions of Sn, Xe, $^{123}SbH^+$, and TeH^+ interferences were accomplished by monitoring ^{118}Sn, ^{132}Xe, and assuming a constant ratio of hydride formation. An iterative routine of data reduction allowed for the correction of interferences and extraction of the natural isotope ratio from the spike-sample mixture. We report isotope values using ^{130}Te and ^{126}Te, following discussion in Wasserman and Johnson (2020). This is expressed using delta notation (‰) or:

$$\delta^{130}Te = [\frac{^{130}Te/^{126}Te_{sample}}{^{130}Te/^{126}Te_{standard}} - 1] * 1000 \qquad (5.1)$$

Sample Te isotope ratios were subtracted from the ratio of NIST SRM 3156 (lot no. 140830), which bracketed every 4 samples. A secondary standard of dissolved Alfa Aesar Te(VI) powder (lot no. Y05A029) was measured every ten samples to ensure a consistent offset of 0.84‰ relative to NIST SRM 3156. Duplicates of six paleosol and five ironstone samples showed average uncertainties of 0.15‰ and 0.17‰ (2σ) respectively, using a root-mean-square method based off Hyslop and White (2009).

5.3 Results

5.3.1 Concentrations and enrichment or depletion during weathering

Tables 5.3 and 5.4 show the range of concentrations of Te, Fe, and Ti and ratios of Te and Fe relative to, the immobile elements, Ti in paleosols and ironstone formations. For paleosol samples, Te concentrations range from below limit of detection (0.05 ng g^{-1}) to 200 ng g^{-1} in CLRD-0.75. The average concentrations of Te are variable among the paleosol formations. For example, the Lauzon Bay paleosol and the Cooper Lake paleosol were deposited at the same time (2.45 Ga), but Te concentrations are ten times greater in the Cooper Lake paleosol. Ironstone formations contain on average higher concentrations of Te than the paleosols and show no variation with time (Table 5.4).

Normalization to the conservative element, Ti, can give some indication of elemental enrichment or depletion in paleosols (Cole et al., 2017). As Ti is considered to be relatively immobile, high Te/Ti or Fe/Ti ratios, relative to the unweathered parent rock, point to processes that concentrate Te in the solid (i.e. reduction or adsorption processes). Conversely, relatively low ratios suggest mobilization and removal of Te or Fe. In the paleosols, elemental enrichment or loss during weathering can also be examined relative to the parent material using a chemical mass balance model assuming no bulk density changes in the profile (Brimhall and Dietrich, 1987). We calculated the unitless elemental mass balance coefficient, τ, for Te and Fe as follows:

$$\tau_{i,j} = \frac{C_{i,p} C_{j,w}}{C_{i,w} C_{j,p}} - 1 \tag{5.2}$$

In this equation, C represents concentration, where subscripts i and j denote the immobile and mobile elements, respectively, and subscripts p and w denote the parent rock and the weathered host rock, respectively. Here, we use Ti as the immobile element and Te is the potentially mobile element of interest. Samples representative of the unweathered parent rock are indicated in Table 5.3 for the calculation of $\tau_{\mathrm{Te,Ti}}$. Values close to zero signify no loss nor gain of Te from the parent rock, while negative and positive values show loss and gain respectively (Brimhall and Dietrich, 1987). $\tau_{i,j}$ were calculated for seven of the twelve paleosols examined in this study. For the remainder of the paleosols, no parent rock sample was available. Although the data are sparse, average depth-weighted $\tau_{\mathrm{Te,Ti}}$ appear to decrease over time, from the Archean to the Phanerozoic (Table 5.3). The pre-GOE samples from the Nsuze, Carletonville, and Black

Reef paleosols show a range of $\tau_{i,j}$ indicating Te enrichment to slight loss. At the GOE, the Lauzon Bay and Cooper Lake paleosols display gains of Te. The Phanerozoic Verde River and Olive Hill paleosols both show, on average, negative $\tau_{Te,Ti}$.

Given the strong adsorption affinity of Te(IV) and Te(VI) to Fe-(oxy)hydroxides (Hayes and Ramos, 2019; Kashiwabara et al., 2014a; Qin et al., 2017), the comparison of Te/Ti and Fe/Ti should give some indication if the Fe weathering cycle is correlated to Te mobility (Tables 5.3, Figure 5.2). Pre-GOE paleosols tend to have higher Fe/Te and lower Te/Ti on average than GOE and Phanerozoic samples. However, overall, there is little correlation between Te and Fe retention in paleosols (Figure 5.2).

5.3.2 Te isotopic fractionation

We estimate the range in average crustal $\delta^{130/126}$Te to be 0.06 to 0.26‰. This range is based on the range in $\delta^{130/126}$Te the carbonaceous chondrite Orgueil, which showed little evidence of metamorphism compared to other chondrites (Fehr et al., 2018). Isotopic measurements of USGS standard BCR-1 and BHVO-2 fall within this range (0.25 ± 0.18‰ and 0.15 ± 0.18‰), suggesting that the contribution from mantle sources to the average crustal $\delta^{130/126}$Te overlaps with chondritic values. Other studies (Toth, 2019) have reported that the bulk silicate earth isotopic composition agrees with Te isotope measurements of carbonaceous chondrites from Fehr et al. (2018). However, further investigations of crustal $\delta^{130/126}$Te variability should be done to confirm the validity of this range.

The $\delta^{130/126}$Te of the measured paleosols and ironstones ranges from -0.42 to 1.52‰ (Tables 5.5 and 5.6, Figure 5.3). Prior to the GOE (>2.45 Ga), $\delta^{130/126}$Te of paleosols falls within the range of crustal values. Samples deposited after the GOE are isotopically similar to, or slightly heavier than, the crustal range. Mesoproterozoic ironstones show a ~1‰ spread, where most samples plot at crustal values or lower. The largest range in $\delta^{130/126}$Te occurs in the Phanerozoic paleosols and ironstones, where the paleosols are all isotopically heavier than average crust and the ironstones are all at the upper end of the crustal range.

5.4 Discussion

5.4.1 Paleosols

Examination of $\tau_{Te,Ti}$ in paleosols (Table 5.3) shows no weathering loss of Te during the Archean, but significant loss in Phanerozoic samples. We attribute this to increased oxidative weathering and export of Te(IV) and Te(VI) oxyanions after the Great Oxidation Event. Meanwhile, the net enrichment of Te in the paleosols deposited prior to and at the onset of the GOE could be the product of limited oxidative weathering, where Te is remobilized, then concentrated via reduction or adsorption at certain points within the weathering profile. Indeed, others have noted an enrichment of U from the Cooper Lake paleosol suggesting that oxidation and subsequent reduction must have occurred (Babechuk et al., 2019; Colwyn et al., 2019).

Environmental Te mobility is related to the Fe redox cycle, in addition to the redox state of the Te itself. In mine tailings and modern soils, the majority of oxidized Te is associated with Fe-(oxy)hydroxides and to a lesser extent, clay minerals (Hayes and Ramos, 2019). Results of EXAFS spectra indicate that Te(VI) can also co-precipitate on ferrihydrite providing a long–term sink of the oxyanion (Kashiwabara et al., 2014a). Therefore, the formation of oxidized Fe phases, or higher Fe/Ti, could limit the flux of Te from the continents even when conditions are oxidizing enough to convert most Te to Te(VI) during weathering.

The relationship between Te and Fe in the paleosols is not straightforward. Paleosols deposited prior to the GOE and during the GOE show conservative or slightly enriched behavior. In Phanerozoic paleosols, $\tau_{Te,Ti}$ is negative for the Verde River and Olive Hill paleosols showing overall loss (Table 5.3). However, Fe/Ti values are lower in the Phanerozoic paleosols than in the pre-GOE paleosols, which is the opposite trend than expected for Te adsorption by Fe-(oxy)hydroxides. While it appears that Fe does not entirely control Te mobility, adsorption to Fe-(oxy)hydroxides and clay minerals could be a sink for most of the Te oxidized in these paleosols, as has been observed in modern studies (Qin et al., 2017). This is supported by the fact that $\tau_{Te,Ti}$ values do not show complete loss of Te from the Phanerozoic paleosols suggesting that oxidized Te may not be as mobile as other redox-sensitive elements.

Tellurium isotopes in paleosols indicate that oxidative mobilization occurred during the Great Oxygenation Event. The Cooper Lake paleosol (2.45 Ga) and Karelia paleosols (2.35 - 2.2 Ga) are slightly heavier than the crustal range (Table 5.5, Figure 5.3). These deviations from the crustal range are small but significant and may reflect limited mobilization and concentration, via reduction, of Te within the paleosol. Isotopic fractionation due to oxidative weathering and adsorption or redox cycling is clearly visible in the Phanerozoic samples. In samples younger than 2.35 Ga, all of these excursions outside the range of unaltered crust are isotopically heavy (Figure 5.3). In addition, in the Cooper Lake and St. Francois paleosols, $\delta^{130/126}$Te increased at shallower depths (Table 5.5).

While it is difficult to identify the fractionating processes simply based on the available data, multiple cycles of reduction and re-oxidation, or adsorption and desorption of Te could drive $\delta^{130/126}$Te either higher and lower values. In the case of reduction, as oxidized Te- bearing groundwater enters more reducing parts of the paleosol, isotopically light Te(0) will be precipitated. As the groundwater is reduced further, continuous reduction will drive the remaining Te(IV) and Te(VI) isotopically heavier. The reduced product will also become isotopically heavier as the water moves further into the reducing zone. This is identical to the processes responsible for the ~25‰ range observed in outcrops of the Yutangba Plateau for Se isotopes (Zhu et al., 2014). A similar process could be expected for adsorption, where continuous adsorption would drive the remaining groundwater isotopically heavy, leaving the adsorbed pool would be isotopically light. Given this behavior, a reservoir of isotopically light Te should be present within the outcrop. However, the measurements in this study, given our limited sample size, have not captured this pool so far.

5.4.2 Ironstones

Higher Te concentrations in the ironstone samples compared to paleosols provide evidence for the increased weathering flux of soluble Te oxyanions to the shallow ocean during the Proterozoic. To address whether isotopic fractionation in the ironstone samples is of an authigenic or detrital origin, we examined the patterns of Te in the ironstones relative to paleosols (Figure 5.4A). In this archive, decreases and increases in Te/Ti represent the variations in the detrital and authigenic contributions of Te due to oxidative weathering. Higher Te/Ti positively correlates with total Te in the ironstones (Figure 5.4A). The enrichment of Te, therefore, represents a higher authigenic incorporation of soluble Te.

Tellurium is most likely associated with the hematitic ooids as opposed to the cements in these formations, as a there is a strong correlation between elevated Te/Ti and Fe/Ti (Table 5.4). The ironstones examined here show evidence of minimal post-depositional alteration and recrystallization (Planavsky et al., 2014). Therefore, Te concentrations and isotopic fractionation should be reflective of processes at the time of deposition. Other studies have also noticed enrichments of Te in Proterozoic marine sediments. Parnell et al. (2018) reported up to 32 ppm of Te in reduction spheroids of the red beds in the Mesoproterozoic Belt Supergroup. Similarly, in black shales, higher Te concentrations are observed in sedimentary pyrite during the

Mesoproterozoic and Neoproterozoic relative to crustal Te concentrations (Armstrong et al., 2018; Large et al., 2015). Given these observations, Te enrichment in mid-Proterozoic marine sediments may be indicative of active Te oxidative weathering.

Tellurium isotopic fractionation in samples from Proterozoic and Phanerozoic ironstone formations represents a combination of authigenic processes (i.e., adsorption and reduction) and the changing $\delta^{130/126}$Te of waters draining the continents (Figure 5.3). The comparison of $\delta^{130/126}$Te and Te/Ti can give some indication if detrital input or authigenic processes are controlling Te isotopic fractionation (Figure 5.4B). As there is no difference in trends between the suite of Phanerozoic samples versus Proterozoic samples, it is plausible that similar processes must be controlling the Te isotope values in oxic Phanerozoic samples as in the mid-Proterozoic ironstones.

If atmospheric O_2 was not sufficiently high to oxidize Te(0), reduced detrital phases would not deviate from crustal $\delta^{130/126}$Te values. When oxidative weathering is active, the riverine flux of Te to the oceans should be isotopically heavy, as adsorption and reduction both result in enrichment of the lighter isotopes into the immobilized product. However, adsorption of Te oxyanions on the precursor Fe(III)-oxyhydroxides can also induce isotopic fractionation. At isotopic equilibrium, Te(VI) adsorption to goethite can result in a ~0.65‰ enrichment in the aqueous phase relative to the adsorbed phase (Wasserman, in prep). This could drive the $\delta^{130/126}$Te of adsorbed Te to lighter values as observed in closed systems, or to heavier values if open system behavior allowed for continuous partial adsorption along a reaction path. Therefore, high $\delta^{130/126}$Te could be reflective of isotopically heavy detrital input and open-system adsorption behavior, while sub-crustal $\delta^{130/126}$Te points to closed-system adsorption processes.

5.5 Implications and future directions

Taken together, $\tau_{Te,Ti}$ and isotopic data in paleosols and ironstone formations provide evidence for an active post-GOE Te redox cycle. This study adds to increasing evidence that large scale changes in atmospheric pO_2 controlled the mobility of redox-sensitive elements and isotopic fractionation in the geologic record (Brüske et al., 2020; Greaney et al., 2020) The $\delta^{130/126}$Te of paleosols and ironstone formations suggest that, as shown in Figure 5.1, Te oxidation is more sensitive to pO_2 than Cr and possibly similarly or less sensitive than U. However, this is based on simple thermodynamic data, which does not take into account strong complexation of U and Te in natural waters. The precise redox threshold of Te relative to U should be examined more in depth in future studies of the Te paleoredox proxy (Missen et al., 2020).

Mesoproterozoic ironstone formations show evidence of Te enrichments and isotopic fractionation, which we interpret to be a result of oxidative weathering. Although pO_2 during the Mesoproterozoic (<0.001-0.01 PAL) is thought to be lower than levels at the GOE (Planavsky et al., 2014), environmental O_2 must have been high enough for redox cycling of Te to continue. In sedimentary pyrite in marine black shales, Large et al. (2015) noted that Te is elevated prior to the GOE and then decreases from the Paleoproterozoic through the Mesoproterozoic. The authors note that low concentrations of this metalloid seem to correlate with the deposition of banded iron and ironstone formations. This suggests ironstones are an important archive of Te in marine settings, and that Te enrichments in these formations during the Mesoproterozoic could be indicative of oxidative weathering.

While the results of this limited dataset show that the Te isotope system tracks variations in environmental redox conditions, the addition of more samples representative of various depositional environments could elucidate the sensitivity of this proxy. In particular, in order to confirm that the Te data in ironstones reflects oxidative weathering, additional records of Te weathering should be examined from the mid-Proterozoic. Tellurium isotope measurements of detrital pyrite in Precambrian marine shales could help identify a detrital sediment endmember, which could identify the authigenic contribution during ironstone formation. In addition, the inclusion of mid-Proterozoic paleosols in this dataset would help validate the interpretation of our results.

5.6 Conclusions

The results of this study show the first use of Te isotopes to examine low-temperature Te mobility as a function of rising pO_2 over the Precambrian and Phanerozoic. Similar to Cr and U isotopes, the Te isotope paleoredox proxy shows binary behavior in paleosols and ironstone formations. Prior to the rise of oxygen at 2.45 Ga, Te isotope values lie within the range of average crustal $\delta^{130/126}$Te. After this period, the shift of $\delta^{130/126}$Te to outside the range inferred for average earth crust shows the initiation of active Te redox cycling. Future investigations of Te(0) oxidation kinetics can determine the relative sensitivity of the Te paleoredox proxy to pO_2. While this study does not establish new constraints on atmospheric O_2 over time, it does add to existing evidence for the presence of (1) appreciable levels of O_2 during the GOE, (2) sufficient Mesoproterozoic O_2 to maintain Te oxidative weathering, and (3) very active Te redox cycling under Phanerozoic pO_2.

5.7. Tables and Figures

Table 5.1. Age and description of the paleosols measured in this study.

Formation	Time (Ga)	Parent Material	Upper and Lower Age Constraint (Ga)	References
Basal Pongola Paleosol (SA)*	3	Archean felsic gneiss	3.105 ± 0.003; 2.98 ± 0.01	Grandstaff et al. (1986), Kimberley and Grandstaff (1986), Mukasa et al. (2013), Wilson and Zeh (2018)
Nsuse Paleosol (SA)*	2.97	Nsuze group basaltic andesite	2.968 ± 0.006; 2.954 ± 0.009	Crowe et al. (2013), Wilson and Zeh (2018), Delvigne et al. (2016)
Carletonville Paleosol (SA)*	2.9	Crown Formation Lava	2.914 ± 0.004; 2.714 ± 0.008	Robb and Meyer (1990, 1995)
Mt. Roe Paleosol (AUS)	2.76	Mt. Roe Basalt	2.78; 2.76	Rye and Holland (2000)
Black Reef (Delmas) Paleosol (SA)	2.7	Hydrothermally altered granite	2.785 ± 0.002; 2.550	Maynard et al. (1995)
Karelia Paleolols (FIN)*	2.2 - 2.7	Various substrates: Archaean granitoids, lower Proterozoic glacial rock	2.7; 2.2	Marmo (1992), Hanski and Melezhik (2013); Strand and Laajoki (1993)
Cooper Lake Paleosols (CAN)*	2.4-2.45	Quartzite intruded by mafic dike	2.475; 2.4525 ± 0.0062	Babechuk et al. (2019); Ketchum et al. (2013); Rasmussen et al. (2013); Rye and Holland (1998); Sutton and Maynard (1993); Utsunomiya et al. (2003)

Table 5.1 (cont.)

Formation	**Time (Ga)**	**Parent Material**	**Upper and Lower Age Constraint (Ga)**	**References**
Lauzon Bay Paleosol (CAN)	2.4	Algoman Granite	2.5, 2.475	Sutton and Maynard (1992), Maynard et al. (2013); Rasmussen et al. (2013), Babechuk et al. (2019)
Verde River Paleosol (USA)*	0.52	Payson Ophiolite basalts	1.729 +/- 0.006; Early Cambrian	Colwyn et al. (2019)
St. Francois Mts Paleosol (USA)*	0.5	Granite	1.4-1.3; Late Cambrian	Colwyn et al. (2019); Sutton et al. (1996);
Olive Hill Paleosol (USA)*	0.323	Upper Mississippian Pennington, Borden, and Newman Formation shale	Carboniferous biostratigraphy	Smyth (1984)
Lago Posadas Paleosol (ARG)*	0.016	Santa Cruz Formation tuff	0.0022; 0.0014	Blisniuk et al. (2005)

*Formations measured for $\delta^{130/126}$Te

Table 5.2. Age and references for ironstone formations examined in this study.

Formation	**Time (Ga)**	**Upper and Lower Age Constraints**	**References**
Chuanliggou Ironstone (CHN)	1.70	1.731 +/- 0.004; 1.673+/- 0.01	Peng et al. (2012), Planavsky et al. (2014)
Freedom Ironstone (USA)	1.65	1.71; 1.63	Holm et al. (1998), Medaris et al. (2003)
Sherwin Ironstone (AUS)	1.45	1.492+/- 0.004; 1.429+/- 0.031;	Jackson et al. (1988); Kralik (1982)
Cap de la Che'vre Ironstone (FRA)	0.46	0.465+/-.001	Planavsky et al. (2014); Robardet et al. (1994)
Red Mountain Ironstone (USA)	0.44	Rhuaddanian (0.4438 +/- 0.0015; 0.4408 +/- 0.0012)	Chowns et al. (2015)
Rashby Ironstone (ENG)	0.18	ND	Planavsky et al. (2014)

Table 5.3. Concentrations of Te, Fe, and Ti and $\tau_{(Te,Ti)}$ for paleosols. Depth-weighted average $\tau_{(Te,Ti)}$ are bolded and italicized.

Formation	**Time (Ga)**	**Sample ID**	**Te (ng g^{-1})**	**Fe (wt. %)**	**Ti (wt. %)**	**Te/Ti**	**Fe/Ti**	**τ (Te, Ti)**
Basal Pongola Paleosol	3	92.6(1)	11.1	4.66	0.16	7.08E-06	29.6	
		92.8(1)	BLD	5.43	0.14	2.08E-08	37.7	
Nsuze Paleosol	2.97	WM 08	4.3	0.21	0.45	9.62E-07	0.5	-0.63
		WM11	7.5	5.04	0.15	5.10E-06	34.4	0.98
		WM 12	0.1	6	0.1	4.89E-08	58.6	-0.98
		WM13	4.8	6.28	0.11	4.23E-06	54.9	0.64
		WM14	0.1	5.91	0.1	2.99E-08	58.9	-0.96
		WM15	0.1	4.42	0.08	3.73E-08	55	-0.95
		WM16*	1.8	5.51	0.07	2.58E-06	79.9	***-0.30***
Carletonville Paleosol	2.9	DN6 11.83.9/1184 W.C	13.8	2.75	0.31	4.51E-06	9	1.02
		DN6 1185.8	9.52	4.19	0.29	3.24E-06	14.3	0.45
		DN6 1186.2	9.11	6.12	0.38	2.40E-06	16.1	0.08
		DN6 1188.3*	4.59	2.37	0.21	2.23E-06	11.5	***0.51***
Mt. Roe Paleosol	2.76	Pi10214	0.4	3.48	0.27	1.35E-07	13	
		Pi10204	0.8	1.15	0.31	2.49E-07	3.7	
Black Reef Paleosol	2.7	BH155	20.24	3.54	0.2	1.01E-05	17.7	1.55
		BH155-0.15	13.44	0.62	0.23	5.84E-06	2.7	0.47
		BH155-0.75	13.39	1.2	0.4	3.35E-06	3	-0.16
		BH155-3.3	30.7	2.06	0.4	7.66E-06	5.2	0.93
		BH155-9.95	5.3	2.03	0.32	1.66E-06	6.3	-0.58
		BH155-55.3*	26.63	4.73	0.67	3.97E-06	5.15	***0.63***
Karelia Paleolols	2.7	10401a	7	3.91	ND	ND	ND	
		10401b	9	3.51	ND	ND	ND	
		10401e	11	0.79	0.28	3.94E-06	2.8	
	2.35	6105a	5.5	1.62	0.34	1.60E-06	13.4	
	2.2	205e	10.2	1.58	0.12	8.71E-06	4.8	
Cooper Lake Paleosols	2.4	CLRD-0.75	202.2	1.38	0.42	4.79E-05	3.3	0.49
		CLRD-3.0	41.9	3.1	0.48	8.72E-06	6.4	-0.73
		CLRD-3.5*	72.3	5.08	0.23	3.21E-05	22.5	***0.11***
		CLW-2.5	12.8	1.07	0.02	7.77E-05	6.5	1.90
		CLW-3.5	5.7	0.1	0.02	2.63E-05	4.7	-0.02
		CLW-4.5*	9.5	0.08	0.04	2.68E-05	2.3	***0.43***

Table 5.3 (cont.)

Formation	**Time (Ga)**	**Sample ID**	**Te**	**Fe**	**Ti**	**Te/Ti**	**Fe/Ti**	**τ (Te, Ti)**
Lauzon Bay Paleosol	2.4	L4	3.2	0.11	0.01	3.17E-05	11	0.26
		L5	1.3	0.34	0.06	2.20E-06	5.7	-0.91
		L7	1.3	0.25	0.02	6.55E-06	12.5	-0.74
		L8	15.4	0.23	0.02	7.68E-05	11.5	2.05
		L11	4.1	0.3	0.03	1.38E-05	10	-0.45
		L12*	7.6	0.36	0.03	2.52E-05	12	***0.32***
Verde River Paleosol	0.52	VR1E0	41.3	0.97	0.59	6.99E-06	1.6	-0.37
		VR1E5	1.8	0.97	0.58	3.11E-07	1.7	-0.97
		VR1E50	6.2	1.24	0.37	1.67E-06	3.4	-0.85
		VR100C	81.3	1.68	7.88	1.03E-06	0.2	-0.91
		VR1600	15.9	0.68	0.32	4.98E-06	2.1	-0.55
		VR1 2800*	30.9	0.63	0.28	1.11E-05	2.3	***-0.44***
St. Francois Mts Paleosol	0.5	SF589	9	0.49	0.09	9.84E-06	5.4	
		SF590	9	0.59	0.09	9.90E-06	6.5	
		SF598	4	0.36	0.05	9.45E-06	7.5	
Olive Hill Paleosol	0.323	OHC-0.01	63	7.19	1.89	3.33E-06	3.8	-0.93
		OHC-0.2	150.2	1.41	1.52	9.88E-06	0.9	-0.8
		OHC-1.0	124.3	7.5	0.91	1.37E-05	8.2	-0.72
		OHC-2.2	120.8	6.41	1.14	1.06E-05	5.6	-0.78
		OHC-8.5	51.1	1.27	0.36	1.42E-05	3.5	-0.71
		OHC-10.0*	194.5	0.89	0.4	4.86E-05	2.2	***-0.77***
Lago Posadas Paleosol	0.016	14P40	44	ND	ND	ND	34.4	
		14P1	41.5	ND	ND	ND	58.6	

*Sample representative of parent material. The Cooper Lake paleosol has two protoliths.

Table 5.4. Concentrations of Te, Fe, and Ti for ironstone samples.

Formation	**Time (Ga)**	**Sample ID**	**Te (ng g^{-1})**	**Fe (wt. %)**	**Ti (wt. %)**
Chuanliggou Ironstone	1.7	CLG-6-1	16.7	48.20	0.01
		CLG-6-3-2	32.2	ND	0.01
Freedom Ironstone	1.65	H-28-B	65.0	27.00	0.12
		H-22-2	171.3	30.40	0.04
Sherwin Ironstone	1.45	RR01-1	199.6	51.00	0.01
		RR05-1	126.0	49.30	0.01
		S8	232.7	50.20	0.03
		S-13	230.8	49.90	0.05
		Sherwin S-10	225.7	55.20	0.01
		S-8-2	161.3	50.20	0.06
Cap de la Che'vre Ironstone	0.46	FIRS-2	6.9	42.90	0.17
Red Mountain, USA Ironstone	0.44	BF-CP-4	105.4	27.60	0.10
		BF-RM-1	480.0	42.60	0.09
		BF-RM-7	67.3	15.20	0.06
		BF-RM-12	150.70	42.6	0.09
Rashby Ironstone	0.18	RI-1	241.0	10.30	0.40

Table 5.5. $\delta^{130/126}$Te of selected samples from paleosol formations.

Paleosol Formation	**Time (Ga)**	**Sample**	$\delta^{130/126}$Te **(‰)**	**2σ**
Basal Pongola, Nsuze Paleosol	3	92.6(1)	0.15	0.15
Carletonville Paleosol	2.9	DN6 11.83.9/1184 W.C	0.14	0.15
Karelia Paleolols	2.7	10401e	-0.07	0.15
	2.35	6105a	0.29	0.15
	2.2	205e	0.46	0.15
Cooper Lake Paleosols	2.4	CLRD-0.75	0.37	0.15
		CLRD-3.0	0.43	0.13
		CLRD-3.5	0.28	0.13
		CLW-3.5	-0.01	0.15
		CLW-4.5	0.12	0.15
Verde River Paleosol	0.52	VR1E0	0.52	0.15
		VR100C	1.09	0.15
St. Francois Mts Paleosol	0.5	SF589	1.52	0.15
		SF590	1.11	0.15
		SF598	0.48	0.15
Olive Hill Paleosol	0.323	OHC-0.01	0.78	0.11
		OHC-2.2	0.64	0.13
Lago Posadas Paleosol	0.016	14P40	0.82	0.16
		14P1	0.60	0.16

Table 5.6. $\delta^{130/126}$Te of selected samples from ironstone formations.

Ironstone Formation	**Time (Ga)**	**Sample**	$\delta^{130/126}$Te **(‰)**	**2σ**
Chuanliggou, China Ironstone	1.7	CLG-6-1	-0.16	0.15
Freedom, USA Ironstone	1.65	H-28-B	-0.41	0.16
		H-22-2	-0.42	0.12
Sherwin, AUS Ironstone	1.45	RR01-1	0.24	0.12
		RR05-1	0.03	0.08
		S8	0.50	0.10
		S-13	0.10	0.10
		Sherwin S-10	0.18	0.09
		S-8-2	-0.16	0.09
Cap de la Che'vre Ironstone	0.46	FIRS-2	-0.01	0.20
Red Mountain, USA Ironstone	0.44	BF-CP-4	0.24	0.10
		BF-RM-1	0.33	0.11
		BF-RM-7	0.21	0.08
		BF-RM-12	0.23	0.09
Rashby Ironstone	0.18	RI-1	0.30	0.20

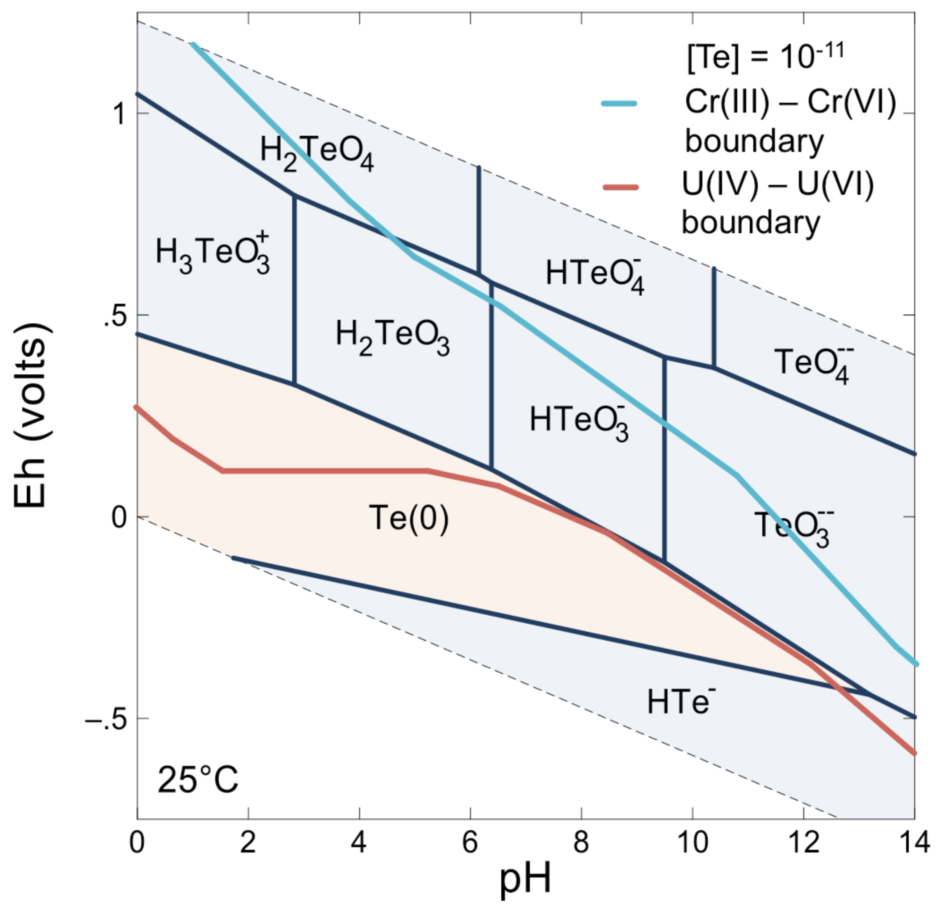

Figure 5.1. Eh-pH diagram for Te species at 25 C for [Te] $=10^{-11}$. Thermodynamic data is from McPhail (1995) and diagram was constructed using Geochemist's Workbench. Light blue and orange colors indicate aqueous and solid phases, respectively. The Cr(III)-Cr(VI) transition is denoted by the blue line, while that of the U(IV)-U(VI) transition is represented by the red line.

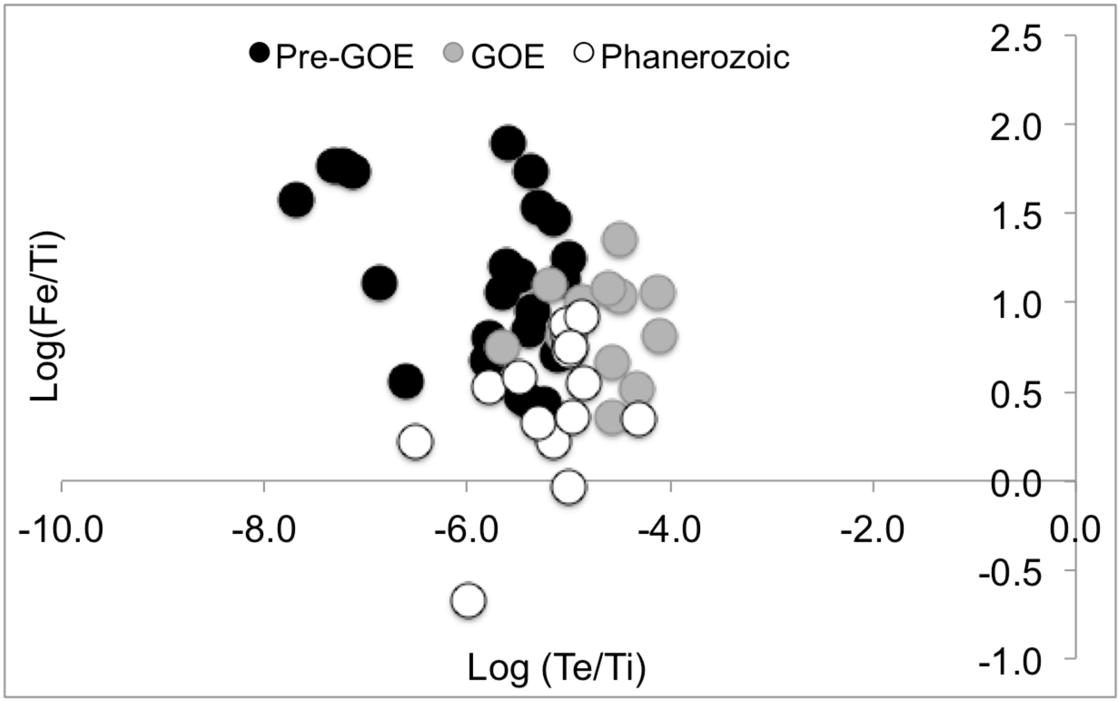

Figure 5.2. Log(Fe/Ti) over log(Te/Ti). Black, grey, and white circles denote paleosols deposited prior to the GOE, during the GOE, and after the GOE, respectively.

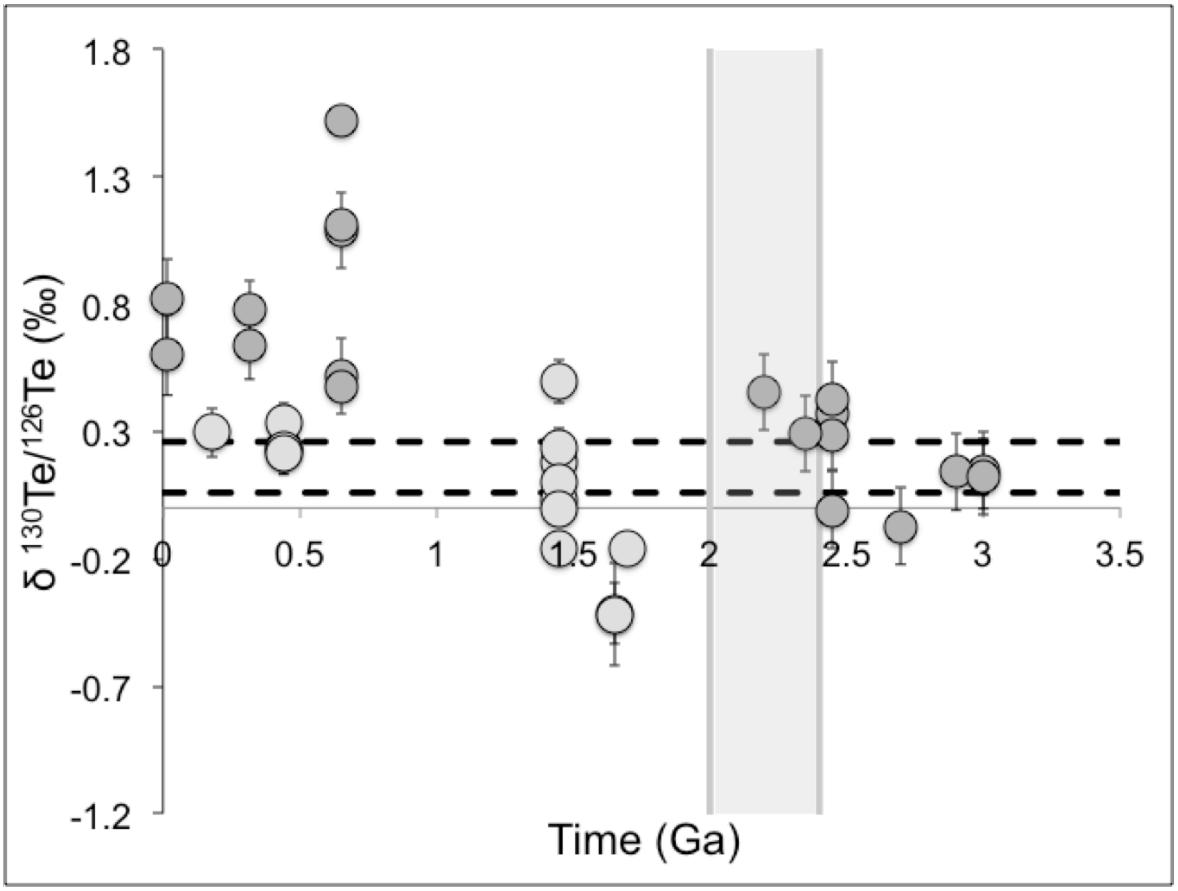

Figure 5.3. $\delta^{130/126}$Te of paleosols and ironstone formations over time. Uncertainties represent 2σ of three pairs of duplicate samples for each analytical session. Lighter grey circles show isotope values for ironstone formations, while darker grey circles represent $\delta^{130/126}$Te of paleosols. Dashed lines indicate the range of crustal Te isotope values (Fehr et al., 2018; Toth, 2019). The Great Oxidation Event is denoted by the grey band.

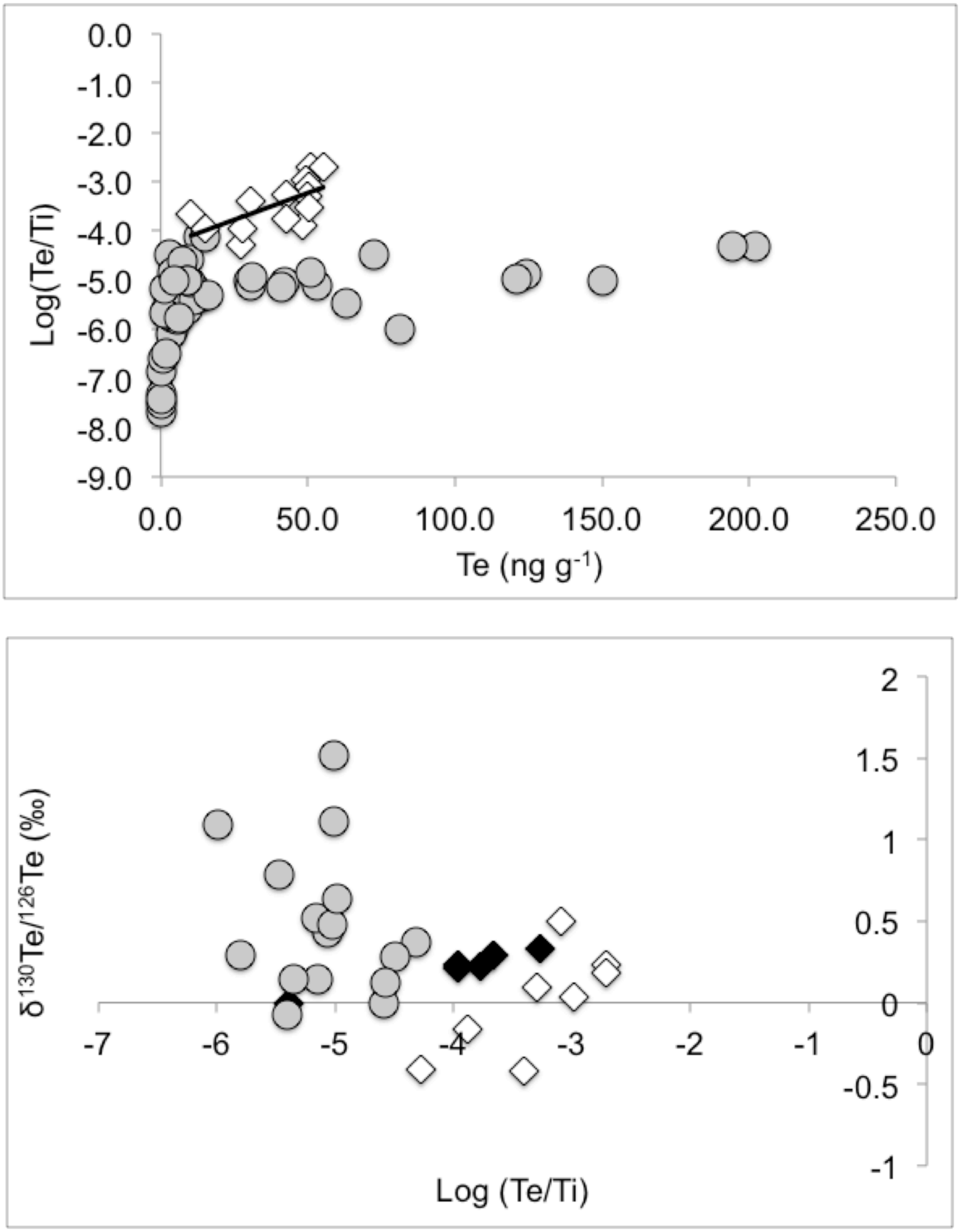

Figure 5.4. A. Enrichments of Te versus total Te concentration. Grey circles denote paleosols, while white diamonds show data from ironstone formations. Increasing Te enrichments are correlated with higher Te concentrations in ironstone formations. B. δ$^{130/126}$Te over Te enrichment in paleosols and ironstones. Grey circles represent paleosols, white and black diamonds show data for Proterozoic and Phanerozoic ironstones, respectively.

5.8. References

Anbar, A.D., Duan, Y., Lyons, T.W., Arnold, G.L., Kendall, B., Creaser, R.A., Kaufman, A.J., Gordon, G.W., Scott, C., Garvin, J. and Buick, R. (2007) A Whiff of Oxygen Before the Great Oxidation Event? Science 317, 1903.

Armstrong, J.G.T., Parnell, J., Bullock, L.A., Perez, M., Boyce, A.J. and Feldmann, J. (2018) Tellurium, selenium and cobalt enrichment in Neoproterozoic black shales, Gwna Group, UK: Deep marine trace element enrichment during the Second Great Oxygenation Event. Terra Nova 30, 244-253.

Babechuk, M.G., Weimar, N.E., Kleinhanns, I.C., Eroglu, S., Swanner, E.D., Kenny, G.G., Kamber, B.S. and Schoenberg, R. (2019) Pervasively anoxic surface conditions at the onset of the Great Oxidation Event: New multi-proxy constraints from the Cooper Lake paleosol. Precambrian Research 323, 126-163.

Baesman, S.M., Bullen, T.D., Dewald, J., Zhang, D., Curran, S., Islam, F.S., Beveridge, T.J. and Oremland, R.S. (2007) Formation of Tellurium Nanocrystals during Anaerobic Growth of Bacteria That Use Te Oxyanions as Respiratory Electron Acceptors. Appl. Environ. Microbiol. 73, 2135-2143.

Blisniuk, P.M., Stern, L.A., Chamberlain, C.P., Idleman, B. and Zeitler, P.K. (2005) Climatic and ecologic changes during Miocene surface uplift in the Southern Patagonian Andes. Earth and Planetary Science Letters 230, 125-142.

Brimhall, G.H. and Dietrich, W.E. (1987) Constitutive mass balance relations between chemical composition, volume, density, porosity, and strain in metasomatic hydrochemical systems: Results on weathering and pedogenesis. Geochimica et Cosmochimica Acta 51, 567-587.

Canfield, D.E. (2004) The Early History Of Atmospheric Oxygen: Homage to Robert M. Garrels. Annual Review of Earth and Planetary Sciences 33, 1-36.

Canfield, D.E., Zhang, S., Frank, A.B., Wang, X., Wang, H., Su, J., Ye, Y. and Frei, R. (2018) Highly fractionated chromium isotopes in Mesoproterozoic-aged shales and atmospheric oxygen. Nature Communications 9, 2871.

Chowns, T.M., Rindsberg, A.K. and Holmes, A.E. (2015) Stratigraphy and depositional environments in the Silurian Red Mountain Formation of the southern Appalachian basin, USA, Diverse Excursions in the Southeast: Paleozoic to Present. Geological Society of America, p. 0.

Ciborowski, T.J.R. and Kerr, A.C. (2016) Did mantle plume magmatism help trigger the Great Oxidation Event? Lithos 246-247, 128-133.

Cole, D.B., O'Connell, B. and Planavsky, N.J. (2018) Authigenic chromium enrichments in Proterozoic ironstones. Sedimentary Geology 372, 25-43.

Cole, D.B., Reinhard, C.T., Wang, X., Gueguen, B., Halverson, G.P., Gibson, T., Hodgskiss, M.S.W., McKenzie, N.R., Lyons, T.W. and Planavsky, N.J. (2016) A shale-hosted Cr isotope record of low atmospheric oxygen during the Proterozoic. Geology 44, 555-558.

Cole, D.B., Zhang, S. and Planavsky, N.J. (2017) A new estimate of detrital redox-sensitive metal concentrations and variability in fluxes to marine sediments. Geochimica et Cosmochimica Acta 215, 337-353.

Colwyn, D.A., Sheldon, N.D., Maynard, J.B., Gaines, R., Hofmann, A., Wang, X., Gueguen, B., Asael, D., Reinhard, C.T. and Planavsky, N.J. (2019) A paleosol record of the evolution of Cr redox cycling and evidence for an increase in atmospheric oxygen during the Neoproterozoic. Geobiology 17, 579-593.

Crowe, S.A., Døssing, L.N., Beukes, N.J., Bau, M., Kruger, S.J., Frei, R. and Canfield, D.E. (2013) Atmospheric oxygenation three billion years ago. Nature 501, 535-538.

Delvigne, C., Opfergelt, S., Cardinal, D., Hofmann, A. and André, L. (2016) Desilication in Archean weathering processes traced by silicon isotopes and Ge/Si ratios. Chemical Geology 420, 139-147.

Diamond, C.W. and Lyons, T.W. (2018) Mid-Proterozoic redox evolution and the possibility of transient oxygenation events. Emerging Topics in Life Sciences 2, 235-245.

Droser, M.L. and Gehling, J.G. (2015) The advent of animals: The view from the Ediacaran. Proceedings of the National Academy of Sciences 112, 4865.

Duan, Y., Anbar, A.D., Arnold, G.L., Lyons, T.W., Gordon, G.W. and Kendall, B. (2010) Molybdenum isotope evidence for mild environmental oxygenation before the Great Oxidation Event. Geochimica et Cosmochimica Acta 74, 6655-6668.

Farquhar, J. and Wing, B.A. (2003) Multiple sulfur isotopes and the evolution of the atmosphere. Earth and Planetary Science Letters 213, 1-13.

Fehr, M.A., Hammond, S.J. and Parkinson, I.J. (2018) Tellurium stable isotope fractionation in chondritic meteorites and some terrestrial samples. Geochimica et Cosmochimica Acta 222, 17-33.

Gilleaudeau, G.J., Frei, R., Kaufman, A.J., Kah, L.C., Azmy, K., Bartley, J.K., Chernyavskiy, P. and Knoll, A.H. (2016) Oxygenation of the mid-Proterozoic atmosphere: clues from chromium isotopes in carbonates. Geochemical Perspectives Letters 2, 178-187.

Grandstaff, D.E., Edelman, M.J., Foster, R.W., Zbinden, E. and Kimberley, M.M. (1986) Chemistry and mineralogy of Precambrian paleosols at the base of the Dominion and Pongola Groups (Transvaal, South Africa). Precambrian Research 32, 97-131.

Gumsley, A.P., Chamberlain, K.R., Bleeker, W., Söderlund, U., de Kock, M.O., Larsson, E.R. and Bekker, A. (2017) Timing and tempo of the Great Oxidation Event. Proceedings of the National Academy of Sciences 114, 1811.

Hanski, E.J. and Melezhik, V.A. (2013) 3.2 Litho- and Chronostratigraphy of the Palaeoproterozoic Karelian Formations, Reading the Archive of Earth's Oxygenation: Volume 1: The Palaeoproterozoic of Fennoscandia as Context for the Fennoscandian Arctic Russia - Drilling Early Earth Project. Springer Berlin Heidelberg, Berlin, Heidelberg, pp. 39-110.

Hayes, S.M. and Ramos, N.A. (2019) Surficial geochemistry and bioaccessibility of tellurium in semiarid mine tailings. Environmental Chemistry 16, 251-265.

Hodgskiss, M.S.W., Crockford, P.W., Peng, Y., Wing, B.A. and Horner, T.J. (2019) A productivity collapse to end Earth's Great Oxidation. Proceedings of the National Academy of Sciences 116, 17207.

Holland, H.D. (2002) Volcanic gases, black smokers, and the great oxidation event. Geochimica et Cosmochimica Acta 66, 3811-3826.

Holland, H.D. (2006) The oxygenation of the atmosphere and oceans. Philosophical transactions of the Royal Society of London. Series B, Biological sciences 361, 903-915.

Holm, D., Schneider, D. and Coath, C.D. (1998) Age and deformation of Early Proterozoic quartzites in the southern Lake Superior region: Implications for extent of foreland deformation during final assembly of Laurentia. Geology 26, 907-910.

Hyslop, N. and White, W. (2009) Estimating Precision Using Duplicate Measurements. Journal of the Air & Waste Management Association (1995) 59, 1032-1039.

Jackson, J., Sweet, I.P. and Powell, T.G. (1988) Studies On Petroleum Geology And Geochemistry, Middle Proterozoic, mcarthur Basin Northern Australia I: Petroleum Potential. The appea Journal 28, 283-302.

Kashiwabara, T., Oishi, Y., Sakaguchi, A., Sugiyama, T., Usui, A. and Takahashi, Y. (2014) Chemical processes for the extreme enrichment of tellurium into marine ferromanganese oxides. Geochimica et Cosmochimica Acta 131, 150-163.

Kendall, B., Creaser, R.A., Gordon, G.W. and Anbar, A.D. (2009) Re–Os and Mo isotope systematics of black shales from the Middle Proterozoic Velkerri and Wollogorang Formations, McArthur Basin, northern Australia. Geochimica et Cosmochimica Acta 73, 2534-2558.

Ketchum, K.Y., Heaman, L.M., Bennett, G. and Hughes, D.J. (2013) Age, petrogenesis and tectonic setting of the Thessalon volcanic rocks, Huronian Supergroup, Canada. Precambrian Research 233, 144-172.

Kimberley, M.M. and Grandstaff, D.E. (1986) Profiles of elemental concentrations in Precambrian paleosols on basaltic and granitic parent materials. Precambrian Research 32, 133-154.

Kralik, M. (1982) Rb Sb age determinations on Precambrian carbonate rocks of the Carpentarian McArthur basin, Northern Territories, Australia. Precambrian Research 18, 157-170.

Lalonde, S.V. and Konhauser, K.O. (2015) Benthic perspective on Earth's oldest evidence for oxygenic photosynthesis. Proceedings of the National Academy of Sciences of the United States of America 112, 995-1000.

Large, R.R., Gregory, D.D., Steadman, J.A., Tomkins, A.G., Lounejeva, E., Danyushevsky, L.V., Halpin, J.A., Maslennikov, V., Sack, P.J., Mukherjee, I., Berry, R. and Hickman, A. (2015) Gold in the oceans through time. Earth and Planetary Science Letters 428, 139-150.

Lee, D.S. and Edmond, J.M. (1985) Tellurium species in seawater. Nature 313, 782-785.
Lyons, T.W., Reinhard, C.T. and Planavsky, N.J. (2014) The rise of oxygen in Earth’s early ocean and atmosphere. Nature 506, 307-315.

Marmo, J.S. (1992) The Lower Proterozoic Hokkalampi Paleosol in North Karelia, Eastern Finland, Early Organic Evolution: Implications for Mineral and Energy Resources. Springer Berlin Heidelberg, Berlin, Heidelberg, pp. 41-66.

Marty, B., Bekaert, D.V., Broadley, M.W. and Jaupart, C. (2019) Geochemical evidence for high volatile fluxes from the mantle at the end of the Archaean. Nature 575, 485-488.

Maynard, J.B., Sutton, S.J., Robb, L.J., Ferraz, M.F. and Meyer, F.M. (1995) A Paleosol Developed on Hydrothermally Altered Granite from the Hinterland of the Witwatersrand Basin: Characteristics of a Source of Basin Fill. The Journal of Geology 103, 357-377.

Maynard, J.B., Sutton, S.J., Rumble, D. and Bekker, A. (2013) Mass-independently fractionated sulfur in Archean paleosols: A large reservoir of negative Δ33S anomaly on the early Earth. Chemical Geology 362, 74-81.

McPhail, D.C. (1995) Thermodynamic properties of aqueous tellurium species between 25 and 350°. Geochimica et Cosmochimica Acta 59, 851-866.

Medaris, J.L.G., Singer, B.S., Dott, J.R.H., Naymark, A., Johnson, C.M. and Schott, R.C. (2003) Late Paleoproterozoic Climate, Tectonics, and Metamorphism in the Southern Lake Superior Region and Proto–North America: Evidence from Baraboo Interval Quartzites. The Journal of Geology 111, 243-257.

Mukasa, S.B., Wilson, A.H. and Young, K.R. (2013) Geochronological constraints on the magmatic and tectonic development of the Pongola Supergroup (Central Region), South Africa. Precambrian Research 224, 268-286.

Parnell, J., Spinks, S. and Brolly, C. (2018) Tellurium and selenium in Mesoproterozoic red beds. Precambrian Research 305, 145-150.

Payne, J.L., McClain, C.R., Boyer, A.G., Brown, J.H., Finnegan, S., Kowalewski, M., Krause, R.A., Lyons, S.K., McShea, D.W., Novack-Gottshall, P.M., Smith, F.A., Spaeth, P., Stempien, J.A. and Wang, S.C. (2011) The evolutionary consequences of oxygenic photosynthesis: a body size perspective. Photosynthesis Research 107, 37-57.

Peng, P., Liu, F., Zhai, M. and Guo, J. (2012) Age of the Miyun dyke swarm: Constraints on the maximum depositional age of the Changcheng System. Chinese Science Bulletin 57, 105-110.

Planavsky, N.J., Reinhard, C.T., Wang, X., Thomson, D., McGoldrick, P., Rainbird, R.H., Johnson, T., Fischer, W.W. and Lyons, T.W. (2014) Low Mid-Proterozoic atmospheric oxygen levels and the delayed rise of animals. Science 346, 635.

Qin, H.-B., Takeichi, Y., Nitani, H., Terada, Y. and Takahashi, Y. (2017) Tellurium Distribution and Speciation in Contaminated Soils from Abandoned Mine Tailings: Comparison with Selenium. Environ. Sci. Technol. 51, 6027-6035.

Rasmussen, B., Bekker, A. and Fletcher, I.R. (2013) Correlation of Paleoproterozoic glaciations based on U–Pb zircon ages for tuff beds in the Transvaal and Huronian Supergroups. Earth and Planetary Science Letters 382, 173-180.

Robardet, M., Bonjour, J.L., Paris, F., Morzadec, P. and Racheboeuf, P.R. (1994) Ordovician, Silurian, and Devonian of the Medio-North-Armorican Domain, Pre-Mesozoic Geology in France and Related Areas. Springer Berlin Heidelberg, Berlin, Heidelberg, pp. 142-151.

Robb, L.J. and Meyer, F.M. (1990) The nature of the Witwatersrand hinterland; conjectures on the source area problem. Economic Geology 85, 511-536.

Robb, L.J. and Meyer, F.M. (1995) The Witwatersrand Basin, South Africa: Geological framework and mineralization processes. Ore Geology Reviews 10, 67-94.

Rye, R. and Holland, H.D. (1998) Paleosols and the evolution of atmospheric oxygen: a critical review. American Journal of Science 298, 621 - 672.

Rye, R. and Holland, H.D. (2000) Life associated with a 2.76 Ga ephemeral pond?: evidence from Mount Roe #2 paleosol. Geology 28, 483-486.

Saad, E.M., Wang, X., Planavsky, N.J., Reinhard, C.T. and Tang, Y. (2017) Redox-independent chromium isotope fractionation induced by ligand-promoted dissolution. Nature Communications 8, 1590.

Schidlowski, M., Eichmann, R. and Junge, C.E. (1976) Carbon isotope geochemistry of the Precambrian Lomagundi carbonate province, Rhodesia. Geochimica et Cosmochimica Acta 40, 449-455.

Smithers, R.M. and Krouse, H.R. (1968) Tellurium isotope fractionation study. Can. J. Chem. 46, 583-591.

Smyth, A.L. (1984) Pedogenesis and diagenesis of the Olive Hill clay bed, Breathitt Formation (Carboniferous) northeastern Kentucky, Geology. University of Cincinnati.

Strand, K.O. and Laajoki, K. (1993) Palaeoproterozoic glaciomarine sedimentation in an extensional tectonic setting: the Honkala Formation, Finland. Precambrian Research 64, 253-271.

Sutton, S.J. and Maynard, J.B. (1992) Multiple alteration events in the history of a sub-Huronian regolith at Lauzon Bay, Ontario. Canadian Journal of Earth Sciences 29, 432-445.

Sutton, S.J. and Maynard, J.B. (1993) Sediment- and basalt-hosted regoliths in the Huronian supergroup: role of parent lithology in middle Precambrian weathering profiles. Canadian Journal of Earth Sciences 30, 60-76.

Sutton, S.J., Maynard, J.B. and Sutton, S. (1996) Basement Unconformity Control on Alteration, St. Francois Mountains, SE Missouri. The Journal of Geology 104, 55-70.

Toth, E.R.F., M.A.; Konig, S.; Schonbachler, M. (2019) Tellurium stable isotopes: constraining the composition of the BSE and the Late Veneer. Goldschmidt Abstracts.

Utsunomiya, S., Murakami, T., Nakada, M. and Kasama, T. (2003) Iron oxidation state of a 2.45-Byr-old paleosol developed on mafic volcanics. Geochimica et Cosmochimica Acta 67, 213-221.
Wang, Z. and Becker, H. (2013) Ratios of S, Se and Te in the silicate Earth require a volatile-rich late veneer. Nature 499, 328-331.

Wasserman, N.L. and Johnson, T.M. (2020) Measurements of mass-dependent Te isotopic variation by hydride generation MC-ICP-MS. Journal of Analytical Atomic Spectrometry.

Wasserman, N.L.J., Thomas M.; Mackinney, Joel; Kulp, Thomas (in prep) Antimony and tellurium isotopic fractionation during adsorption to goethite and illite.

Wilson, A.H. and Zeh, A. (2018) U-Pb and Hf isotopes of detrital zircons from the Pongola Supergroup: Constraints on deposition ages, provenance and Archean evolution of the Kaapvaal craton. Precambrian Research 305, 177-196.

Yierpan, A., König, S., Labidi, J., Kurzawa, T., Babechuk, M.G. and Schoenberg, R. (2018) Chemical Sample Processing for Combined Selenium Isotope and Selenium-Tellurium Elemental Investigation of the Earth's Igneous Reservoirs. Geochemistry, Geophysics, Geosystems 19, 516-533.

Zakharov, D.O., Bindeman, I.N., Slabunov, A.I., Ovtcharova, M., Coble, M.A., Serebryakov, N.S. and Schaltegger, U. (2017) Dating the Paleoproterozoic snowball Earth glaciations using contemporaneous subglacial hydrothermal systems. Geology 45, 667-670.

Zhang, S., Wang, X., Wang, H., Bjerrum, C.J., Hammarlund, E.U., Costa, M.M., Connelly, J.N., Zhang, B., Su, J. and Canfield, D.E. (2016) Sufficient oxygen for animal respiration 1,400 million years ago. Proceedings of the National Academy of Sciences 113, 1731.

Zhu, J.-M., Johnson, T.M., Clark, S.K., Zhu, X.-K. and Wang, X.-L. (2014) Selenium redox cycling during weathering of Se-rich shales: A selenium isotope study. Geochimica et Cosmochimica Acta 126, 228-249.